POLITECNICO
MILANO 1863

SCUOLA DI INGEGNERIA INDUSTRIALE
E DELL'INFORMAZIONE

Optimization study of cardiac resynchronization therapy by means of a calibrated electro-mechanics computational model

Tesi di Laurea Magistrale in
Biomedical Engineering - Ingegneria Biomedica

Author: **Silvia Fornara**

Student ID: 968970
Advisor: Prof. Christian Vergara[a]
Co-advisors: Francesco Regazzoni[b], Maurizio Del Greco[c]
Academic Year: 2021-22

[a]LaBS, Dipartimento di Chimica, Materiali, Ingegneria Chimica
[b]MOX, Dipartimento di Matematica
[c]Divisione di Cardiologia, Ospedale S. Maria del Carmine, Rovereto, TN, Italy

Ringraziamenti

Ringrazio il mio relatore Christian Vergara, che mi ha sempre aiutato con grande dedizione in questo percorso di tesi. Ringrazio inoltre i miei corelatori: Francesco Regazzoni, che mi ha guidato e supportato durante tutto il mio lavoro di ricerca, e il dr. Maurizio Del Greco, che mi ha dato la possibilità di lavorare con il suo gruppo a contatto con i clinici.

Ringrazio di cuore la mia famiglia che mi ha sempre incoraggiato e spronato: un caloroso grazie a mia mamma Nicoletta, mio papà Marco e mio fratello Giorgio. Ringrazio Ema, che mi ha sempre sostenuto e rincuorato. Ringrazio tutti i miei amici, con cui ho condiviso tanti momenti di gioia: ringrazio Sara G., Sara F., Jimmy, Michele, Lorenzo e Francesco. Ringrazio il mio maestro di pianoforte Jacopo, da cui ho imparato tanto.

Infine, un grazie speciale al mio cucciolotto Charlie, che in questi mesi è sempre riuscito a strapparmi un sorriso.

Abstract

Cardiac resynchronization therapy (CRT) is a treatment for heart failure, that aims at restoring the correct pumping action of the heart. CRT consists of the implantation of a pulse generator, that sends electrical stimuli to heart chambers by means of two electrodes, placed at the apex of the right ventricle and on the epicardium of the left ventricle, inside the epicardial coronary vein. CRT is indicated in patients with left bundle branch block (LBBB), a conduction disorder that leads to an impaired left ventricular activation and contraction. However, 30% of patients selected under the current guidelines do not respond to CRT, which could even worsen their clinical condition. In this context, this thesis aims at investigating how CRT outcomes could be improved, by means of a computational electro-mechanics (EM) model of the left ventricle.
In particular, we analyse four patients who underwent CRT in Ospedale S. Maria del Carmine in Rovereto (Italy). For each patient, we first model the pre-operative condition, calibrating the EM model with electrical and mechanical measures provided by Ospedale S. Maria del Carmine. To speed-up the mechanical calibration procedure, we introduce a novel approach that exploits a cardiac emulator, which is a surrogate 0D cardiac model, built on the basis of left ventricle pressure-volume transients obtained from EM simulations. The 0D emulator allows performing the mechanical calibration in a fast and efficient way, decreasing the computational cost needed.
The calibrated pre-operative model is then exploited to simulate acute post-CRT scenarios, hypothesizing that cardiac electrical and mechanical properties do not change just after the implant. To investigate how CRT outcomes could be improved, we test different configurations: in particular, we study the influence of different right and left electrode positions and how the setting of the time interval between the right and left stimuli can affect the efficacy therapy. All the configurations are compared with the pre-operative condition by means of suitable clinical indices.

Keywords: Cardiac resynchronization therapy, Heart failure, Cardiac electro-mechanics Model, Patient-specific model

Abstract in lingua italiana

La terapia di resincronizzazione cardiaca è un trattamento per lo scompenso cardiaco, volto a ripristinare la corretta azione di pompaggio del cuore. La tecnica consiste nell'impiantare un pacemaker che manda impulsi elettrici ai due ventricoli, attraverso due cavi con elettrodi posti nell'apice del ventricolo destro e sull'epicardio del ventricolo sinistro. La terapia è indicata in pazienti con blocco di branca sinistra, un'anomalia della conduzione elettrica cardiaca che porta a una contrazione ventricolare asincrona. Nella pratica clinica, il 30% dei pazienti selezionati per la terapia non mostra nessun miglioramento, andando anzi incontro in alcuni casi a un peggioramento delle condizioni cliniche. In questo contesto, l'obiettivo di questo lavoro è indagare come si possa migliorare la terapia, utilizzando un modello computazionale elettro-meccanico del ventricolo sinistro.
In particolare, in questa tesi si analizzano quattro pazienti trattati con terapia di resincronizzazione cardiaca all'Ospedale S. Maria del Carmine a Rovereto (Italia). Per ogni paziente, si modellizza lo scenario pre-operatorio, sfruttando le misure elettriche e meccaniche fornite dall'Ospedale S. Maria del Carmine per calibrare il modello elettro-meccanico. Per velocizzare la procedura di calibrazione meccanica, in questa tesi viene usato un emulatore cardiaco, ovvero un modello 0D del cuore costruito sulla base dei tracciati di volume e pressione del ventricolo sinistro, ottenuti da simulazioni elettro-meccaniche. L'emulatore 0D permette di svolgere la calibrazione meccanica in modo veloce e efficiente, diminuendo il costo computazionale della procedura.
Il modello pre-operatorio è poi sfruttato per simulare la terapia in acuto, ipotizzando che le proprietà elettriche e meccaniche del cuore non cambino subito dopo l'impianto. Per capire come si possa ottimizzare la terapia, in questa tesi sono analizzati diversi scenari: in particolare, si studia come le posizioni dell'elettrodo destro e sinistro e come la regolazione del tempo che intercorre tra lo stimolo al ventricolo destro e al sinistro possano influenzare la terapia. Tutte le configurazioni sono confrontate con lo scenario pre-operatorio attraverso appropriati indici clinici.

Parole chiave: Terapia di resincronizzazione cardiaca, Scompenso cardiaco, Modello elettro-meccanico del cuore, Modello paziente-specifico

Contents

1 | Introduction

1.1. Physiology of the heart

1.1.1. Basic anatomy of the heart

The heart is an organ whose primary function is pumping blood. It is located in the mediastinum, in the thorax [84]. It is divided in four chambers: two atria (right and left), in the upper part of the organ, and two ventricles (right and left), in the lower part (See Figure 1.1).

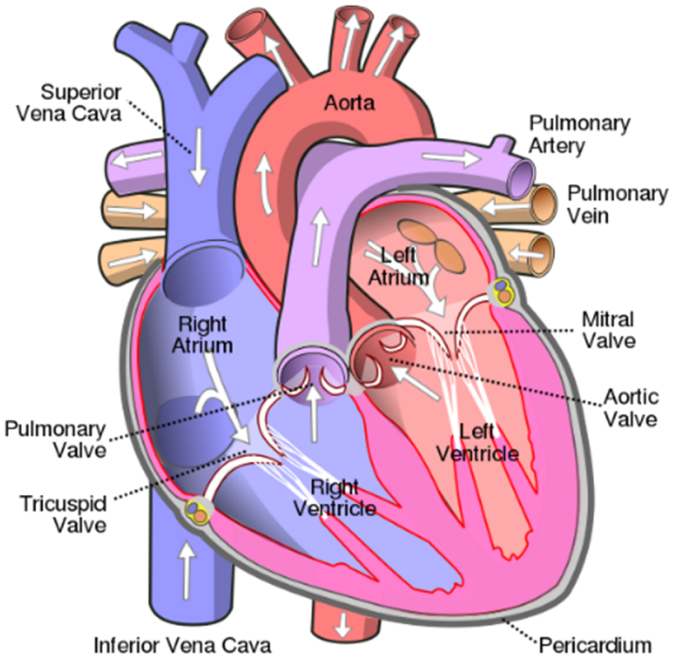

Figure 1.1: Anatomy of the heart. White arrows indicate the direction of the flow. Taken from [82].

The right atrium and the right ventricle (RV) constitute the right heart, that pumps venous blood, while the left atrium and the left ventricle (LV) compose the left heart,

that pumps arterial blood. The right heart and the left heart are separated by the interatrial septum and the interventricular septum, which divide the two atria and the two ventricles, respectively. To regulate the direction of the blood flow, in the heart there are two atrioventricular valves and two semilunar valves. Atrioventricular valves connect atria to ventricles, while semilunar valves connect ventricles to their respective artery. In particular, in the left heart we have:

- the mitral valve: it connects the left atrium to the LV;
- the aortic valve: it connects the LV to the aorta.

In the right heart we have:

- the tricuspid valve: it connects the right atrium to the RV;
- the pulmonary valve: it connects the RV to the pulmonary artery.

The venous blood reaches the right atrium from the superior and inferior vena cava (See Figure 1.1), passes through the tricuspid valve and reaches the RV. Then, it proceeds through the pulmonary valve and flows in the pulmonary artery, reaching the lungs (pulmonary circulation). Oxygenated blood comes back from the lungs and reaches the left atrium through the pulmonary veins. Then, it flows in the LV passing through the mitral valve and it is pushed in the aorta through the aortic valve (systemic circulation).

The wall of the heart is composed by three layers (from outside to inside): the epicardium, the myocardium and the endocardium. The myocardium is a particular muscular tissue and it is composed by contractile cells - also called cardiomyocytes - (90% of myocardium, they constitute the gross part of atria and ventricles) and conductile cells - also called pacemaker cells - (10% of myocardium) [67, 84]. Contractile cells generate force, while conductile cells make the electrical signal propagate through the heart.

1.1.2. Action potential of contractile cells

Cardiac cells can change their membrane potential (that at rest is -90 mV), if they receive a stimulus. When this happens, the action potential develops (See Figure 1.2).

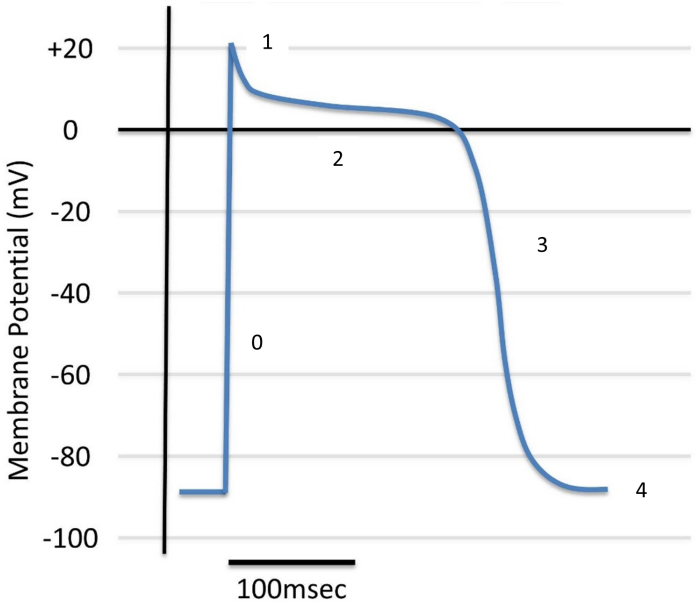

Figure 1.2: Cardiac cell action potential. Numbers indicate the phases of the action potential. Taken from [49]

The cardiac action potential is composed by five phases [84]:

- Phase 0: Sodium channels open rapidly; sodium enters the cell and increase the membrane potential (rapid depolarization phase);
- Phase 1: Sodium channels close, while potassium channels starts opening, making the potassium flowing out from the cell; the membrane potential decreases slightly;
- Phase 2: two events happen at the same time: calcium enters the cell as calcium channels open, while potassium leaves the cell, since particular potassium channels (different from the ones of phase 1) open. As a consequence, there is an inflow and an outflow of ionic positive currents, that eventually keep constant the membrane potential (at a value slightly greater than 0 mV). For this reason this phase is called the *plateau phase*;
- Phase 3: Calcium channels close, while potassium keeps flowing out, bringing the membrane potential back to the rest value;
- Phase 4: the membrane potential keeps the constant value of -90 mV, until a new stimulus reaches the cell. Meanwhile, the sodium-potassium pump and the sodium-calcium exchanger restore the original ion concentration in the cell.

The action potential of a contractile ventricle cell lasts approximately 250-300 ms [84].

Once the cardiac cell receives the stimulus, the action potential develops and the signal is propagated to other cells through the "gap junctions", a type of cell connection that permits the diffusion of the electrical signal. Therefore, the cell does not receive the contraction stimulus from neural activity, as in skeletal muscle, but from adjacent cells, through gap junctions. The stimulus originates from the pacemaker cells, that constitute the conduction system of the heart [67, 84].

1.1.3. The conduction system of the heart

Pacemaker cells differ substantially from cardiac contractile cells: during their action potential they do not reach the rest potential and, for this reason, they keep on depolarizing and repolarizing. Thus, pacemaker cells can generate an action potential without being stimulated [84]. Pacemaker cells are located in specific points, as Figure 1.3 shows.

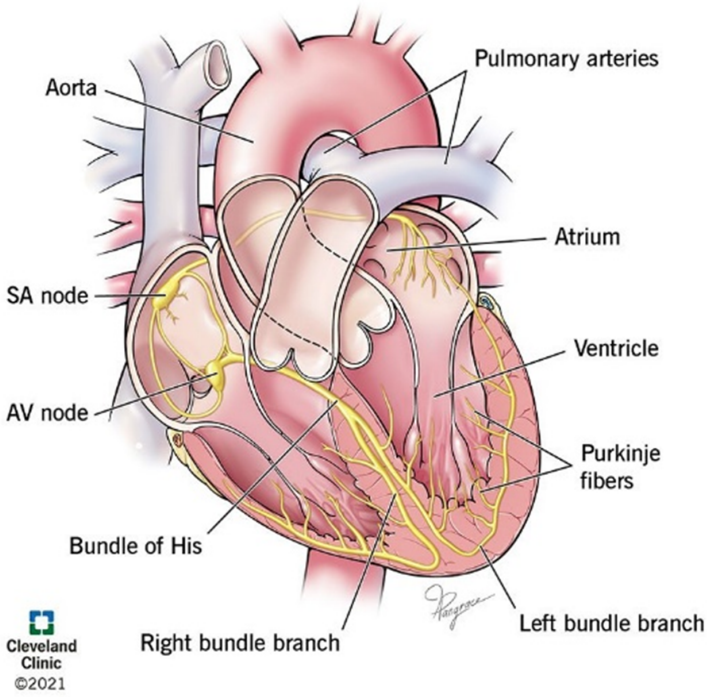

Figure 1.3: Heart conduction system. Taken from [15].

The pacemaker cells that initiate the stimulus are called the sinoatrial node (SA node): located in the right atrium, near the superior vena cava, they send the first impulse to start the beat. For this reason, they are also called the natural pacemaker of the heart [15, 42]. SA node is also responsible for the normal cardiac rhythm, that is called the sinus rhythm. The signal propagates to the atria (through the gap junctions) and reaches the boundary between the atria and ventricles. Here lies the atrioventricular node (AV node),

that permits the propagation of the stimulus to the ventricles. Actually, the two atria are electrically isolated from the ventricles, because of the presence of connective tissue in between. Thus, the AV node is the only point where the signal can be conducted [67, 84]. Another important function of the AV node is to delay the electrical signal, in order to permit the atria to finish their contraction [15, 84]. From the AV node, the electrical wave proceeds along the bundle of His, that covers the interventricular septum until it splits in two branches, the right bundle branch and the left bundle branch. The branches divide in the Purkinje fibers, that are interwoven in the ventricle walls. The Purkinje fibers have to very rapidly conduct the electrical impulse in order to permit the ventricles to contract synchronously. As a consequence of the path followed by the electrical wave, ventricles contract from the bottom to the top.

Each group of cells has its own action potential: as it can be seen in Figure 1.4 [42], each waveform is different from the other. Eventually, the different action potentials contribute to give shape to the electrocardiogram.

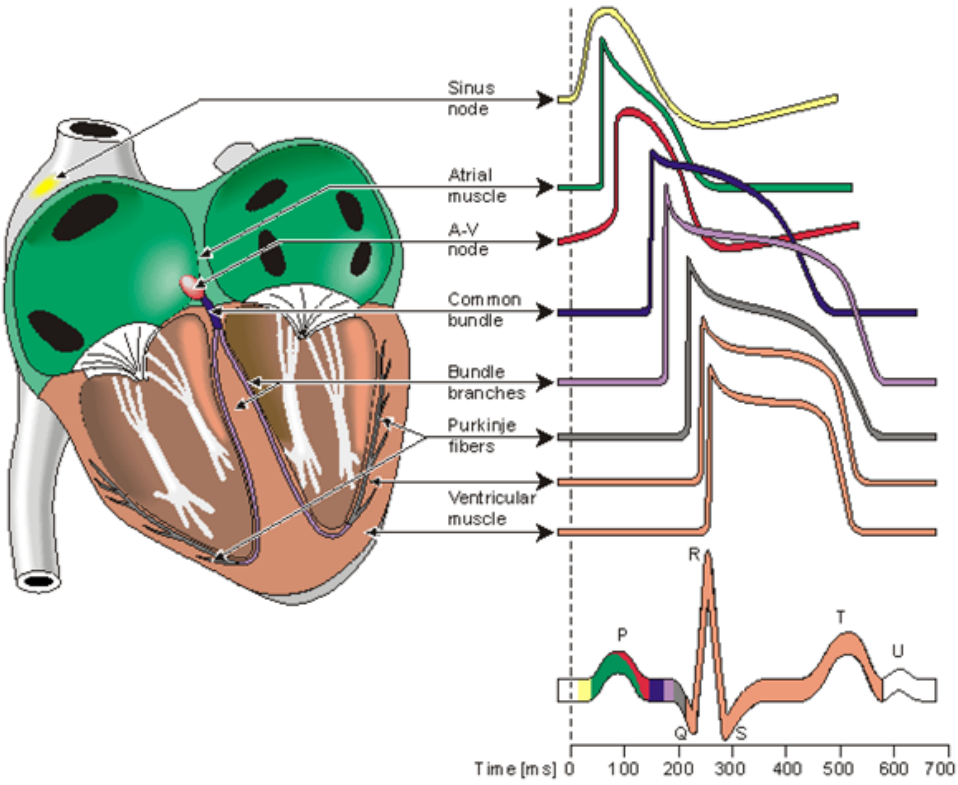

Figure 1.4: Heart electrophysiology. Taken from [42].

1.1.4. The heart contraction

The electrical activity of the heart (described in Section 1.1.2 and in Section 1.1.3) is coupled with the mechanical one, which is responsible of heart contraction. The cardiac cycle is composed by two alternating actions: contraction, called *systole*, and relaxation, called *diastole*. During the cardiac cycle, atria contract first and simultaneously, then, ventricles contract and push blood out. In particular, the cardiac cycle can be described by four phases (referring to the left heart) [65, 84]:

1. Isovolumetric contraction: the LV starts contracting; at this time ventricular pressure is greater than the atrial pressure but lower than the aortic pressure: therefore both the atrial and mitral valves are closed. The ventricle contracts keeping constant its volume and increasing its pressure;

2. Ejection: this phase starts when ventricular pressure value exceeds aortic pressure value, causing the opening of the aortic valve and, consequently, the blood flow through the artery. The volume of the ventricle decreases, while its pressure increases as long as active contraction keeps going on. When active contraction finishes, ventricular pressure decreases, inducing a negative blood flow through the aortic valve, which, as a result, closes;

3. Isovolumetric relaxation: in this phase, the ventricular pressure is lower than the aortic one but greater than the atrial pressure, therefore, as it happens in phase 2, both the aortic and the mitral valves are closed. The volume of the ventricle is constant as its pressure decreases;

4. Ventricular filling: ventricular pressure becomes lower than atrial pressure, causing the opening of the mitral valve. Blood starts flowing from the atrium to the ventricle, whose volume increases greatly. At the end of this phase, also atrium contraction contributes to ventricular filling.

The same phases hold true for the right heart, which, however, reaches significantly lower pressure values.

A common way to visualize the cardiac cycle is constituted by the Wiggers diagram (See Figure 1.5): it plots time on the X-axis, while on the Y-axis it shows the aortic, atrial and ventricular pressure, the ventricular volume, the electrocardiogram and the phonocardiogram (it shows heart sounds: every sound is associated to the opening and closing of a valve, apart from the third one, that is related to the rapid ventricular filling). Thanks to this diagram, it is very easy to associate the phases of the cardiac cycle.

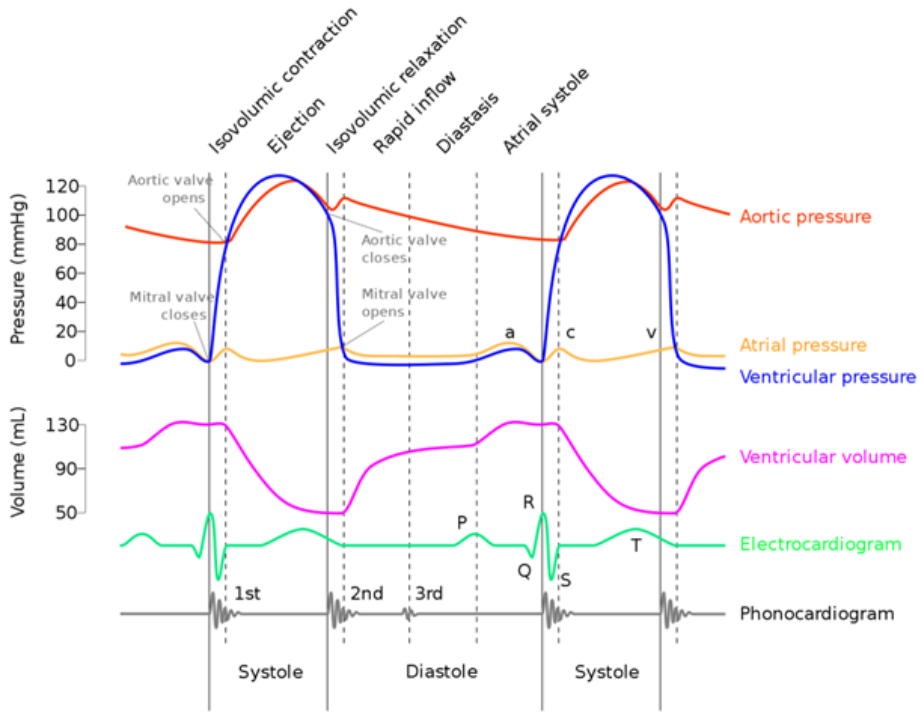

Figure 1.5: Wiggers diagram of the LV. Taken from [65]

Another way to visualize the cardiac cycle is the left ventricular pressure-volume (PV) loop: it plots the LV pressure on the Y-axis and the LV volume on the X-axis.

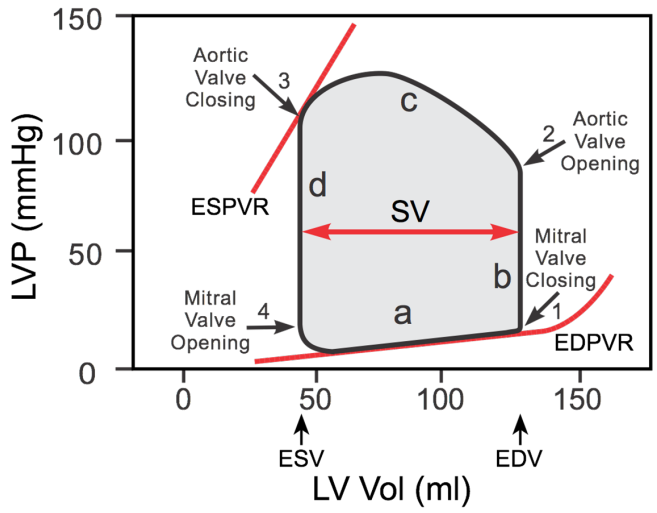

Figure 1.6: Heart PV loop. Adapted from [13]. a: ventricular filling, b: isovolumetric contraction, c: ejection, d: isovolumetric relaxation. ESV: End systolic volume, EDV: End diastolic volume. ESPVR: End-systolic pressure-volume relationship, EDPVR: End-diastolic pressure-volume relationship.

From the LV PV loop it is possible to point out some relevant clinical quantities [13, 65, 84]:

- ESV: End systolic volume, the volume of blood remaining in the ventricle after the contraction;
- EDV: End diastolic volume, the volume of blood in the LV before the contraction;
- SV: Stroke volume, given by $SV = EDV - ESV$;
- Ejection fraction (EF): given by $EF[\%] = \frac{SV}{EDV} \times 100$
- Aortic valve opening pressure;
- Aortic valve closing pressure;
- Mitral valve opening pressure;
- Mitral valve closing pressure;
- ESPVR: End-systolic pressure-volume relationship, the curve that represents the maximum pressure achievable by the ventricle at a given volume;
- EDPVR: End-diastolic pressure-volume relationship, the curve that represents the passive properties of the ventricle (the reciprocal of the slope of the curve is the ventricle compliance).

1.2. Heart Dyssynchronies

Cardiac dyssynchrony refers to an anomalous uncoordinated activation and contraction of the heart. It is divided in electrical dyssynchrony, that causes the prolongation of the conduction times in the ventricles (which reflects on the ECG as a longer QRS complex), and in mechanical dyssynchrony, that is related the asynchronous contraction of atria and/or ventricles [66]. Moreover, cardiac dyssynchronies are classified as [66]:

- atrioventricular dyssynchrony: atria and ventricles contract asynchronously because of a delay in the conduction stimulus at the AV node (see Section 1.1.3);
- interventricular dyssynchrony: the RV and LV do not contract synchronously because of the presence of a delay in the activation between the two chambers;
- intraventricular dyssynchrony: it is associated to delays in contraction and activation of the ventricle itself.

Interventricular and intraventricular dyssynchronies influence the heart pump function much more than atrioventricular dyssynchrony [66]. The ventricle dyssynchrony starts a

process of remodeling that is shown in Figure 1.7 [44].

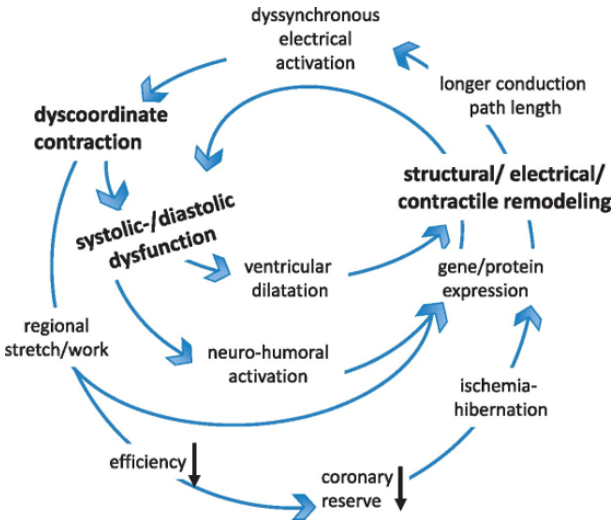

Figure 1.7: Cardiac dyssynchronies consequences. Taken from [44].

After the appearance of the dyssynchrony, the electrical conduction path changes, inducing a dyssynchronous electrical activation that leads to an uncoordinated contraction. As a consequence, the ventricle experiences systolic and diastolic dysfunctions, because of a non effective contraction. To supply the same amount of blood, the ventricle is forced to work at an higher volume to reach the same pressure as before the appearance of the dyssynchrony. Also, neuro-humoral signals intervene to stimulate the expression of a gene or protein, so that the ventricle can remodel itself. Moreover, the uncoordinated contraction dissipates more energy with respect to the healthy case, leading to a decrease of the efficiency of the contraction and of the coronary reserve, since the heart needs to be more perfused to do the same work [44]. The condition in which the heart cannot supply enough blood to the body is called "heart failure".

There are many pathologies and conditions that can lead to cardiac dyssynchrony: hypertrophic cardiomyopathy, ischemic heart disease, diastolic heart failure, hypertension, LV hypertrophy, left bundle branch block (LBBB), myocardial fibrosis [9, 44, 66]. For the purpose of this thesis, LBBB and myocardial fibrosis will be deeply discussed.

1.2.1. Myocardial fibrosis

Myocardial fibrosis refers to a condition in which there is over-deposition of extra cellular matrix (ECM), alterating the cardiac tissue structure and causing dysfunctions to the heart [25, 30].

There are three types of cardiac fibrosis [25]:

- Interstitial fibrosis;
- Perivascular fibrosis;
- Replacement fibrosis.

Interstitial fibrosis is related to a condition in which the perimysium and the endomysium (the internal and external membrane of muscular fibers) expand because of the ECM deposition; it is not connected to cardiomyocyte damages. Perivascular fibrosis regards the expansion of the external membrane of the microvasculature. Replacement fibrosis is the tissue response to cardiomyocyte damages or deaths: in fact, it typically happens after myocardium infarction. Dead cells are replaced by ECM (mostly formed by type I collagen), that forms a scar tissue. Interstitial and perivascular fibrosis mostly influence diastolic function, while replacement fibrosis influences systolic functions [25].

The presence of a scar both impacts the electrical and mechanical activation on the heart [30]. The scar is considered an electrical insulator: in fact, in a study from [1], areas with dense scar resulted to have a 1.97 to 2.66-fold slower conduction velocity with respect to non fibrotic tissue. Therefore, fibrosis can cause a conduction block, leading to heart dyssynchronies, that translates in a uncoordinated contraction and in a reduced cardiac efficiency (See Section 1.2). The scar could also cause the formation of a re-entry circuit (in the electrical conduction pathway), increasing the probability of the development of an arrhythmia. Cardiac fibrosis is therefore a factor that has to be taken in great consideration in order to find an effective treatment for cardiac dyssynchronies.

1.2.2. Left bundle branch block

Left bundle branch block (LBBB) is a conduction disorder that leads to an altered left ventricular activation and contraction. As it can be seen in Figure 1.8, the conduction signal does not follow the usual path along the left bundle branch, because of the presence of a block. Therefore, the RV activates earlier with respect to the LV, whose activation happens at the level of the mid-septum, and then proceeds homogeneously to the rest of the ventricle [16, 52, 74, 75].

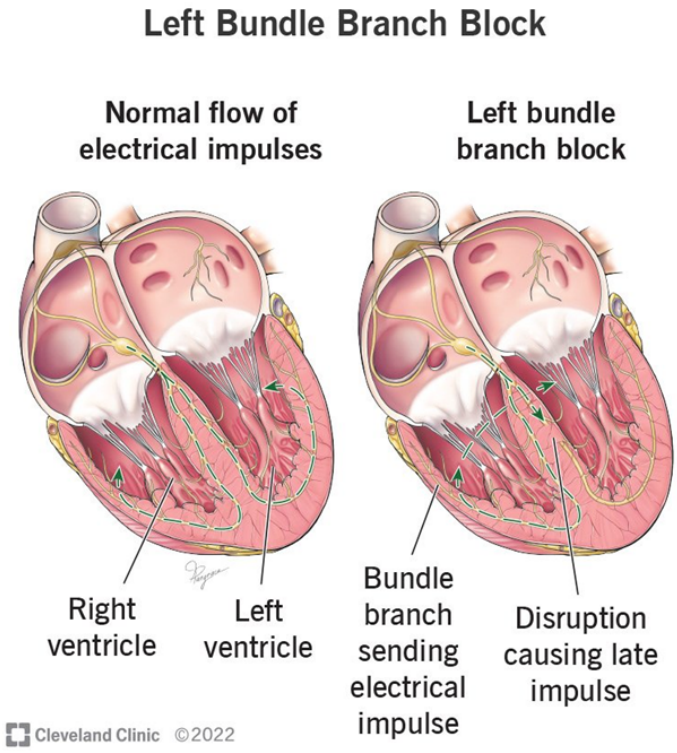

Figure 1.8: Physiological conduction system and LBBB. Taken from [16].

The abnormal conduction signal translates in an uncoordinated contraction [75]: in the early systole, the RV and the interventricular septum contract first, causing the passive stretch of the posterior and lateral walls of the LV. Then, also the walls contract, stretching the septum. As a consequence, the contraction results uncoordinated and less efficient.

LBBB is not typically diagnosed in young people: it is actually identified at an average age of 70 ± 10 in men and 68 ± 11 in women [52, 74]. Regarding the etiology of this disorder, it is still not clear what is the real cause of LBBB. However, different studies have found association of LBBB to different conditions like arterial hypertension, coronary artery disease, valvular-related disease [52, 74, 75]. LBBB can also be diagnosed after the implantation of a transcatheter aortic valve, probably because of the interference of the implant on the conduction pathway [74].

LBBB could be identified through the ECG: in particular, the prolongation of the QRS complex ($\geq$ 120 ms) is widely recognized as an indicator of the presence of LBBB [52, 74, 75]. However, the validity of this criterion is still discussed: in fact, in 2009 the criterion was changed, focusing also on the QRS complex morphology, besides the QRS prolongations [74].

LBBB is commonly treated with cardiac resynchronization therapy (CRT), a pacemaker that will be deeply discussed in Section 1.3. Besides this treatment, there are other therapies currently under study, that aim at restoring the conduction pathway (for example with the use of stem cells or conductive polymers). However, these treatments are still in the pre-clinical phase, being not considered safe for their use on humans [74].

1.3. Cardiac resynchronization therapy

1.3.1. Components and implantation

Cardiac resynchronization therapy (CRT) refers to the implantation of a cardiac pacemaker that has to restore the correct pumping action of the heart in patients with heart failure (see Section 1.2). In CRT, electrical stimuli are sent to both ventricles in order to make them contract simultaneously. For this reason, this therapy is also called biventricular pacing.

The CRT systems are composed by three elements [7, 46, 64] (See Figure 1.9):

- Pulse generator: a device usually implanted beneath the skin under the collarbone. It has to continuously monitor the heart and deliver electrical stimuli to coordinate the heart contraction. Optionally, it can also include a defibrillator: this is called cardiac resynchronization therapy defibrillator (CRT-D), otherwise cardiac resynchronization therapy pacemaker (CRT-P);
- right ventricular lead: it is placed through a catheter in the RV, near the apex;
- left ventricular lead: through a catheter, it is placed through the coronary vein on the epicardium of the LV.

Optionally, there can also be a lead in the right atrium.

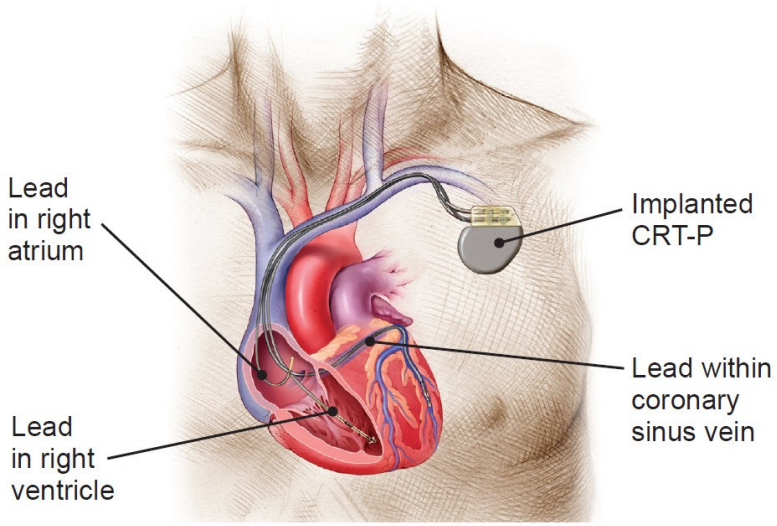

Figure 1.9: Illustration of CRT components. Taken from [6].

To implant the CRT system, a patient needs to be sedated. A small incision is done near the collarbone, so that leads can be inserted through a vein (usually the subclavian, auxillary or cephalic vein [29]): the leads run through it to reach the right atrium and the apex of the RV, so that they can directly touch the inner wall of the two chambers. The third lead is inserted in the coronary vein of the LV. Depending on the patient, to insert the left ventricular lead, it may be necessary to create another incision on the side of the chest. If leads are correctly positioned (their location is monitored by means of fluoroscopy [29]), they are tested in order to verify that they can send proper stimuli to the heart. Then, leads are connected to the pulse generator, that is implanted near the collarbone [7].

1.3.2. Long term effects

As soon as CRT starts working, the heart dyssynchrony is reduced. The therapy induces a mechanism of reverse remodeling that is summarized in Figure 1.10.

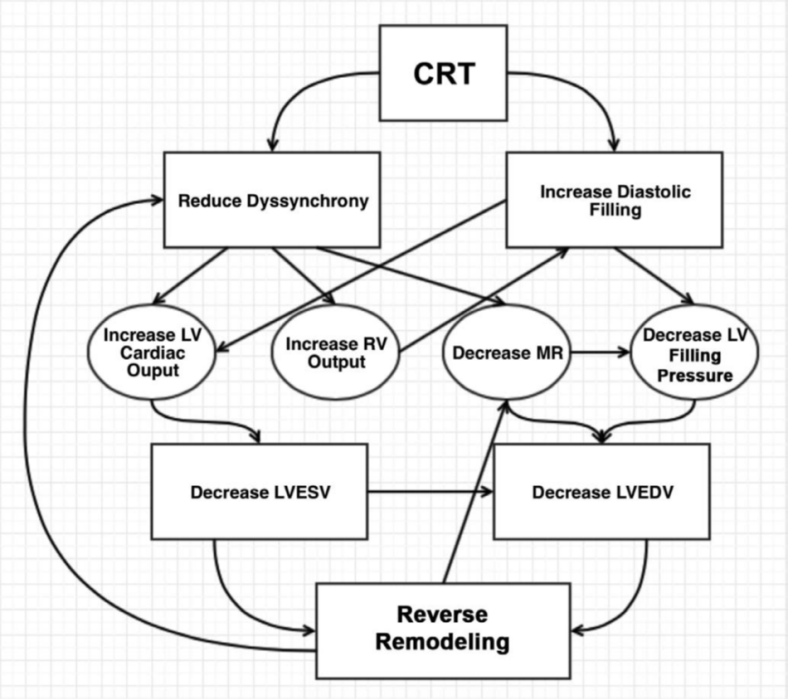

Figure 1.10: CRT-induced reverse remodeling. Taken from [34]. LV: left ventricle, RV: right ventricle, MR: mitral regurgitation, LVESV: left ventricle end systolic volume, LVEDV: left ventricle end diastolic volume.

In particular, we can distinguish between short-term effects (e.g. just after CRT implant) and long term effects (e.g. some months after the implant) [34]:

- Short term effect: cardiac output increases, since mechanical contraction becomes more synchronized;
- Long term effects: in some months, the therapy induces long-term changes to the heart structure, in a process called reverse remodeling. Specifically, we have:
  - A decrease in the LV size as well as in ESV and EDV, because of the improvement in systolic and diastolic functions;
  - A decrease in diastolic filling time, which leads to a reduction in the LV filling pressure;
  - A decrease in mitral regurgitation.

In this thesis, we will model only short term effects of the therapy, thus excluding the reverse remodeling process.

To assess long term changes induced by CRT, typically clinical measures and classifications used are the following [20, 33]:

- six-minute walk test: the patient is asked to walk for six minutes, the distance covered is compared with respect to the value obtained before CRT implant;
- EF: difference in EF with respect to pre operative value;
- the increase in the maximum rate of ventricular pressure (dP/dt_{max}): it is used as a measure of myocardium contractility;
- New York Heart Association (NYHA) classes: NYHA categorizes heart failure in classes, from mild symptoms - class I - to severe symptoms - class IV. After CRT implant, the NYHA class of the patient can change.

1.3.3. Patient selection and non-responders

According to the American Heart Association (AHA) (last update: 2012)[23], CRT is highly indicated for patients with a left ventricular EF $\leq$ 35%, sinus rhythm, LBBB morphology, QRS $\geq$ 150 ms and NYHA class III or IV. European Society of Cardiology (ESC) (last update: 2021) recommends CRT with the same criterion, but it does not use NYHA classes [26]. Though the ESC and AHA criteria are widely accepted, in 30% of the patients belonging to this category there is no clinical benefit from CRT [34]. In some cases there has been even a worsening in the patient conditions [35]. In fact, patient selection is a matter still under great discussion: at the moment, it is not clear whether or not considering patients with 120 ms $\leq$QRS$\leq$ 149 ms and without LBBB morphology [23, 26]. In order to reduce the rate of non-responders, some studies have tried to find new indices to correctly select patients [46]: in particular, they used ecocardiography to assess mechanical dyssynchrony. However, no measure was found to predict CRT response. Further investigations are needed to correctly select eligible patients for CRT. Nonetheless, apart from patient selection criteria, there are other factors that may lead to an ineffective therapy, such as the left and right ventricular lead positions, the ventriculoventriucular (VV) delay and inconsistent pacing [34, 35].

1.3.4. Left and right lead position

An optimal positioning of the left ventricular lead is crucial to determine the success of the implant. Theoretically, the lead should be placed in the last electro-mechanical activated point, that is usually in the lateral or postero-lateral side of the LV [34, 35], as long as this point could be reached through the epicardial coronary vein (See Figure 1.11). Locations that should be excluded are the apical zone [34, 35], since it can increase the probability of heart failure, and scarred region. In fact, pacing at fibrotic regions should be avoided

because the electrical stimulus would not be entirely conducted [34]. Regarding the right lead positioning, it is usually placed in the apex of the right ventricle: however, other locations (e.g. right ventricle septum and His bundle) should be investigated, being these positions accessible during the CRT implant [83].

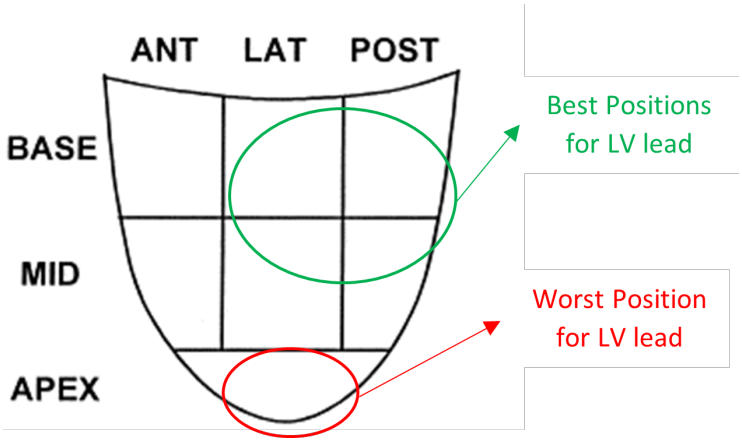

Figure 1.11: Different left ventricular lead positions in CRT. Modified from [2]. ANT: anterior, LAT: lateral, POST: posterior.

Another aspect that is raising interest in the last years regards endocardial pacing [46]: the left lead is placed inside the LV, directly touching the endocardium. With this procedure, the heart is electrically activated faster and in a more physiologic way with respect to standard epicardial pacing, leading to an increased contractile function. The main problem with this technique is related to the potential formation of clots, that could cause stroke and systemic embolism.

1.3.5. Ventriculoventricular delay

Ventriculoventricular (VV) delay can be defined as the time interval between the stimulus sent by the left ventricular lead and the one sent by the right ventricular lead. Optimization of VV delay is a critical aspect, that is still under discussion, since it is a very important parameter that can greatly affect the interventricular and intraventricular dyssynchronies (See Section 1.2). However, VV delay optimization is never done, since it is time consuming during a CRT implantation. Guidelines suggests to fix to zero the VV interval [35, 46]. Further investigations should be performed in order to understand the best way to set VV and its relation with non-responders. Ideally, the CRT system should automatically set the correct parameter: at the moment, some companies have developed algorithm able to optimally set VV delay [46]. Indeed, in [62] it was tested an algorithm able to automatically optimize the VV delay: however, it leaded to a widening

of the QRS complex, and therefore it was rejected. Nonetheless, automatic optimization of the VV delay is a promising field, that is currently under study.

1.3.6. Inconsistent pacing

Inconsistent pacing may be the cause of CRT failure: it refers to a condition in which the heart own frequency is higher than the maximum one set on the device, so that CRT system cannot pace the heart [34]. This happens in patients suffering from tachycardia, a type of arrhythmia in which the heart frequency is greatly increased. In order not to lose CRT benefit, the patient should undergo a pharmacologic therapy, so that heart rhythm could be controlled [34].

1.4. Cardiac electro-mechanics modeling

1.4.1. Overview of cardiac mathematical models

To realistically develop a heart model, it is necessary to include and integrate different multi-scale and multi-physic models [8, 59, 78]. The heart functioning is indeed a result of the coupling of the electrophysiology activity (from the ionic currents causing the generation of the action potential to the transmission of the electrical impulse), active and passive mechanics (from the protein to the the entire organ contraction and relaxation) and blood flow mechanic. The coupling between the electrical and mechanical part is achieved by means of calcium dynamics: during the electrical activation calcium is released and induces the muscle contraction [8, 78]. The electro-mechanical coupling is also called excitation-contraction coupling [8]. Lastly, an important feature that should be present to develop a realistic heart model is the integration of clinical measures: electrical measures (such as electrocardiography (ECG) and electrical mapping), mechanical measures (e.g. ejection fraction (EF)) should be used to calibrate the computational model in order to create a patient-specific model and to assess its validity.

To summarize, to develop an electro-mechanic mathematical model of the heart it is necessary to include the following models (see Figure 1.12) [8, 78]:

- Electrophysiology models:
  - Cellular ionic model;
  - Tissue propagation model;
- Mechanical models:

  - Active tension generation model;
  - Passive elastodynamic cardiac model;
- Hemodynamic model.

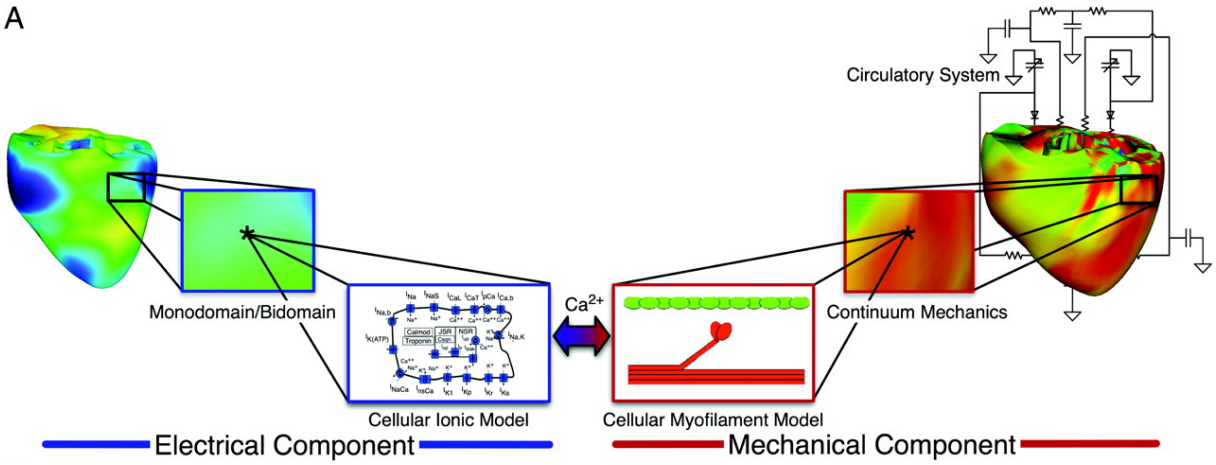

Figure 1.12: Heart modeling. Adapted from [78].

Cellular ionic models describe the development of the action potential by modelling the ionic channels, pumps and exchangers present in the cell [8, 78]. These models are composed by a system of ordinary differential equations. Current models simulate ventricular myocytes, like in *O'Hara et al.* [48], *Ten Tusscher et al.* and *Tomek et al.* [77], atrial myocytes (*Courtemanche et al.* [19]) and even the Purkinje fibers (*Stewart et al.* [71]). Cellular ionic models are coupled with tissue propagation models, that describe the propagation of the electrical stimulus through the organ. For this purpose, the bidomain and monodomain models are commonly used [8, 69]. The bidomain model consists of a set of two of partial differential equations that compute the propagation of the cellular transmembrane and external potential. The bidomain model is very complex and difficult to solve, thus, the monodomain model was introduced. The monodomain model simplifies the bidomain model by assuming that the external and internal conductivity tensors of the cardiac tissue are proportional. This model can compute the trans-membrane potential, and, with a post-processing calculation, the external membrane [69]. A further simplification is constituted by the Eikonal model, that allows to compute only activation times; it has a reduced computational cost with respect to the bidomain and monodomain models [70]. Also, to reduce computational times, it is possible to use cellular automation models [38, 60]. In these models, action potentials are pre-calculated and then applied according to rules that include electrophysiology principles [80]. As a result, temporal and spatial distribution of transmembrane potential is fastly computed.

Active tension generation can be described by mainly two types of approach [57]:

- Phenomenological models: they use simple laws to fit measured data; a flaw of these kind of models is related to the fact that the parameters used often do not have a physical meaning;
- Biophysically detailed models: these models precisely describe the behaviour of the proteins involved in the generation of active force. However, these models are very computationally demanding: the computational time is huge.

Regarding the passive properties of the heart, the organ is usually described through equations of continuum mechanics and it is modeled as an orthotropic, hyper-elastic and near-incompressible material [78]. Famous models are the Guccione model, a strain based model (meaning that the strain energy function depends directly on the deformation), and the Holzapfel-Gasser-Ogden model, which is an invariant based model (the strain energy function depends on the invariants of the right Cauchy-Green tensor $\mathbf{C}$).

Lastly, it is essential to couple the electro-mechanic model of the heart to blood circulation. This could be achieved with multi-scale and multi-physics code that can account to fluid-structure interactions: however, this is a very complex approach. More often, the coupling with blood circulation is obtained through the use of a simple lumped parameter model, that can simulate the whole body circulation [8]. An example of lumped parameter model is the Windkessel model.

The models previously described are essential to develop a complete electro-mechanic model of the heart. They can be applied on an idealized geometry or on patient-specific geometry, which can be obtained by medical imaging techniques, such as magnetic resonance imaging (MRI). Another important aspect that has to be present is the cardiac fiber orientation, which defines the preferential direction of electrical propagation [8, 78]. This could be achieved by integrating information either from histological sections or from diffusion-tensor MRI [78]. However, this kind of information is hardly available, therefore mathematical models are needed to define fibers orientations. An example is the rule-based algorithm developed by *Bayer et al.* [4].

Cardiac electrical and mechanics models previously described have to be mathematically coupled, since they deeply interact with each other [53]. In particular, the tissue propagation model computes either the transmembrane potential or the calcium concentration, that are needed by the active tension model to calculate the active tension. Moreover, the mechanics model influences electrophysiology, since the action potential propagation problem has to be solved on a moving domain, because of the cardiac contraction and relaxation

cycle [54]. These interactions give rise to a highly coupled electro-mechanical problem, composed by four blocks: the ionic model, the tissue propagation model, the active tension model and the mechanics model. Addressing the case in which the monodomain model is implemented, a possible strategy to numerically solve the electro-mechanic problem consists in solving first the electrical problem (e.g. monodomain problem and cell ionic model) at each time step, and then the mechanics problem [28, 43, 73]. The electrical problem can be solved with either an implicit, semi-implicit or explicit method. The electro-mechanic model could be solved also by splitting the electrical model (with a semi-implicit method): in particular, the ionic model is solved first, followed by the mechanics problem and lastly by the monodomain problem [50]. Some recent works [70, 72] have considered to use the reaction-Eikonal model, that is composed by the standard Eikonal problem and a monodomain-like reaction problem. The reaction-Eikonal problem is solved first, followed by the mechanics problem. This strategy allows to greatly reduce the computational cost, since the reaction-Eikonal model is solved offline.

Cardiac electro-mechanic models can be used to study pathologies and therapies, such as atrial and ventricular arrhythmia, defibrillation and also CRT, that will be deeply discussed in the next section.

1.4.2. Computational modeling of cardiac resynchronization therapy

As previously described in Section 1.4.1, electro-mechanic models of the heart can be applied to simulate CRT. Current computational studies used to model CRT are summarized in Table 1.1. In this context, also RV and LV pacing were taken in consideration, since this kind of models can potentially be applied also to CRT.

Firstly, it can be noticed that more than half of the studies uses only an electrical model [17, 18, 32, 39, 40, 60]: the mechanical part is therefore ignored. In these works, the focus is on the activation times computed in different configurations, in order to find the best way to optimize CRT (e.g. varying lead locations [60], pacing near/far from the scar [17, 18, 39], varying ventriculoventricular (VV) delay [60], comparing epicardial and endocardial pacing [18, 32]). Activation times (and its post-processing related calculations) become the only parameter that can be used to discriminate between different scenarios, posing a limit on this kind of studies. In fact, given the strict correlation between electrical conduction and heart contraction, a mechanical model of the heart is required to correctly assess and study CRT effects [38]. This was done in *Niederer et al.* [45], *Crozier et al.* [20], *Lee et al.* [37] and in *Isotani et al.* [33]. In these studies, besides activation times, also SV, EF

and dP/dt_{max} are evaluated, offering a more complete view of the CRT effects. Moreover, these studies include a fluid dynamic model: in most of the cases it is a simple three element Windkessel model [20, 37, 45]. In *Isotani et al.* [33], it was used a more complex and accurate lumped parameter model of the systemic and pulmonary circulation: it describes more precisely the circulation with respect to the Windkessel model, but it also requires more parameters to be suitably chosen.

Another important aspect regarding CRT simulations is constituted by the integration of clinical measures in the model. To correctly model electrophysiology, it is necessary to calibrate the electrical model to realistically reproduce the propagation of the electrical stimulus. This can be done by means of electrical mapping [20, 45], through which it is possible to know the activation times in the heart, by fitting the model parameters according to QRS duration [37, 39] or by reproducing the ECG recorded [33]. This last option requires a model of the torso, thus increasing the computational cost. Electrical mapping could lead to a precise calibration, while considering the QRS duration is less accurate. On the other hand, data from electrical mapping are not often available, while QRS duration, obtained from the ECG, is always accessible. In works without an electrical calibration [17, 18, 32, 40, 60], the choice of model parameters is based on previous literature studies. Besides electrical calibration, also mechanical calibration should be performed. In all studies listed in Table 1.1, mechanical calibration is performed by fitting the specific patient PV loops to the model [20, 33, 37, 45].

Another feature that should be present to realistically model CRT is the reconstruction of the coronary epicardial veins. Actually, none of the studies in Table 1.1 models epicardial vein geometry: however, modeling vein geometry would be very useful to understand where the left ventricular lead could be realistically placed. Indeed, not all the locations on the LV are easily accessible during a CRT implant. Besides from epicardial vein geometry, also scarred regions should be present in the model: this is done in many works [17, 18, 31, 33, 37, 39, 40, 45], and it is essential to study the effect of fibrosis on CRT.

An alternative to three-dimensional models of the heart is constituted by the CircAdapt model [31]. CircAdapt model is composed by a set of modules, each representing an element of the cardiovascular system (e.g. atria, ventricles, valves, arteries). As demonstrated by *Huntjens et al.* [31], with the CircAdapt model it is possible to simulate CRT with the presence of fibrosis. Ventricles are modeled as chambers with three walls: RV free wall, LV free wall and the interventricular septum. Then, each wall is subdivided in patches, each assigned with an activation time (that can be obtained by patient measures) [38]. The CircAdapt model allows to simulate CRT in real time, giving information about the anatomical, mechanical and hemodynamic response. It can easily describe macro-

scopic adaptation of the heart, without however offering a detailed view of microscopic dynamics [38].

	Article	Virtual CRT	Models	PSG	Calibration with EAM	Calibration with PV	Fibrosis	Fluid dynamic model
Electrophysiology model only	Reumann et al. (2007) [60]	✓	Electrical model: CAM	No	No	No	No	No
	Hyde et al. (2015) [32]	✓	Electrical model: Monodomain model	Yes*	No	No	No	No
	Lee et al. (2019) [39]	✗ (RV pacing)	Electrical model: Reaction-Eikonal	Yes	No†	No	Yes	No
	Costa et al. (2019) [17]	✓	Electrical model: Reaction-Eikonal Monodomain	Yes	No	No	Yes	No
	Lee et al. (2019) [40]	✗ (RV pacing)	Electrical model: Eikonal	Yes	No	No	Yes	No
	Costa et al. (2020) [18]	✓	Electrical model: Reaction-Eikonal	Yes	No	No	Yes	No
Electro-mechanics model	Niederer et al. (2011) [45]	✗ (LV pacing)	Electrical model: Monodomain model Active force model: Kerckhoffs et al.	Yes	Yes	Yes	Yes	Windkessel model
	Crozier et al. (2016) [20]	✓	Electrical model: Monodomain model Active force model: Kerckhoffs et al.	Yes	Yes	Yes	No	Windkessel model
	Lee et al. (2017) [37]	✓	Electrical model: Monodomain model Active force model: Kerckhoffs et al.	Yes	No†	Yes	Yes	Windkessel model
	Isotani et al. (2020) [33]	✓	Electrical model: Bidomain model	Yes	No†	Yes	Yes	Lumped model of systemic and pulmonary circulation
0D model	Huntjens et al. (2014) [31]	✓	CircAdapt model	No	No	No	Yes	CircAdapt model

Table 1.1: State of the art of CRT modeling studies. PSG: patient-specific geometry, EAM: electro-anatomical mapping, PV: pressures and volumes, CAM: cellular automation model, RV: right ventricle, LV: left ventricle. * The geometry refers to a canine ventricle. † Electrical calibration was performed by fitting ECG data.

1.5. Aim of the thesis

Cardiac resynchronization therapy (CRT) is an effective treatment for heart failure, however 30% of the patients, selected according to current implant criteria, do not respond

to this therapy, that, in some cases, can even worsen their clinical situation. It is still not clear the reason why CRT fails: it may be related to lead positions (with the left ventricular lead often placed in the latest electrically activated segment (LEAS), while the right one is commonly placed at the right ventricle apex), to the setting of ventriculoventricular (VV) delay, whose optimization is rarely performed during CRT implant.

In this context, this thesis aims at investigating how different CRT configurations can improve the therapy outcomes, using a computational patient-specific electro-mechanics (EM) model that includes real patient geometry of the left ventricle (LV) together with the reconstruction of the coronary epicardial veins and electrical and mechanical measurements for its calibration. The model will be deeply discussed in the next chapters.

In particular, this work is composed by two main sections, each one correlated by a specific aim:

1. Patient-specific calibration: firstly, we want to personalize the EM model for every patient studied, integrating clinical data provided by Ospedale S. Maria del Carmine. In particular, two patients with fibrosis and two without fibrosis are studied; for each patient both an electrical calibration, based on measures obtained from electrical mapping, and a mechanical calibration, based on pressure-volume (PV) loop measures, are performed. All these data refer to the preoperative condition, that is the one firstly modeled;
2. Simulations of virtual CRT scenarios: the second purpose of this work is investigating how different CRT scenarios can impact the therapy outcomes, comparing every configuration studied on the basis of some clinical indices. We consider the following scenarios:
    a. Study of left electrode location: we want to investigate how different left electrode locations affect CRT, in order to find out which configuration best improves the therapy. Starting from the preoperative scenario, virtual CRT is performed, keeping the right electrode position fixed and varying the left one along the coronary epicardial veins. We also want to pay attention to LEAS effects, that are studied and compared with other points of stimulation;
    b. Study of VV delays: different VV delays are simulated, in order to identify the configuration that most improves CRT outcomes;
    c. Study of right electrode positioning: keeping the left electrode fixed at the LEAS, different right electrode positions are simulated. In this way, we want to understand how the right electrode positions can influence CRT. Indeed, the standard

right electrode position (e.g. the right ventricle apex) is not the only accessible location during the mapping procedure: the right lead could be also placed at the right ventricle septum [83], that is the area we consider in this work.

To reach these goals, we simulate CRT on the LV with a cardiac electro-mechanic (EM) model, proposed by [11, 68, 70], with the following features:

- Geometry: CRT is simulated on the reconstructed LV geometry obtained from magnetic resonance imaging (MRI), with and without scarred regions. Moreover, patient-specific epicardial vein geometry is considered, allowing to realistically select the LV electrode positions, as done in [11, 68]. LV and epicardial vein reconstruction was performed in the work of [68];
- EM model, composed by:
  - The Tor-ORd ionic model [77], an electrophysiological detailed model of the ventricular cardiomyocyte (See Section 1.4.1). Thanks to its high degree of accuracy, this model allows us to retrieve intracellular calcium concentration at different heart rates: in this way, we can include in our model patient-specific heart rates, differently from the work of [11, 68], where cardiac frequency was fixed for every patient treated. Indeed, in [11, 68] it was used the 18-variables ten Tusscher-Panfilov ionic model [76], which is not able to reproduce calcium dynamics at high and low heart rates;
  - The reaction-Eikonal problem, that models cardiac electrophysiology. The idea (proposed in [70]) is to solve the Eikonal model to retrieve activation times, that are needed by the reaction problem to compute the applied ionic current, in order to calculate the intracellular calcium concentration. The reaction-Eikonal model introduces a great innovation with respect to standard monodomain or bidomain models: the reaction-Eikonal problem is solved offline, thus greatly reducing the computational cost, making it a very efficient model;
  - The active and passive mechanics model [47], represented by the momentum conservation equation. It is linked to the electrical model by means of the excitation-contraction coupling;
  - The RDQ20-MF model [57], that is the active force generation model. It is a biophysically detailed model, that allows to precisely describe the behaviour of proteins involved in the cardiac contraction and relaxation cycle, computing the generated active tension. It is coupled with the mechanics model by means of a relation between the active tension and the cardiac displacement, obtained

through the mechanics model;

– A 0D circulation model, represented by a standard two-element Windkessel model [81]. It is coupled with the mechanics model by means of a constraint on the LV pressure and volume;

- Electrical and mechanical calibration: in this work, we use data from electro-anatomic mapping to calibrate the Eikonal model, i.e. to select proper cardiac tissue conductivity values to match clinical measures, as done in [11, 68]. Considering data from electro-anatomic mapping instead of electrocardiography (ECG) allows to develop a more accurate patient-specific model, since electrical measures are recorded inside the ventricle, and not on body surface. Also, we mechanically calibrate our model in order to reproduce the PV tracings clinically measured, as done in [11]. Compared to [11], we introduce a simplification and a significant speed-up in the mechanical calibration procedure, by exploiting the 0D cardiac emulator developed in [56]. The emulator is a surrogate cardiac model, built on the basis of LV pressure-volume transients obtained from EM simulations. Thanks to the emulator, it is possible to rapidly calibrate the EM model, decreasing the computational cost needed.

In this work, we apply the previously described model to four patients affected by left bundle branch block (LBBB), who underwent CRT in Ospedale S. Maria del Carmine in Rovereto. Moreover, fibrosis was detected in two of the four patients analysed. All the clinical data considered (i.e. images from MRI, measures from electro-anatomical mapping and LV pressure and volume measures) were provided by Ospedale S. Maria del Carmine.

2 | Clinical data processing

In this chapter, we describe the clinical data used to develop our patient-specific model of the heart function. In particular, we use data from magnetic resonance imaging (MRI), bullseye plot, mechanical measures and electro-anatomical mapping, all of them provided by Ospedale S. Maria del Carmine in Rovereto. Images from MRI have been post-processed in the work of [68], where left ventricle geometries and scarred regions have been reconstructed: these geometries are used as input data for modeling cardiac resynchronization therapy (CRT) in this thesis. Moreover, we use coronary epicardial veins reconstructed by [68] from the electro-anatomic mapping procedure.

2.1. Magnetic resonance imaging

Magnetic resonance imaging (MRI) is a diagnostic tool used to non-invasively visualize tissues and structures inside the body. MRI exploits the great quantity of water present in the body: in fact, water contains two atoms of hydrogen, which has one proton inside the nucleus. If hydrogen protons are subjected to a magnetic field, they align to it, and this the basic principle behind MRI.

MRI systems are mainly composed by a super-conductive magnet, radiofrequency coils, gradient coils and a computer system (See Figure 2.1) [63]. Once the patient is positioned inside the MRI scanner, he or she is subjected to different magnetic fields:

- The super conductive magnet generates a constant magnetic field in all the area of interest, thus aligning hydrogen protons to the magnetic field direction;
- Radiofrequency coils superimpose a varying magnetic field to the one generated by the super conductive magnet. The varying magnetic field is at the resonance frequency of the hydrogen protons: therefore, protons rotate around their axis. Once the varying magnetic field is turned off, protons come back to their original configuration (e.g. aligned with the constant magnetic field), emitting a signal that is collected by radiofrequency coils;
- Gradient coils, that are composed by three sets of coils oriented in three perpen-

dicular directions, produce a varying magnetic field, superimposed to the constant one, in order to spatially encode the protons position.

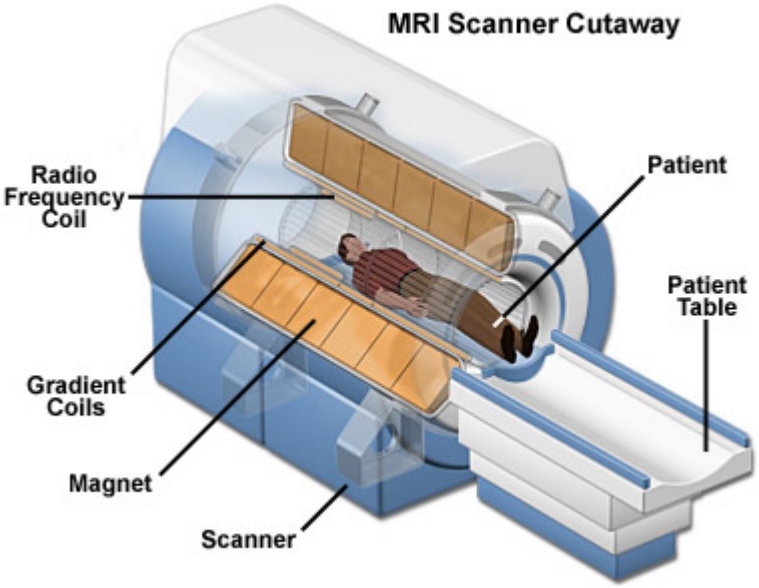

Figure 2.1: Illustration of MRI components. Taken from [41].

The result of the combination of the magnetic fields described above is a set of planar images (called *slices*) colored in grey scale (See Figure 2.2), depending on the amount of hydrogen protons present in that region (whiter regions correspond to a greater quantity of hydrogen protons) [41, 63].

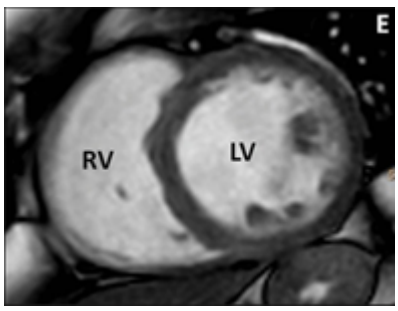

Figure 2.2: Example of slice obtained from MRI. Adapted from [61]. RV: right ventricle, LV: left ventricle.

In the cardiac context, MRI can be used to study cardiovascular morphology, as well as ventricular function [61]. To assess these aspects, it is necessary to synchronize the cardiac scanning with the ECG of the patient, in order to overcome motion artifacts due to respiratory movements and heart contraction. This synchronization is exploited by

cine MRI, a technique that allows to multiply scan the heart during the cardiac cycle. In this way, it is possible to study cardiac function with great precision, displaying the changes in atria and ventricles as well as in ventricular walls.

Another important type of MRI is late gadolinium enhancement MRI (LGE MRI), a technique that allows to characterize cardiac tissue [61]. Gadolinium is a paramagnetic contrast agent, with a specific diffusion kinetic. It is injected intravenously and it is normally washed out by cells in 10-20 minutes. However, in the presence of dead cells, gadolinium is not washed out: these regions result to be brighter with respect to the rest of the image, revealing, in this way, ischemic regions in the heart.

In this thesis, we use left ventricle (LV) geometries reconstructed by [68] from cine MRI images (with and without gadolinium) provided by Ospedale S. Maria del Carmine. In [68], it was performed a segmentation procedure with a semi automatic algorithm, in order to reconstruct LV geometry, distinguishing between the epicardial and the endocardial surface (See Figure 2.3a).

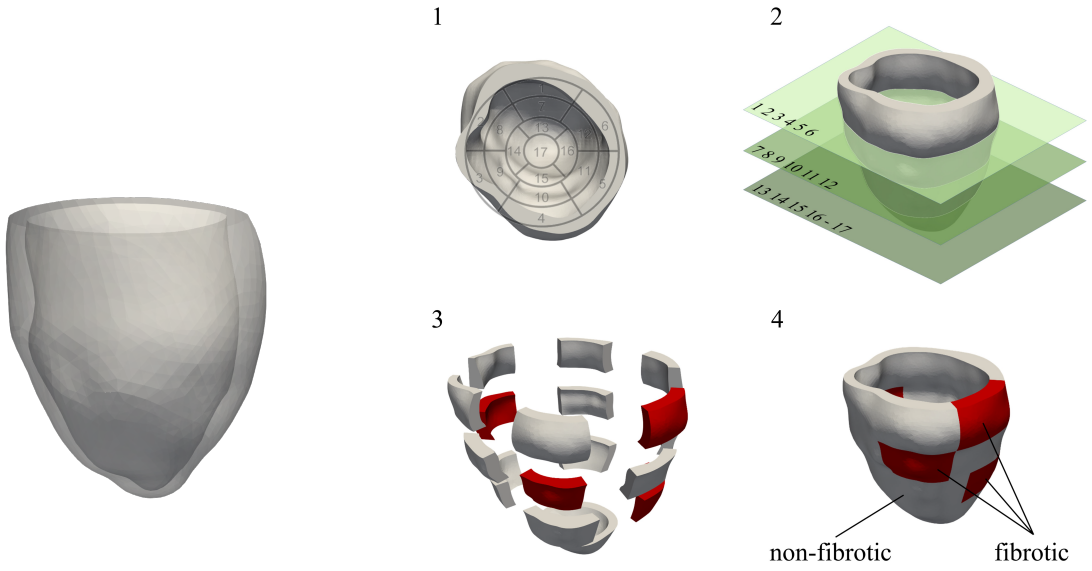

(a) Example of LV geometry reconstructed in [68].

(b) Reconstruction of fibrotic regions. Taken from [68].

Figure 2.3: Example of LV geometry (a) and bullseyeplot (b).

2.2. Bullseye plot

In 2002, American Heart Association introduced a standardized way to segment the left ventricle (LV): the bullseye plot, also called the 17-segment model [14]. The bullseye plot

is a polar plot divided in 17 segments, each one representing a specific region of the LV (See Figure 2.4). In particular, the LV is subdivided longitudinally in four levels (basal, mid, apical and apex zone). The first two levels (e.g. basal and mid zones) are split in six sectors each, while the apical level is divided in four sectors. Each sector represents a specific circumferential location on the ventricle.

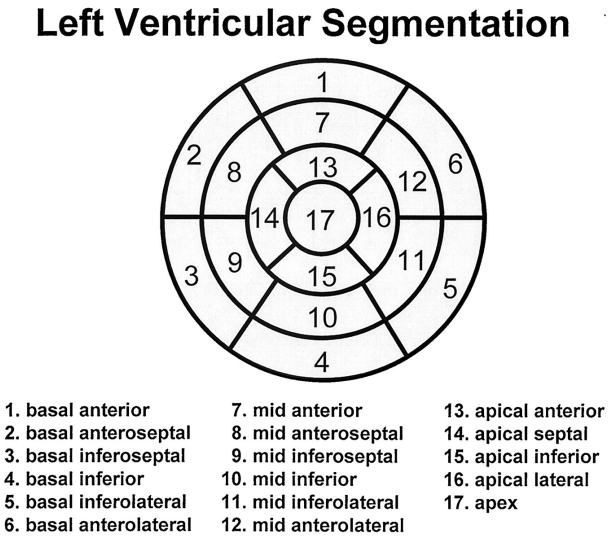

Figure 2.4: Bullseye plot of the left ventricle. Taken from [14].

Each segment is given a name according to its position along the longitudinal and circumferential axis of the heart: for example, segment one is the basal (longitudinal location) anterior (circumferential location) segment.

The bullseye plot can be used to display fibrotic regions present in the LV. As described in Section 2.1, thanks to late gadolinium enhanced magnetic resonance imaging (LGE MRI), it is possible to identify scarred regions: however, LGE MRI is only based on the contrast resolution between areas with and without fibrosis, making difficult the proper identification of scarred regions [61]. To simplify the identification process, the bullseye plot division is used to study every segments of the ventricle, to understand whether or not the fibrosis is present. The radiologist, looking at MRI images and referring to the bullseye plot division, can reveal fibrotic regions.

To integrate the presence of fibrosis in our model, it is necessary to subdivide the reconstructed geometry of the LV according to the bullseye plot division. This was done in [68], in which they divided the LV geometry in regions, assigning each of them a tag value, to identify zones with and without fibrosis (See Figure 2.3b).

2.3. Mechanical measures

In this work, we use mechanical measures (e.g volumes and pressures) provided by Ospedale S. Maria del Carmine to calibrate our heart model.

Volume measures

In this thesis, we include in our model measures of the end systolic volume (ESV) and of the end diastolic volume (EDV) of the left ventricle (LV) (we will only refer to left ventricular volumes) (See also Section 1.1.4). They are defined as the volume of blood remaining in the ventricle after the contraction (ESV) and after the ventricular filling (EDV), respectively [84]. ESV and EDV can be non-invasively measured with magnetic resonance imaging (MRI), in particular with the steady state free precession (SSFP) technique [36], that was used by Ospedale S. Maria del Carmine to provide us volume measures before the implantation of the cardiac resynchronization therapy (CRT) system. In physiologic conditions, EDV ranges from 106-214 mL in men and 86-178 mL in women, while ESV ranges from 26-82 mL in men and 22-66 mL in women [36]. To normalize volume measures, ESV and EDV are often indexed to body surface area (BSA), which is the total surface area of the body. EDV indexed to BSA ranges from 57-105 mL/m^2 in men and 56-96 ml/m^2 in women, while ESV indexed to BSA ranges from 14-38 mL/m^2 in men and 14-34 mL/m^2 in women [36].

Pressure measures

Ideally, left ventricle (LV) pressure should be measured inside the chamber, through the use of a catheter. In practice, this is a very invasive procedure, that is rarely performed in clinics [3]. Therefore, LV pressure is commonly approximated by the measure of arterial blood pressure, which can be easily obtained with the use of a sphygmomanometer. Blood pressure oscillates between two values [84]:

- Systolic pressure: it is the maximum pressure reached by arterial blood during systole, just before the closing of the aortic valve. It normally ranges from 100-140 mmHg;
- Diastolic pressure: it is the minimum pressure reached by arterial blood during diastole, it normally ranges from 60-90 mmHg.

In this thesis, we used systolic and diastolic pressures measured by Ospedale S. Maria del Carmine before the implantation of cardiac resynchronization therapy (CRT). In particu-

lar, in our work diastolic pressure corresponds to the aortic valve opening pressure, while systolic pressure corresponds to the maximum pressure reached by the LV.

2.4. Electrical mapping

Cardiac electrical mapping is a procedure that allows to record the electrical activity of the heart. The latter is represented by the measurement of the local activation time, that can be achieved with two modalities, unipolar or bipolar electrograms [10]. Electrograms record the potential difference between two points: in the unipolar electrogram, the voltage difference is measured from an intracardiac and an extracardiac electrode, while in bipolar electrogram both electrodes are inside the heart. Local activation time is defined differently according to the procedure used to measure it (e.g. unipolar or bipolar electrogram) (See Figure 2.5). If we consider the unipolar electrogram, local activation time is defined as the time needed to reach the maximum (negative) value in the derivative with respect to time of the potential. Instead, for the bipolar electrogram, there are three possible markers used to measure local activation times: the maximum absolute voltage, the maximum absolute slope of voltage and the minimum voltage [10].

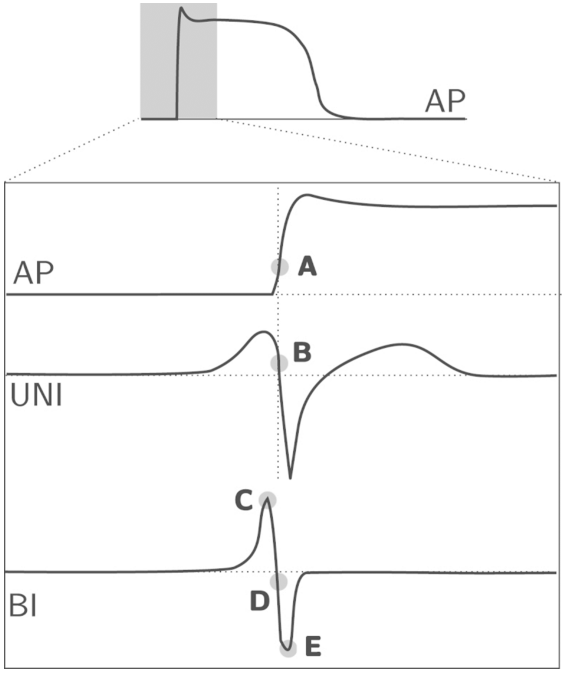

Figure 2.5: Commonly local activation times used. Taken from [10]. AP: action potential, UNI: unipolar electrogram, BI: bipolar electrogram. A, B, C, D, E indicate the points at which local activation time is measured. A: maximum dV/dt, B: maximum negative dV/dt, C: maximum absolute voltage |V|, D: maximum absolute slope |dV/dt|, E: minimum voltage.

In this work, we use electrical measures provided by Ospedale S. Maria del Carmine in Rovereto, taken during the implantation of cardiac resynchronization therapy (CRT) [21, 68]. In particular, to perform cardiac mapping, clinicians used the *EnSite Precision*^{TM} technology, an electro-anatomic mapping system that permits to visualize the position of catheters in the heart chambers and in arteries or veins [21, 55]. First, to perform the cardiac mapping, it is necessary to place three pairs of adhesive electrodes on the patient: the electrodes form the system reference, with the heart in the centre. Specifically, electrodes are placed on patient sides, on chest and back, on the back of the neck and on the inner left thigh, thus generating the X-axis, the Y-axis and the Z-axis, respectively [55]. The three pairs of electrodes generate a low power electrical potential, producing a voltage gradient across the thorax of the patient. When the catheter is moved inside this area, the system analyses the impedance and voltage gradients in order to precisely locate its position, thus generating a 3D navigation field [21, 55]. *EnSite Precision* ^{TM} technology permits to create a 3D map of heart chambers and vasculature structures in real time and without using fluoroscopy, thus reducing X-ray patient exposure. In this context, clinicians from Ospedale S. Maria del Carmine used this system to implant CRT leads: they first created a 3D anatomical map and then they recorded local ventricular activation times in order to find the latest electrically activated segment (LEAS). In particular, they followed this procedure [21]:

- The right ventricular lead was used first to map the superior vena cava, and then to create a 3D map of the right atrium and ventricle. After this, the lead was placed in the apex of the right ventricle;
- An electrophysiological catheter was used to map the coronary sinus and to complete the map of the right atrium. Then, the catheter was removed. The left ventricular lead was inserted: this was used to map the coronary sinus branches and to record the local activation times, in order to find the LEAS. The left ventricular lead was positioned as close as possible to the LEAS;
- Lastly, the right atrial lead was placed in the right auricle.

During this procedure, it is possible to visualize activation maps on the display of the *EnSite Precision* ^{TM} system: in particular, each region mapped is coloured according to the degree of activation time (See Figure 2.6). Thanks to this map, clinicians can place the left ventricular lead at the closest point to the LEAS, compatibly with the vein size and with lead stability.

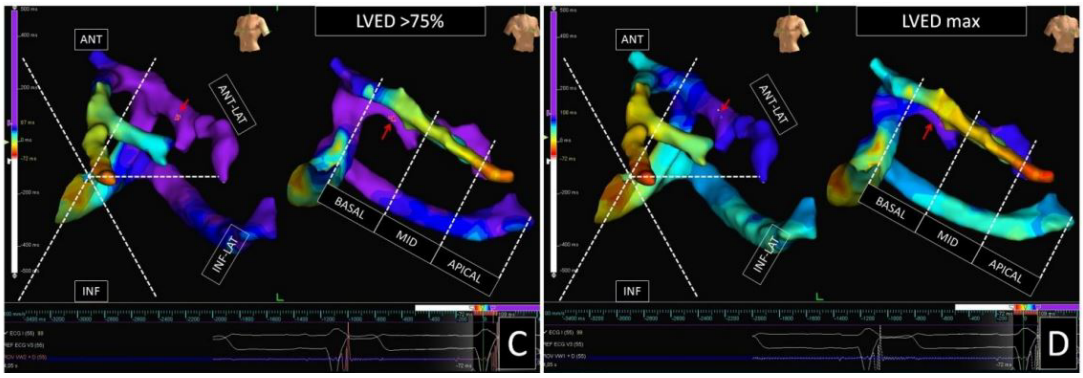

Figure 2.6: Example of activation map obtained through the *EnSite Precision* ^{TM} system. Taken from [22].

Local activation times measured were used in this thesis to calibrate the electrical model of four patients. In particular, clinicians provided us with measures of local activation times taken at the right ventricle septum (not available for all the patients analysed) and at the epicardial coronary veins.

To include these data in the model, it is necessary to merge the electrical measures and the reconstructed geometry of the ventricle, since they belong to two different reference systems, as explained in [69]. In [69], an alignment procedure was performed: the electrical cloud of points was rotated, translated and projected on the surface of the left ventricle (See Figure 2.7).

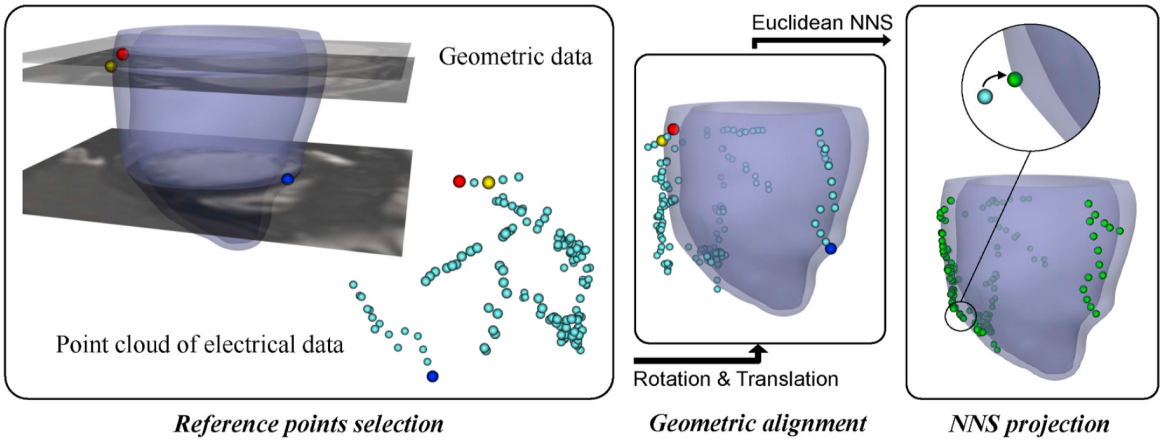

Figure 2.7: The alignment procedure of electrical and geometric data. Taken from [69].

Also, as explained in [68], it is possible to exploit electrical measures to 3D reconstruct the coronary epicardial veins. In particular, they drew the anatomy of the veins by means of splines, a mathematical tool used for interpolations. Figure 2.8 shows an example of

vein reconstruction from the electrical cloud of points. In the next chapters we will see how veins reconstruction can be exploited for CRT modeling.

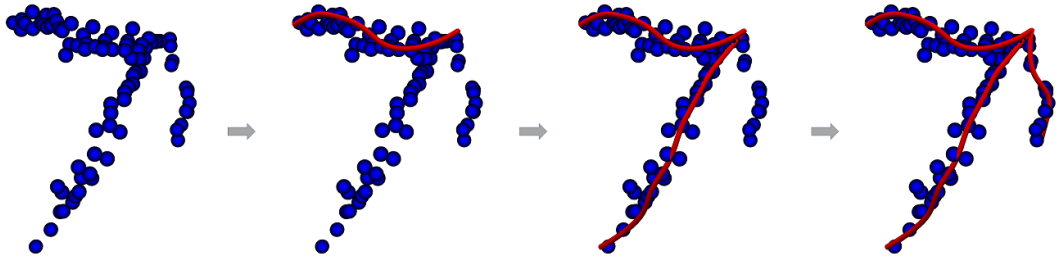

Figure 2.8: Example of vein reconstruction. Taken from [68].

3 | Mathematical and numerical methods

3.1. Mathematical model

The electro-mechanics (EM) model used in this work is the one developed in [70]. The EM model is composed by the reaction-Eikonal model (See Section 1.4.1) for electrophysiology, which is coupled with the RDQ20-MF active force model [57] and the active and passive tissue model, together with a Windkessel model for the systemic circulation. Figure 3.1 summarizes the EM model, which we will deeply discuss.

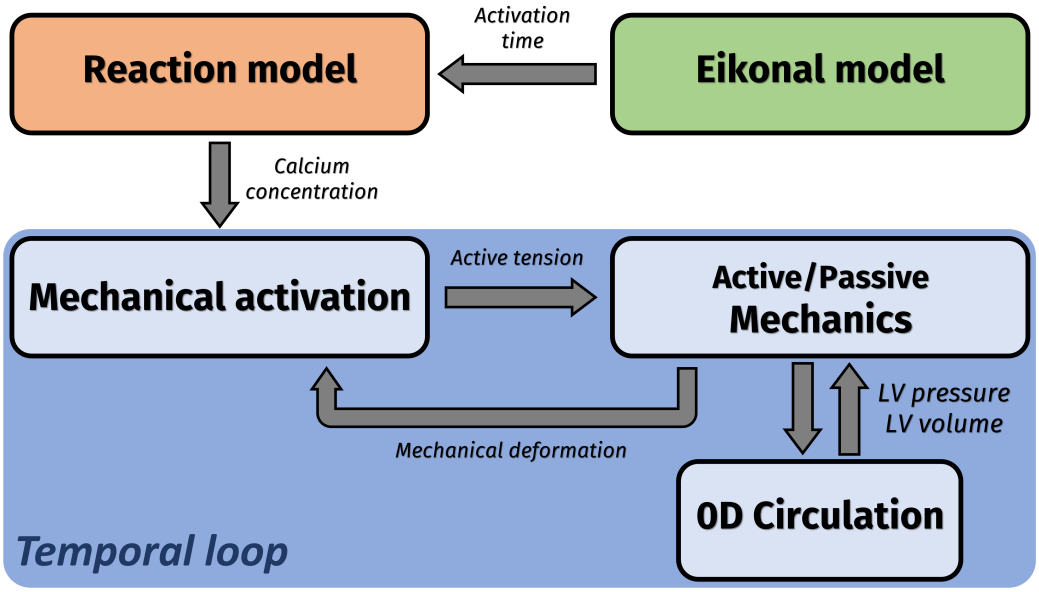

Figure 3.1: Scheme of the electro-mechanics model used. Taken from [70]. First we solve the Eikonal problem, through which we obtain left ventricle activation time. Then, we solve the reaction problem in order to calculate intracellular calcium concentration. Lastly, in a temporal loop we solve the circulation problem, the mechanics problem and the active tension problem.

The EM model is solved in the 3D geometry of the left ventricle (LV): let $\Omega \subset \mathbb{R}^3$ be the left ventricular domain, with $\partial\Omega$ being its boundary, composed by the epicardial surface Γ^{epi}, the endocardial surface Γ^{endo} and the base surface Γ^{base} (See Figure 3.2).

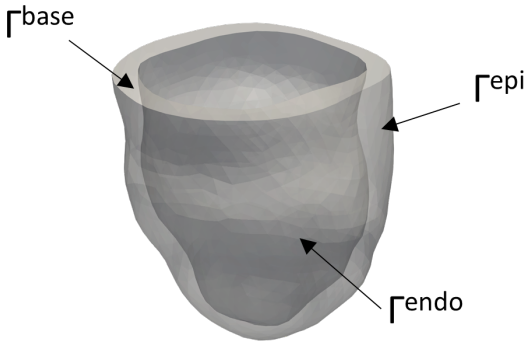

Figure 3.2: Left ventricle domain and surfaces.

3.1.1. Eikonal-diffusion model

Electrical activity of the heart is modeled through the Eikonal-diffusion model, that allows to compute local activation times with a low computational cost. The mathematical formulation of the Eikonal-diffusion model is the following:

Let $\psi : \Omega \to \mathbb{R}$ be the unknown activation time, solution of the Eikonal-diffusion equation:

$$\begin{cases} c_0\sqrt{\nabla\psi \cdot \frac{1}{\chi C_m}\mathbf{D}\nabla\psi} - \varepsilon\nabla\cdot\left(\frac{1}{\chi C_m}\mathbf{D}\nabla\psi\right) = 1 & \text{in } \Omega, \quad (3.1a) \\ \left(\frac{1}{\chi C_m}\mathbf{D}\nabla\psi\right)\cdot\boldsymbol{n} = 0 & \text{on } \partial\Omega \setminus S_a, \quad (3.1b) \\ \psi = \psi_a & \text{on } S_a, \quad (3.1c) \end{cases}$$

where c_0 is a parameter related to the velocity of depolarization wave along the fiber direction for a planar wavefront, χ is the surface to volume ratio, C_m is the transmembrane capacitance and ϵ is a dimensionless parameter. The conductivity tensor $\mathbf{D}$ is defined as

$$\mathbf{D} = z\sigma_s\mathbf{1} + z(\sigma_f - \sigma_s)\boldsymbol{f_0}\otimes\boldsymbol{f_0} + z(\sigma_n - \sigma_s)\boldsymbol{n_0}\otimes\boldsymbol{n_0} \quad (3.2)$$

where σ_f, σ_s and σ_n are the conductivities along the fibers direction $\boldsymbol{f_0}$, the sheets $\boldsymbol{s_0}$ and the normal direction $\boldsymbol{n_0}$, respectively (See Figure 3.3). The parameter $z \in [0, 1]$ is the degree of fibrosis, from scarred tissue ($z = 0$) to physiological one ($z = 1$) [68].

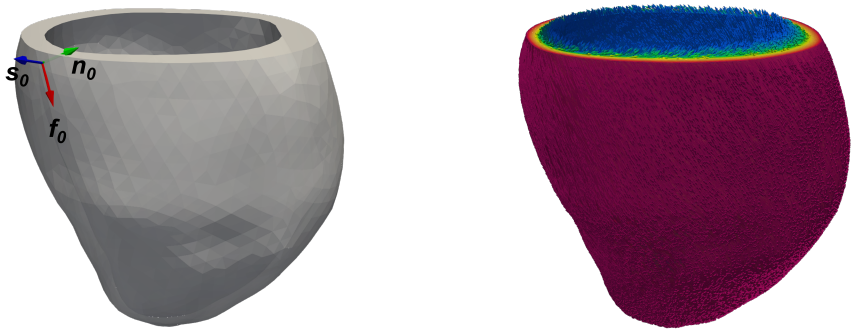

(a) Directions of fibers. (b) Fibers distribution.

Figure 3.3: Left ventricle fibers directions and distribution.

Regarding the boundary conditions (3.1b) and (3.1c), S_a is defined as the portion of the physical boundary where the activation time ψ_a is prescribed, in order to surrogate the Purkinje fibers effect (See also Section 1.1.3). Indeed, in this work Purkinje fibers are not modeled. The vector $\boldsymbol{n}$ is the outward directed unit vector normal to the boundary $\partial\Omega$ of the domain Ω.

3.1.2. Reaction model

Intracellular calcium concentration $[Ca^{2+}]_i$ has to be calculated in order to couple the active force model to the Eikonal one (See Figure 3.1). To reach this goal, we will present the simplified version of the monodomain model (See Section 1.4.1), obtained by neglecting the diffusion term.

Let $u : \Omega \times (0, T_{HB}) \to \mathbb{R}$ be the unknown transmembrane potential and let T_{HB} be the heart beat period; the simplified monodomain problem reads:

$$\begin{cases} \chi\left[C_m \dfrac{\partial u}{\partial t} + I_{\text{ion}}(u, \boldsymbol{w}, \boldsymbol{z})\right] = I_{\text{app}}(t - \psi(\boldsymbol{x})) & \text{in } \Omega \times (0, T_{HB}), \\ \dfrac{d\boldsymbol{w}}{dt} = \boldsymbol{H}(u, \boldsymbol{w}) & \text{in } \Omega \times (0, T_{HB}), \\ \dfrac{d\boldsymbol{z}}{dt} = \boldsymbol{G}(u, \boldsymbol{w}, \boldsymbol{z}) & \text{in } \Omega \times (0, T_{HB}), \end{cases} \tag{3.3}$$

with periodic conditions

$$u(\boldsymbol{x}, T_{HB}) = u(\boldsymbol{x}, 0)$$
$$\boldsymbol{w}(\boldsymbol{x}, T_{HB}) = \boldsymbol{w}(\boldsymbol{x}, 0)$$
$$z(\boldsymbol{x}, T_{HB}) = z(\boldsymbol{x}, 0)$$

for every $\boldsymbol{x} \in \Omega$. $\psi(\boldsymbol{x})$ is the solution of the Eikonal problem (3.1), $I_{ion}(u, \mathbf{w}, z)$ is the ionic current defined accordingly to the chosen ionic model (See Section 3.1.3), $\mathbf{w} : \Omega \times (0, T_{HB}) \to \mathbb{R}^r$ are the gating variables, $z : \Omega \times (0, T_{HB}) \to \mathbb{R}^s$ are the ionic concentrations. The functions $\boldsymbol{H} \in \mathbb{R}^r$ and $\boldsymbol{G} \in \mathbb{R}^s$ are defined accordingly to the specific ionic model. I_{app} is defined as

$$I_{\text{app}}(t) = \begin{cases} \bar{I}_{\text{app}} & \text{if } 0 \leq \text{mod}(t, T_{HB}) < \delta_{\text{stim}}, \\ 0 & \text{otherwise} \end{cases} \tag{3.4}$$

being $\bar{I}_{\text{app}}$ and δ_{stim} suitable prescribed values. The modulo operator mod(.,.) calculates the remainder after the division. Within this simplified monodomain version, the diffusion term is substituted by the term $I_{\text{app}}(t - \psi(\boldsymbol{x}))$, that allows to apply a current in every point $\mathbf{x}$ in a temporal neighborhood of the local activation time $\phi(\boldsymbol{x})$.

To further decrease the computational effort needed to solve equation (3.3), in [70] it was exploited the fact that spatial points are decoupled from each other. Therefore, we solve for each point the following ordinary differential system (ODE):

$$\begin{cases} \chi\left[C_m \dfrac{du^{0D}}{dt} + I_{\text{ion}}(u^{0D}, \boldsymbol{w}^{0D}, \boldsymbol{z}^{0D})\right] = I_{\text{app}}(t) & \text{in } (0, T), \quad (3.5a) \\ \dfrac{d\boldsymbol{w}^{0D}}{dt} = \boldsymbol{H}(u^{0D}, \boldsymbol{w}^{0D}) & \text{in } (0, T), \quad (3.5b) \\ \dfrac{d\boldsymbol{z}^{0D}}{dt} = \boldsymbol{G}(u^{0D}, \boldsymbol{w}^{0D}, \boldsymbol{z}^{0D}) & \text{in } (0, T), \quad (3.5c) \end{cases}$$

imposing the periodic conditions $u^{0D}(T_{HB}) = u^{0D}(0)$, $w^{0D}(T_{HB}) = w^{0D}(0)$ and $z^{0D}(T_{HB}) = z^{0D}(0)$. To find the solution in each point of the domain, the 0D functions u^{0D}, $\boldsymbol{w}^{0D}$ and z^{0D} (that depend on time only) are translated in time according to the activation time of each point $\phi(\boldsymbol{x})$:

$$\begin{aligned} u(\boldsymbol{x}, t) &= u^{0D}(t - \psi((x))), \\ \boldsymbol{w}(\boldsymbol{x}, t) &= \boldsymbol{w}^{0D}(t - \psi((x))), \\ \boldsymbol{z}(\boldsymbol{x}, t) &= \boldsymbol{z}^{0D}(t - \psi((x))). \end{aligned} \tag{3.6}$$

The great innovation in this method is related to the fact that system (3.5) is independent of the spacial coordinates: thus, it can be solved offline, greatly reducing the computational effort needed.

After computing $u, \mathbf{w}, z$, we can identify the calcium intracellular concentration $[Ca^{2+}]_i$ from the variable z:

$$[Ca^{2+}]_i(\boldsymbol{x}, t) = [Ca^{2+}]_i{}^{0D}(t - \psi(\boldsymbol{x})). \tag{3.7}$$

3.1.3. Ionic model

In this work, we use the ToR-ORd ionic model [77], which is an upgraded version of the standard ORd ionic model [48]. The Tor-ORd model is an electrophysiological detailed model of the ventricular cardiomyocyte: intracellular dynamics are described with an high degree of accuracy, being the model based on a series of experimental and clinical datasets. The Tor-ORd model is defined for three types of cells: the endocardial, midmyocardial and epicardial. Each cell is divided in three compartments (main cytosolic space, junctional subspace and sarcoplastic reticulum) where ionic currents and fluxes are modeled, either with an Hodgkin-Huxley equation or with Markov models (See Figure 3.4). The Tor-ORd model defines a total number of 17 ionic currents, making this model one of the most complex and complete one.

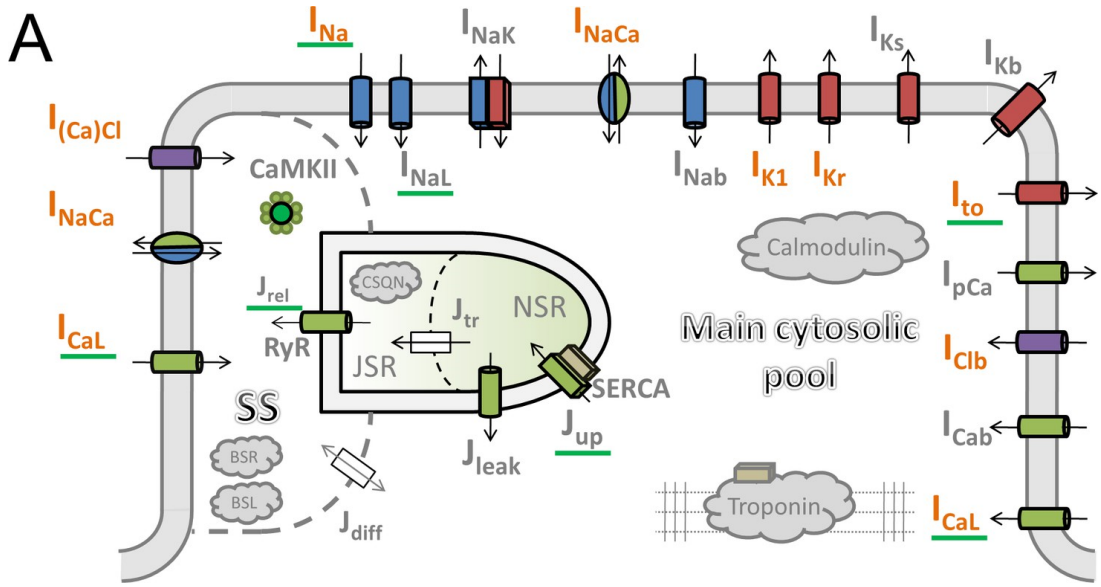

Figure 3.4: Scheme of the Tor-ORd model. Taken from [77]. SS: junctional subspace compartment, JSR: junctional sarcoplastic reticulum compartment, NSR: network sarcoplastic reticulum compartment.

Given its high degree of complexity, in this work we will only propose a possible general

formulation behind the Tor-ORd model, a system of ODE:

$$\begin{cases} J_{ion}(V,t) = J_{Na}(V,Y_{j,i},Z_i,t) + J_K(V,Y_{j,i},Z_i,t) + J_{Ca}(V,Y_{j,i},Z_i,t) + J_b(V,t) \\ \dfrac{\partial Y_{j,i}}{\partial t} = \alpha_j(Y_{i,j}^{\infty} - Y_{i,j}) + \beta_j Y_{j,i} \\ \dfrac{\partial Z_i}{\partial t} = G(V,Z_i,t) \end{cases} \tag{3.8}$$

where J_{ion} is the total ionic flux, sum of the sodium, potassium and calcium fluxes (J_{Na}, J_K, J_{Ca}) plus the background flux J_b. $Y_{j,i}$ is the j-th gating variable related the i-th ion: it is a function the represents the different configurations of ionic channels, from a closed to an open state. More than one gating variable can be associated to a single ion. α_j and β_j are the transition rates, the probability to pass from an ionic channel state (e.g. state a) to another one (e.g. state b) (α_j) and viceversa (from state b to a) (β_j). Y_j^{∞} represents the steady state value of the gating variable Y_j. Other variables involved are the transmembrane potential V, the concentration of the i-th ion Z_i and time t. G is a suitable function for the modeling of ionic concentration.

In this work, we exploit the Tor-ORd model to retrieve intracellular calcium concentration dynamics at different heart rates: in this way, we can include patient-specific heart rates in our model. This a new feature with respect to the works of [11, 68], in which the ten Tusscher-Panfilov ionic model [76] was used. The ten Tusscher-Panfilov model is not able to accurately reproduce calcium dynamics at different heart rates, and thus we decided to switch on the Tor-ORd model.

3.1.4. Mechanical activation model

To model the cardiac active force generation, we use the RDQ20-MF model [57], a biophysically detailed model, that describe the behaviour of proteins involved in the generation of active force (See Section 1.4.1). Being $\boldsymbol{s} : \Omega \times (0,T) \to \mathbb{R}^{20}$ the vectorial functions constituting the 20 state variables of the model, we have:

$$\begin{cases} \dfrac{d\boldsymbol{s}}{dt} = \boldsymbol{K}\left(\boldsymbol{s}, [Ca^{2+}]_i, SL, \dfrac{dSL}{dt}\right) & \text{in } \Omega \times (0,T), \\ \boldsymbol{s}(0) = \boldsymbol{s}_0 & \text{in } \Omega \times \{t=0\}, \end{cases} \tag{3.9}$$

where $\mathbf{K}$ is a suitable function that depends on the state variables, on the intracellular calcium concentration $[Ca_i^{2+}]$ (defined in equation (3.7)), on the sarcomere length SL and on its derivative with respect to time. The state variables are related to the proteins involved in active force generation, e.g. troponin, tropomyosin, actin and myosin.

Sarcomere length is calculated as

$$SL = SL_0\sqrt{I_{4f}} \tag{3.10}$$

where SL_0 is the sarcomere length at rest, while I_{4f} is the fourth invariant, that represents a measure of tissue elongation, being connected to tissue displacement $\boldsymbol{d}$ (See Section 3.1.5).

From the state variables $\boldsymbol{s}$ and sarcomere length SL we can compute the the active tension T_a as

$$T_a = G(\boldsymbol{s}, SL), \tag{3.11}$$

with G being a suitable non linear function.

3.1.5. Active and passive mechanics model

We now present the momentum conservation equation [47] to model cardiac displacement, solution of the elasto-dynamic problem. Let $\boldsymbol{d} : \Omega \times (0,T) \to \mathbb{R}^3$ be the cardiac displacement, we have

$$\begin{cases} \rho\dfrac{\partial^2 \boldsymbol{d}}{\partial t^2} - \nabla \cdot \mathbf{P}(\boldsymbol{d}, T_a) = \mathbf{0} & \text{in } \Omega \times (0,T), \quad (3.12a) \\ \mathbf{P}(\boldsymbol{d}, T_a)\boldsymbol{n} + \mathbf{K}^{\text{epi}}\boldsymbol{d} + \mathbf{C}^{\text{epi}}\dfrac{\partial \boldsymbol{d}}{\partial t} = \mathbf{0} & \text{on } \Gamma^{\text{epi}} \times (0,T), \quad (3.12b) \end{cases}$$

with initial conditions $\boldsymbol{d} = \boldsymbol{d}_0$ and $\frac{\partial \boldsymbol{d}}{\partial t} = \dot{\boldsymbol{d}}_0$ in Ω at $t = 0$. The Piola-Kirchoff stress tensor $\boldsymbol{P} = \boldsymbol{P}(\boldsymbol{d}, T_a)$ is defined as

$$\mathbf{P}(\boldsymbol{d}, T_a) = \frac{\partial \mathcal{W}(\mathbf{F})}{\partial \mathbf{F}} + T_a \frac{\mathbf{F}\boldsymbol{f_0} \otimes \boldsymbol{f_0}}{\sqrt{\mathcal{I}_{4f}}}, \tag{3.13}$$

with $\boldsymbol{F} = \boldsymbol{I} + \nabla \boldsymbol{d}$ being the deformation tensor and $\mathcal{W}$ the strain energy function. The first term of equation (3.13) represents passive tissue mechanics, while the second term represents the active tissue mechanics, since it depends on the active tension T_a, calculated from equation (3.11). It is important to point out that to evaluate the Piola-Kirchoff tensor it is necessary to work in the stress-free configuration of the domain Ω. Therefore, left ventricle geometry reconstructed from clinical images has to be deflated by blood pressure, to get a stress-free configuration.

The fourth invariant I_{4f} is defined as $I_{4f} = \boldsymbol{F}\boldsymbol{f}_0 \cdot \boldsymbol{F}\boldsymbol{f}_0$ (See Figure 3.3): as mentioned in Section 3.1.4, it is a measure of tissue elongation, since it depends on $\boldsymbol{F}$ which in

turn depends on the displacement $\boldsymbol{d}$. The strain energy function $\mathcal{W}$ is defined as in the Guccione model $\mathcal{W}(\boldsymbol{F}) = \frac{C}{2}(e^Q - 1)$, with the right Cauchy-Green deformation tensor $C = \boldsymbol{F}^T\boldsymbol{F}$ and Q defined as in [27].

Equation (3.12b) is the boundary condition that models the interaction between the left ventricle and the pericardium, defining the stiffness tensor $\boldsymbol{K}^{epi}$ and the viscosity tensor $\boldsymbol{C}^{epi}$

$$\begin{aligned} \mathbf{K}^{\text{epi}} &= K_{\perp}^{\text{epi}}(\boldsymbol{n}\otimes\boldsymbol{n}) + K_{\parallel}^{\text{epi}}(\mathbf{I} - \boldsymbol{n}\otimes\boldsymbol{n}), \\ \mathbf{C}^{\text{epi}} &= C_{\perp}^{\text{epi}}(\boldsymbol{n}\otimes\boldsymbol{n}) + C_{\parallel}^{\text{epi}}(\mathbf{I} - \boldsymbol{n}\otimes\boldsymbol{n}), \end{aligned} \tag{3.14}$$

where $K_{\perp}^{\text{epi}}$, $K_{\parallel}^{\text{epi}}$, $C_{\perp}^{\text{epi}}$ and $C_{\parallel}^{\text{epi}}$ are positive constant values of stiffness and viscosity of the epicardium in the normal and tangent directions.

Boundary conditions at the endocardium and at the base are the following:

$$\begin{cases} \mathbf{P}(\boldsymbol{d}, T_a)\boldsymbol{n} = -p_{LV}(t)J\mathbf{F}^{-T}\boldsymbol{n} & \text{on } \Gamma^{\text{endo}} \times (0,T), \quad (3.15a) \\ \mathbf{P}(\boldsymbol{d}, T_a)\boldsymbol{n} = p_{LV}(t)|J\mathbf{F}^{-T}\boldsymbol{n}|\boldsymbol{v}^{\text{base}}(t) & \text{on } \Gamma^{\text{base}} \times (0,T). \quad (3.15b) \end{cases}$$

Equations (3.15a) and (3.15b) allow to couple the active and passive mechanics model with the 0D hemodynamic model (See Section 3.1.6). In particular, $p_{LV}(t)$ is the blood pressure obtained from the 0D model. The term

$$\boldsymbol{v}^{\text{base}}(t) = \frac{\int_{\Gamma^{\text{endo}}} J\mathbf{F}^{-T}\boldsymbol{n}\, d\Gamma}{\int_{\Gamma^{\text{base}}} \|J\mathbf{F}^{-T}\boldsymbol{n}\|\, d\Gamma} \tag{3.16}$$

permits to introduce an energy-consistent boundary condition. Another coupling condition with the 0D circulation model is given by the calculation of the left ventricle volume, that is obtained from the solution of the mechanics problem ((3.12)):

$$V_{LV}^{3D}(t) = \int_{\Gamma^{\text{endo}}} J(t)((\boldsymbol{h}\otimes\boldsymbol{h})(\boldsymbol{x} + \boldsymbol{d}(t) - \boldsymbol{b})) \cdot \mathbf{F}^{-T}(t)\boldsymbol{n}\, d\Gamma \tag{3.17}$$

where $\boldsymbol{d}$ is the displacement, $\boldsymbol{h}$ a vector lying on the base of the left ventricle and $\boldsymbol{b}$ the vectorial coordinate of a point inside the left ventricle.

3.1.6. Circulation model

Lastly, we model hemodynamics with a 0D model, as done in the work [58]. The circulation model is coupled with the mechanics one by equations (3.15) and equation (3.17), that respectively impose LV pressure and volume continuity. In particular, we have $p_{LV}^{0D} = p_{LV}$ and $V_{LV}^{0D} = V_{LV}^{3D}$.

The cardiac cycle is modeled by four phases (See also Section 1.1.4):

1. Isovolumetric contraction: imposing $V_{LV}^{0D} = EDV$, with EDV being the end diastolic volume (a measure provided by clinicians), the momentum conservation equation (3.12) is solved. The pressure p_{LV}^{0D} is calculated as the Lagrange multiplier that strengthens the constraint imposed on the left ventricle volume;

2. Ejection: when ventricular pressure reaches a prescribed fixed value of pressure ($\bar{p}_{AVO}^{0D}$, at time instant t_{AVO}), aortic valve opens. Blood is pushed out until the flow becomes retrograde, causing the closing of the aortic valve at the time instant t_{AVC}. Left ventricular pressure is modeled by a two-element Windkessel model [81]:

$$C\frac{dp_{LV}^{0D}}{dt} + \frac{1}{R}p_{LV}^{0D} = \frac{dV_{LV}^{0D}}{dt} \qquad t \in (t_{\text{AVO}}, t_{\text{AVC}}), \tag{3.18}$$

   where R is the total peripheral resistance, while C is the total arterial compliance. The ejection phase ends when $\frac{dV_{LV}^{0D}}{dt}$ becomes positive: this means that the left ventricle volume stops decreasing, because of retrograde blood flows. The end of the ejection phase determines $p_{LV}^{0D}(t_{AVC}) = \bar{p}_{AVC}^{0D}$. Both t_{AVO} and t_{AVC} are unknown, while $\bar{p}_{AVO}^{0D}$ is obtained from clinical datas (See Section 2.3). V_{LV}^{0D} is calculated exploiting equation (3.17) of the mechanics model.

3. Isovolumetric relaxation: as in the first phase, the mechanical problem (3.12) is solved imposing $V_{LV}^{0D} = ESV$, where ESV is the end systolic volume, the volume of the ventricle at the very end of phase 2. While the volume is kept constant, the pressure decreases until $p_{LV}^{0D} = \bar{p}_{MVO}^{0D}$, where $\bar{p}_{MVO}^{0D}$ is the prescribed pressure value for the opening of the mitral valve;

4. Filling: left ventricular volume is linearly increased until it reaches the prescribed value, e.g the EDV.

We have to point out that, differently from the work of [11, 68], phase four of cardiac cycle is modeled with a volume-ramp instead of a pressure-ramp. Even if it would be more physiological to linearly increase pressure, in this work we decided to linearly increase volume in order to simplify the calibration process needed to develop our patient-specific models, as we will explain in the next sections.

3.2. Numerical approximation

The electro-mechanics model described in the previous sections has been numerically solved in [70] with a segregated method, based on a loosely-coupled strategy for the

couplings between mechanics and active force model and between mechanics and the circulation model. Regarding time discretization, the reaction problem and the mechanics problem were solved by means of the Backward Differentiation Formula (BDF) of order 1. Ionic concentrations and gating variables were treated with an Implicit Explicit (IMEX) scheme, while the active force generation model was discretized with a forward Euler scheme. Eventually, space discretization was implemented through the Finite Element Method (FEM) of order 1 on hexahedral meshes. To solve the final linear system arising from the FEM, the GMRES method was used, preconditioned with the AMG preconditioner. All the numerical methods have been implemented within `life`$^{\mathtt{x}}$, a high performance C++ finite element library, with focus on cardiac applications.

3.2.1. Solution of the Eikonal-diffusion problem

The numerical discretization of the Eikonal-diffusion model can be obtained by first transforming equation (3.1a) in a parabolic equation by introducing a pseudo time term and then looking for a steady-state solution [68, 70]. In this way, once we have spatially discretized equation (3.1a), the parabolic term introduces a mass matrix, that helps in reaching convergence when solving the system with the Newton method.

Problem (3.1a) can become a parabolic one by adding the partial derivative with respect to time of the activation time:

$$\frac{\partial \psi}{\partial \tau} + c_0 \sqrt{\nabla \psi \cdot \frac{1}{\chi C_m} \mathbf{D} \nabla \psi} - \varepsilon \nabla \cdot \left(\frac{1}{\chi C_m} \mathbf{D} \nabla \psi \right) = 1 \qquad \text{in } \Omega \times (0, \tilde{T}] \tag{3.19}$$

where τ is the pseudo-time and $\tilde{T}$ is the time instant at which the steady solution is reached. Equation (3.1a) is solved adding a parabolic term, since, in this way, we add a mass matrix that helps reaching convergence

To discretize in time equation (3.21), we subdivide the time interval $(0, \tilde{T})$ in N subintervals (τ^n, τ^{n+1}), such that $\tau^{n+1} = (n+1)\Delta\tau^n$, with $n = 0, ..., N-1$. Approximating the discretized solution as $\psi^{n+1} \approx \psi(\tau^{n+1})$, we have

$$\frac{\psi^{n+1} - \psi^n}{\Delta \tau} + c_0 \sqrt{\nabla \psi^{n+1} \cdot \frac{1}{\chi C_m} \mathbf{D} \nabla \psi^{n+1}} - \varepsilon \nabla \cdot \left(\frac{1}{\chi C_m} \mathbf{D} \nabla \psi^{n+1} \right) = 1 \qquad \text{in } \Omega \tag{3.20}$$

applying the fully implicit backward Euler method and with initial condition $\psi^0 = \psi_0$. The stopping criterion (related to the pseudo time term) used to calculate the asymptotic

solution of the problem is the following:

$$||\psi^{n+1} - \psi^n||_{L^2(\Omega)} < \text{tol}$$

where tol is the tolerance set at 10^{-10}.

Regarding spatial discretization, we report the final non-linear system obtained applying the Galerkin formulation and introducing the scalar basis functions φ:

$$\begin{cases} M\dfrac{\boldsymbol{\psi}_h^{n+1} - \boldsymbol{\psi}_h^n}{\Delta\tau} + \boldsymbol{m}(\boldsymbol{\psi}_h^{n+1}) + A\boldsymbol{\psi}_h^{n+1} = \boldsymbol{f} \\ \boldsymbol{\psi}_h^0 = \boldsymbol{\psi}_{h,0} \end{cases} \tag{3.21}$$

where $\boldsymbol{\psi}_h$ is the solution vector of the system. Equation (3.21) is solved with the Newton algorithm.

We define matrix elements as

$$(M)_{ij} = \int_\Omega \varphi_j \varphi_i \, d\Omega, \tag{3.22}$$

$$(A)_{ij} = \varepsilon \int_\Omega \mathbf{D}\nabla\varphi_j \cdot \nabla\varphi_i \, d\Omega, \tag{3.23}$$

and vector elements as

$$(\boldsymbol{m}(\boldsymbol{\psi}_h^{n+1}))_j = c_0 \int_\Omega \sqrt{\nabla\boldsymbol{\psi}_h^{n+1} \cdot \frac{1}{\chi C_m}\mathbf{D}\nabla\boldsymbol{\psi}_h^{n+1}}\varphi_j \, d\Omega, \tag{3.24}$$

$$(\boldsymbol{f})_j = \int_\Omega \varphi_j \, d\Omega + \int_{S_a} \psi_a \varphi_j \, dS_a. \tag{3.25}$$

3.2.2. Solution of the reaction problem

The reaction problem is discretized in time as follows:

$$\begin{cases} u_{0D}^{n+1} = u_{0D}^n - \dfrac{\Delta t}{C_m}\left(I_{\text{ion}}(u_{0D}^n, \boldsymbol{w}_{0D}^n, \boldsymbol{z}_{0D}^n) - \dfrac{I_{\text{app}}^n}{\chi}\right), & \text{(3.26a)} \\ \boldsymbol{w}_{0D}^{n+1} = \boldsymbol{w}_{0D}^n + \Delta t \boldsymbol{H}(u_{0D}^n, \boldsymbol{w}_{0D}^{n+1}), & \text{(3.26b)} \\ \boldsymbol{z}_{0D}^{n+1} = \boldsymbol{z}_{0D}^n + \Delta t \boldsymbol{G}(u_{0D}^n, \boldsymbol{w}_{0D}^n, \boldsymbol{z}_{0D}^n). & \text{(3.26c)} \end{cases}$$

Equation (3.26a) was discretized with the Backward Differentiation Formula (BDF) of order 1, while equations (3.26b) and (3.26c) were discretized with the first order implicit-explicit (IMEX) scheme. In particular, ionic concentrations, that have a non-linear dy-

namics, are treated explicitly. In this way, we avoid solving a non-linear system and we do not compromise the stability of the solution, being equation (3.5c) non-stiff. On the other hand, gating variables are treated implicitly, since equation (3.5b) is linear: therefore, it is possible to use an implicit scheme without solving a non-linear system.

Once we solve system (3.26), we can retrieve intracellular calcium concentration $[Ca^{2+}]_i^{0D}$. Then, exploiting equations (3.6) and (3.7), we can compute and interpolate in time the intracellular calcium concentration for every point of the domain to get $[Ca^{2+}]_{i,h}^{n+1}$.

3.2.3. Solution of the mechanical activation problem

The time discretization of the mechanical activation problem can be achieved by using the forward Euler scheme. In particular, partitioning the time interval (0, T) in N subintervals (t^n, t^{n+1}), such that $t^{n+1} = (n+1)\Delta t$, and approximating $\boldsymbol{s}^{n+1} \approx \boldsymbol{s}(t^{n+1})$, we have:

$$\begin{cases} \boldsymbol{s}^{n+1} = \boldsymbol{s}^n + \Delta t \boldsymbol{K}\left(\boldsymbol{s}^n, [Ca^{2+}]_i^n, SL^n, \dfrac{dSL^n}{dt}\right) & \text{in } \Omega \\ \boldsymbol{s}^0 = \boldsymbol{s}_0 & \text{in } \Omega \end{cases} \tag{3.27}$$

The active tension can be computed as

$$\begin{cases} T_a^{n+1} = G(\boldsymbol{s}^{n+1}, SL^n) \\ T_a^0 = T_{a,0} \end{cases} \tag{3.28}$$

where we approximated $T_a^{n+1} \approx T_a(t^{n+1})$.

For stability purposes the mechanical activation problem a requires a smaller Δt with respect to the mechanics problem.

Regarding spatial discretization, the Galerkin formulation is the following (with $\boldsymbol{\varphi}$ being the vector basis functions):

$$\begin{cases} M\boldsymbol{S}_h^{n+1} = M\boldsymbol{S}_h^n + \Delta t \widetilde{\boldsymbol{K}}\left(\boldsymbol{S}_h^n, [Ca^{2+}]_{i,h}^n, SL_h^n, \dfrac{dSL_h^n}{dt}\right) \\ \boldsymbol{S}_h^0 = \boldsymbol{S}_{h,0} \end{cases} \tag{3.29}$$

with

$$\begin{cases} T_{a,h}^{n+1} = G(\boldsymbol{S}_h^{n+1}, SL_h^n) \\ T_{a,h}^0 = T_{a,h,0}. \end{cases} \tag{3.30}$$

being $\boldsymbol{S_h}$ the unknown solution vector. M is the mass matrix given by

$$(M)_{ij} = \int_\Omega \boldsymbol{\varphi}_j \cdot \boldsymbol{\varphi}_i \, d\Omega \tag{3.31}$$

and vector $\widetilde{\boldsymbol{K}}$ is

$$(\widetilde{\boldsymbol{K}}(\mathbf{S}_h^n))_i = \int_\Omega \boldsymbol{K}\left(\boldsymbol{s}_h^n, [Ca^{2+}]_{i,h}^n, SL_h^n, \frac{dSL_h^n}{dt}\right) \cdot \boldsymbol{\varphi}_i \, d\Omega. \tag{3.32}$$

3.2.4. Solution of the tissue mechanics problem

Time discretization of the mechanics problem is performed by dividing the time interval $(0, T)$ in N subintervals (t^n, t^{n+1}), with $n = 0, ..., N-1$, such that $t^{n+1} = (n+1)\Delta t$. Exploiting the Backward Differentiation Formula (BDF) of order 1, and approximating $\boldsymbol{d}^{n+1} \approx \boldsymbol{d}(t^{n+1})$, $p_{LV}^{n+1} \approx p_{LV}(t^{n+1})$ and $\boldsymbol{v}^{base,n+1} \approx \boldsymbol{v}^{base}(t^{n+1})$, we have:

$$\begin{cases} \rho\dfrac{\boldsymbol{d}^{n+1} - 2\boldsymbol{d}^n + \boldsymbol{d}^{n-1}}{\Delta t^2} - \nabla \cdot \mathbf{P}(\boldsymbol{d}^{n+1}, T_a^{n+1}) = \mathbf{0} & \text{in } \Omega, \quad (3.33a) \\ \mathbf{P}(\boldsymbol{d}^{n+1}, T_a^{n+1})\boldsymbol{n} + \mathbf{K}^{\text{epi}}\boldsymbol{d}^{n+1} + \mathbf{C}^{\text{epi}}\dfrac{\boldsymbol{d}^{n+1} - \boldsymbol{d}^n}{\Delta t} = \mathbf{0} & \text{on } \Gamma^{\text{epi}}, \quad (3.33b) \\ \mathbf{P}(\boldsymbol{d}^{n+1}, T_a^{n+1})\boldsymbol{n} = -p_{LV}^{n+1} J\mathbf{F}^{-T}\boldsymbol{n} & \text{on } \Gamma^{\text{endo}}, \quad (3.33c) \\ \mathbf{P}(\boldsymbol{d}^{n+1}, T_a^{n+1})\boldsymbol{n} = p_{LV}^{n+1} |J\mathbf{F}^{-T}\boldsymbol{n}| \boldsymbol{v}^{\text{base, n+1}} & \text{on } \Gamma^{\text{base}}, \quad (3.33d) \end{cases}$$

with initial conditions $\boldsymbol{d}^0 = \boldsymbol{d}_0$ and $\frac{\partial \boldsymbol{d}}{\partial t}^0 = \dot{\boldsymbol{d}}_0$. In system (3.33), we reported the momentum conservation equation (3.33a), together with the bondary conditions at the epicardium (3.33b), at endocardium (3.33c) and at the base (3.33d).

Eventually, being $\boldsymbol{D}_h$ the vector of unknowns and $\boldsymbol{\varphi}$ the vectorial basis functions, the Galerkin formulation of the mechanics problem is the following:

$$\rho M\frac{\boldsymbol{D}_h^{n+1} - 2\boldsymbol{D}_h^n + \boldsymbol{D}_h^{n-1}}{\Delta t^2} + C\frac{\boldsymbol{D}_h^{n+1} - \boldsymbol{D}_h^n}{\Delta t} + K\mathbf{D}_h^{n+1} + \boldsymbol{P}(\mathbf{D}_h^{n+1}, T_{a,h}^{n+1}) = p_{LV}^{n+1}\boldsymbol{p}(\mathbf{D}_h^{n+1}) \tag{3.34}$$

with initial conditions $\boldsymbol{D}_h^0 = \boldsymbol{D}_{h,0}$ and $\frac{\partial \boldsymbol{D}_h}{\partial t}^0 = \dot{\boldsymbol{D}}_{h,0}$. Matrices and vectors are defined as:

$$(M)_{ij} = \int_\Omega \boldsymbol{\varphi_j} \cdot \boldsymbol{\varphi_i} \, d\Omega, \tag{3.35}$$

$$(C)_{ij} = \int_\Omega \mathbf{C}^{\text{epi}}\boldsymbol{\varphi_j} \cdot \boldsymbol{\varphi_i} \, d\Gamma, \tag{3.36}$$

$$(K)_{ij} = \int_\Omega \mathbf{K}^{\text{epi}} \boldsymbol{\varphi_j} \cdot \boldsymbol{\varphi_i} \, d\Gamma, \tag{3.37}$$

$$(\boldsymbol{P}(\mathbf{D}_h^{n+1}, T_{a,h}^{n+1}))_j = \int_\Omega P(\boldsymbol{d}_h^{n+1}, T_{a,h}^{n+1}) : \nabla \boldsymbol{\varphi}_j \, d\Omega, \tag{3.38}$$

$$(\boldsymbol{p}(\mathbf{D}_h^{n+1}))_j = \int_{\Gamma^{\text{base}}} |J_h \mathbf{F}_h^{-T} \boldsymbol{n}| \boldsymbol{v}_h^{\text{base, n+1}} \cdot \boldsymbol{\varphi}_j \, d\Gamma - \int_{\Gamma^{\text{endo}}} J_h \mathbf{F}_h^{-T} \boldsymbol{n} \cdot \boldsymbol{\varphi}_j \, d\Gamma. \tag{3.39}$$

The non-linear equation (3.34) is solved by means of the Newton algorithm.

3.2.5. Solution of the circulation problem

We now address the discretization of the coupling between the circulation model and the mechanics model. Briefly, we solve for each time step t^{n+1} the circulation model, retrieving the left ventricle pressure needed by the mechanics model. Exploiting the updated pressure, we then solve the mechanics problem. Referring to the four phases of the cardiac cycle described in Section 3.1.6, we can discretize the circulation/mechanics problem as follows:

1. Isovolumetric contraction: given the initial conditions $\boldsymbol{D}_h^0 = \boldsymbol{D}_{h,0}$, $p_{LV}^{0D,0} = \bar{p}_{ED}^{0D}$ and $V_{LV}^{0D,0} = EDV$, find $(\boldsymbol{D}_h^{n+1}, p_{LV}^{0D,n+1})$ such that:

$$\begin{cases} V_{LV}^{0D,n+1} = V_{LV}^{0D,n} \\ \text{Solve the mechanics problem (3.34) and retrieve } \boldsymbol{D}_h^{n+1}. \end{cases} \tag{3.40}$$

   until $p_{LV}^{0D,n+1} = \bar{p}_{AVO}^{0D}$ at $t^{n+1} = t_{AVO}$;

2. Ejection: applying the backward Euler method on the two-element Windkessel model, we have: find $p_{LV}^{0D,n+1}$ such that

$$p_{LV}^{0D,n+1} = \frac{RC}{RC + \Delta t} p_{LV}^{0D,n} + \frac{R}{RC + \Delta t}(V_{LV}^{0D,n+1} - V_{LV}^{0D,n}) \tag{3.41}$$

   until

$$\frac{V_{LV}^{0D,n+1} - V_{LV}^{0D,n}}{\Delta t}$$

   changes its sign at time instant t_{AVC}, where $p_{LV}^{0D}(t_{AVC}) = \bar{p}_{AVC}^{0D}$. $V_{LV}^{0D,n+1}$ is computed explicitly discretizing equation (3.17):

$$V_{LV}^{0D,n+1} = \int_{\Gamma^{\text{endo}}} J_h^n((\boldsymbol{h} \otimes \boldsymbol{h})(\boldsymbol{x} + \boldsymbol{D}_h^{n+1} - \boldsymbol{b})) \cdot \mathbf{F}_h^{-T,n} \boldsymbol{n} \, d\Gamma. \tag{3.42}$$

   Then, Solve the mechanics problem (3.34) and retrieve $\boldsymbol{D}_h^{n+1}$;

3. Isovolumetric relaxation: given $p_{LV}^{0D}(t_{AVC}) = \bar{p}_{ED}^{0D}$, $\boldsymbol{D}_h(t_{AVC})$ with the initial value $V_{LV}^{0D}(t_{AVC}) = ESV$, find $(\boldsymbol{D}_h^{n+1}, p_{LV}^{0D,n+1})$ such that:

$$\begin{cases} V_{LV}^{0D,n+1} = V_{LV}^{0D,n} \\ \text{Solve the mechanics problem (3.34) and retrieve } \boldsymbol{D}_h^{n+1} \end{cases} \tag{3.43}$$

   until $p_{LV}^{0D,n+1} = \bar{p}_{MVO}^{0D}$, at time instant $t^{n+1} = t_{MVO}$;

4. Filling: linearly increase $V_{LV}^{0D,n+1}$ until $V_{LV}^{0D,n+1} = EDV$. Then, Solve the mechanics problem (3.34) and retrieve $\boldsymbol{D}_h^{n+1}$;

In systems (3.40) and (3.43), the constraint on volumes leads to a saddle-point problem, that is solved with the Schur complement reduction [5, 58].

We summarize the numerical solution of the electro-mechanics (EM) model proposed by [68, 70] by means of Algorithm 3.1: by setting $N = \frac{T}{\Delta t}$ the total number of time steps, we have:

Algorithm 3.1 Summary of the numerical solution of the EM model

Given ψ_a, Solve the Eikonal-diffusion problem (3.21)
Solve the reaction problem (3.26) and retrieve intacellular calcium concentration
for $0 \leq n < N$ **do**
  Interpolate in time calcium concentration to get $[Ca^{2+}]_{i,h}^n$
  Solve the active tension problem (3.29)-(3.30) to compute $T_{a,h}^{n+1}$
  if isovolumetric contraction **then**
    Compute $(\boldsymbol{D}_h^{n+1}, p_{LV}^{0D,n+1})$ such that:

$$\begin{cases} V_{LV}^{0D,n+1} = V_{LV}^{0D,n} \\ \text{Solve the mechanics problem (3.34) and retrieve } \boldsymbol{D}_h^{n+1} \end{cases}$$

    until $p_{LV}^{n+1} = \bar{p}_{AVO}$
  else if ejection **then**
    Solve the Windkessel problem (3.41) to compute $p_{LV}^{0D,n+1}$, until $\frac{V_{LV}^{0D,n+1} - V_{LV}^{0D,n}}{\Delta t}$ changes its sign
    Solve the mechanics problem (3.34) and retrieve $\boldsymbol{D}_h^{n+1}$
  else if isovolumetric relaxation **then**
    Compute $(\boldsymbol{D}_h^{n+1}, p_{LV}^{0D,n+1})$ such that:

$$\begin{cases} V_{LV}^{0D,n+1} = V_{LV}^{0D,n} \\ \text{Solve the mechanics problem (3.34) and retrieve } \boldsymbol{D}_h^{n+1} \end{cases}$$

    until $p_{LV}^{n+1} = \bar{p}_{MVO}$
  else if filling **then**
    Linearly increase $V_{LV}^{0D,n+1}$ until $V_{LV}^{0D,n+1} = EDV$.
    Solve the mechanics problem (3.34) and retrieve $\boldsymbol{D}_h^{n+1}$
  end if
end for

3.3. Calibration procedure

In this work, to simulate cardiac resynchronization therapy (CRT), we first model the pre-operative condition, before the CRT implant, as proposed by [11, 68]. To reach this goal, we exploit electrical and mechanical measures (taken before CRT implant) to calibrate our electro-mechanics (EM) model (See Chapter 2).

We can subdivide the calibration procedure in two phases:

1. Electrical calibration: we exploit measures from electro-anatomic mapping (See Section 2.4) to calibrate the Eikonal model, selecting proper tissue conductivity parameters to match activation times measured before the implant of CRT;
2. Mechanical calibration: the procedure consists in calibrating the circulation model and the active force generation model to reproduce pressure-volume (PV) tracings measured before the CRT implant. To speed up the process, we exploit the cardiac 0D emulator developed by [56].

3.3.1. Electrical calibration

To electrically calibrate our EM model, we follow this procedure:

1. To generate cardiac fibers, we set the left ventricle apex coordinate and fibers orientation angles, as required by the Bayer-Trayanova algorithm [4];
2. We estimate the Eikonal-diffusion parameters trying to fit electrical measures we have at disposal. When available, activation times taken at the septum are used as input datum for the model, while measures at the epicardial veins are the ones we want to reproduce by calibrating the Eikonal model;
3. In case of fibrosis, we simulate different degree of fibrosis in terms of dampened electrical conduction in correspondence of the regions identified in the bullseye and we choose the configuration that best matches the electrical measures taken at the epicardial veins.

We will now deeply discuss each point presented.

Fibers reconstruction

To realistically model electrical propagation, in our work we use the Bayer-Trayanova algorithm, a rule-based method that allows to assign cardiac fibers orientation [4] (See Section 1.4.1). The algorithm requires to set the left ventricle apex coordinate and the fibers and sheets angles, at the epicardium and endocardium (See Figure 3.3). In this thesis, as proposed by [68], for every simulation we set -60° for fibers at the epicardium, 60° for fibers at endocardium, -20° for sheets at epicardium and 20° for sheets at endocardium.

Calibration of the Eikonal-diffusion problem

The Eikonal-diffusion problem (See Section 3.2.1) is characterized by seven parameters: the surface to volume ratio χ, the transmembrane capacitance C_m, the velocity of de-

polarization wave c_0, the dimensionless parameter ϵ and the three conductivities σ_f, σ_s and σ_n. In this work, as proposed by [11, 68], for every simulation we set the surface to volume ratio $\chi = 10^5\ m^{-1}$ and transmembrane capacitance $C_m = 0.01\ F/m^2$. The other five parameters are calibrated for every patient treated, in order to fit activation times clinically measured. To calibrate the Eikonal-diffusion model, we have to first prescribe ψ_a, a term needed to surrogate the Purkinje fibers effect, since they are not present in this model. As in [11, 68], ψ_a is represented by the locations and activation times recorded at the septum through the electro-anatomic mapping. When septum measures are not available, three arbitrary points are selected at the septum, so that they can be used as input datum for the Eikonal problem.

Once prescribed ψ_a, we have to estimate ϵ, c_0 and the conductivities to reproduce the electrical measures taken at the coronary epicardial veins. We start by running a preliminary simulation with the values calibrated for the Zygote 3D Solid Heart [85], that are reported in Table 3.1. Notice that conductivities are normalized to the surface to volume ratio and to the transmembrane capacitance: we denote with $\hat{\sigma}_i = \frac{\sigma_i}{\chi C_m}$ the normalized conductivity in one of the fibers direction $\boldsymbol{f_0}, \boldsymbol{s_0}$ and $\boldsymbol{n_0}$, with $i = \{f, s, n\}$. We then compare the computed activation times with the electrical measures at the coronary epicardial veins, changing the Eikonal parameters in order to fit clinical data. In particular, we modify the three conductivities by the same factor, knowing that higher conductivity values correspond to lower activation times, and vice versa. Also, it is possible to change the standard values of c_0 and ϵ: increasing c_0 and/or decreasing ϵ results in lower activation times. The calibration procedure is therefore performed without using any numerical optimization method.

To quantify the discrepancy between the computed values and the measured values, we calculate the relative error between computed activation time t_i^{comp} and measured activation time t_i^{clin} as follows:

$$e[\%] = \frac{1}{N_v T^{clin}} \sum_{i=1}^{N_v} |t_i^{clin} - t_i^{comp}| \cdot 100 \tag{3.44}$$

where N_v is the number of activation times clinically recorded and T^{clin} is the maximum activation time recorded. We keep on adjusting Eikonal parameters until we reach a small relative error (at least less than 10%).

In patients with scarred tissue, we have to estimate the additional parameter z, which represent the degree of fibrosis (See Equation (3.2)). In particular, $z = 1$ corresponds to physiological conditions, while $z = 0$ to scarred tissue, where no electrical signal is

conducted. In this thesis, we simulate different degrees of fibrosis, in the range of $z \in [0.9, 0.5]$: in this way, instead of setting to zero the conductivities, we only decrease them by a certain factor. Then, we follow the procedure explained above for every degree of fibrosis simulated and we choose the configuration with the smallest relative error.

The pseudo time step used to solve the Eikonal model is $\Delta\tau = 0.01s$, with final time $\tilde{T} = 10s$. We remark that the unit of measure of the pseudo time step τ has no physical meaning.

Eikonal model				
c_0	ϵ	$\hat{\sigma}_f$	$\hat{\sigma}_s$	$\hat{\sigma}_n$
$[s^{-\frac{1}{2}}]$	[-]	$[m^2 s^{-1}]$	$[m^2 s^{-1}]$	$[m^2 s^{-1}]$
73.3627646	14.9502645	$0.7643 \cdot 10^{-4}$	$0.3494 \cdot 10^{-4}$	$0.1125 \cdot 10^{-4}$

Table 3.1: Standard Eikonal parameters for the Zygote 3D Solid Heart [85].

3.3.2. Mechanical calibration

The mechanical calibration procedure can be briefly summarized as follows:

1. To include in our model the cardiac frequency of each patient studied, we retrieve intracellular calcium concentrations from the Tor-ORd ionic model, defined for the endocardial cell;
2. We estimate the total peripheral resistance R of the Windkessel model (3.18) and the contractility a_{XB} of the activation model (3.9) to reproduce pressure-volume (PV) tracings clinically recorded. To speed-up the calibration procedure, we exploit the 0D cardiac emulator developed by [56].

Parameters of the activation model, of the mechanics model and of the Windkessel model

To mechanically calibrate our model, we have to set the parameters related to the active force generation model, the mechanics model and the Windkessel model. The reference values [57, 68, 70, 85] of the main physical constants of the three models are reported in Table 3.2, Table 3.3 and Table 3.4.

RDQ20-MF model								
a_{XB}	SL_0	$\bar{k}_d$	α_{k_d}	γ	k_{off}	k_{basic}	$\mu^0_{f_\mathcal{P}}$	$\mu^1_{f_\mathcal{P}}$
$[MPa]$	$[\mu m]$	$[\mu M]$	$[\mu M \mu m^{-1}]$	[-]	$[s^{-1}]$	$[s^{-1}]$	$[s^{-1}]$	$[s^{-1}]$
$1.6 \cdot 10^6$	2.2	0.381	-0.571	12	100	13	32.653	0.778

Table 3.2: Reference parameters of the RDQ20-MF model. Taken from [59, 85].

Mechanics model			
$K^{\text{epi}}_{\perp}$	$K^{\text{epi}}_{\parallel}$	$C^{\text{epi}}_{\perp}$	$C^{\text{epi}}_{\parallel}$
$[Pa\ m^{-1}]$	$[Pa\ m^{-1}]$	$[Pa\ s\ m^{-1}]$	$[Pa\ s\ m^{-1}]$
$2 \cdot 10^5$	$2 \cdot 10^4$	$2 \cdot 10^4$	$2 \cdot 10^3$

Table 3.3: Reference parameters of the mechanics model. Taken from [68, 70].

Windkessel model					
C	R	$\bar{p}^{0D}_{AVO}$	$\bar{p}^{0D}_{MVO}$	$\bar{p}^{0D}_{ED}$	EDV
$[Pa^{-1}\ m^3]$	$[Pa\ s\ m^{-3}]$	$[mmHg]$	$[mmHg]$	$[mmHg]$	$[mL]$
$4.5 \cdot 10^{-9}$	$5 \cdot 10^7$	83	5	10	120

Table 3.4: Reference parameters of the Windkessel model. Taken from [85].

Regarding the RDQ20-MF model [57], we will only modify the crossbridge stiffness a_{XB}, a parameter representing the myocardial contractility, to match clinical data. Concerning the mechanics model, all the parameters in Table 3.3 will be fixed for every patient. Lastly, in the Windkessel model we will change the total peripheral resistance R, the aortic valve opening pressure $\bar{p}^{0D}_{AVO}$ and the end diastolic volume EDV. The mitral valve opening pressure $\bar{p}^{0D}_{MVO}$ and the end diastolic pressure $\bar{p}^{0D}_{ED}$ will be adjusted for every patient to avoid problems with the convergence of the simulation.

General procedure of the mechanical calibration

The purpose of the mechanical calibration is reproducing the PV loop tracings clinically measured for every patient. In particular, we have at disposal measures of the end diastolic volume EDV_{clin}, the end systolic volume ESV_{clin}, the diastolic pressure $p_{diastolic}$ and the systolic pressure $p_{systolic}$ (See Section 2.3). In our work, systolic and diastolic pressures are considered approximated measures of the left ventricle maximum pressure and of the aortic valve opening pressure, respectively.

To calibrate the model, we follow this procedure:

1. EDV and $\bar{p}^{0D}_{AVO}$ are set once and for all to be equal to the clinically measured EDV_{clin} and to the diastolic pressure $p_{diastolic}$ (that corresponds to aortic valve opening pressure), respectively;

2. The crossbridge stiffness a_{XB} and the resistance R are modified in order to fit the clinical data, i.e. the systolic pressure $p_{systolic}$ (that corresponds to the left ventricle maximum pressure) and ESV_{clin}. In particular, as shown by [68], increasing the contractility a_{XB} results in lower ESV values and in an increase in the computed maximum left ventricle pressure $\bar{p}_{max}$ (See Figure 3.5). On the other hand, an increment in the resistance value causes the increase of both $\bar{p}_{max}$ and ESV.

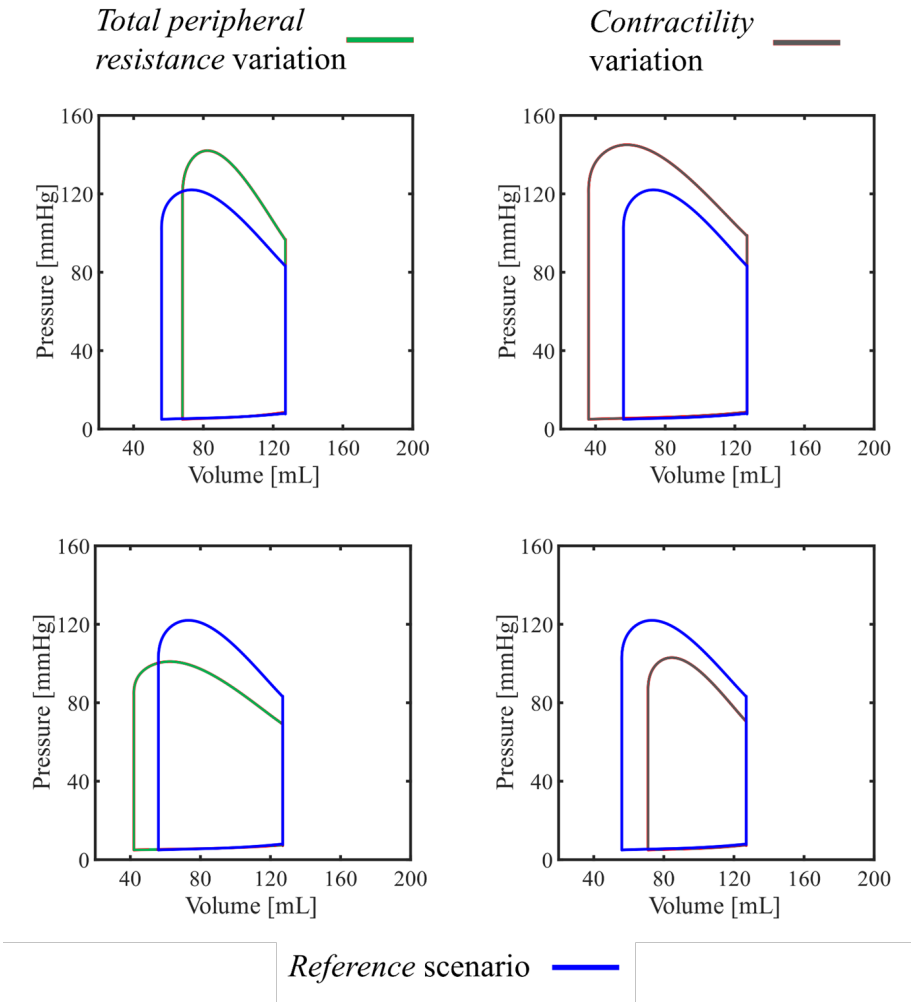

Figure 3.5: Effect of the increase (top) and of the decrease (bottom) of the total peripheral resistance and of the contractility. Taken from [68]. The loops are compared with the blue reference scenario.

The 0D cardiac emulator

The mechanical calibration requires to run the Eikonal-reaction-mechanics (ERM) model every time a parameter is changed, thus it can become a very long procedure. Indeed, an ERM simulation takes $5 \sim 8$ hours, since we have to simulate two heartbeats to reach convergence, as shown by [68]. To speed-up the calibration procedure, we exploit the 0D cardiac emulator developed by [56]. The emulator is a surrogate cardiac model, built basing on a data-driven approach: indeed, the emulator is based on some PV loop samples obtained from the 3D EM model. The emulator is defined by three functions: the end-systolic pressure-volume relationship $\mathcal{P}_{ES}$, that represents the maximum pressure achievable by the ventricle at a given volume, the end-diastolic pressure-volume relationship $\mathcal{P}_{ED}$, that represents the passive properties of the left ventricle (See Section 1.1.4) and the activation kinetics φ_{act}. The latter is a time-dependent function that ideally is equal to zero at the end of diastole, while it is equal to one at the end of systole. These three functions (i.e. $\mathcal{P}_{ES}$, $\mathcal{P}_{ED}$, φ_{act}) have to be constructed to build the emulator. In particular, in our work we construct the emulator in this way:

1. We run two 3D EM simulations, that differ only from the parameter a_{XB};
2. We construct the 0D emulator for each simulation, fitting $\mathcal{P}_{ES}$, $\mathcal{P}_{ED}$ and φ_{act} on the PV loop of the second heartbeat simulated (See Figure 3.6);
3. We build a parametric emulator, interpolating between the two emulators previously built.

Once we have built the parametric 0D emulator, we can exploit it to calibrate our model. In particular, we can modify the total peripheral resistance R and the contractility a_{XB}, evaluating their effects on the cardiac emulator built, with a very low computational cost.

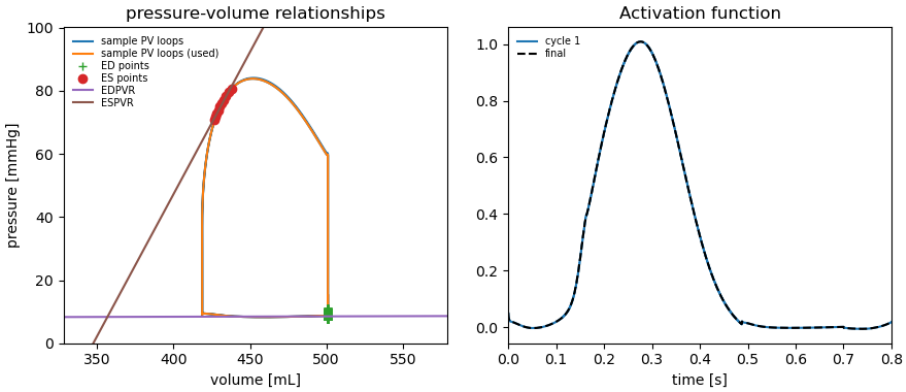

Figure 3.6: Construction of the 0D emulator. ED: end diastolic, ES: end systolic, EDPVR: end-diastolic pressure-volume relationship, ESPVR: end-systolic pressure-volume relationship. On the left we fit $\mathcal{P}_{ES}$ and $\mathcal{P}_{ED}$, while on the right we fit φ_{act}. We sample the second heartbeat simulated (orange curve on the left, black dotted curve on the right). Green crosses and red dots indicate the points used to reconstruct EDPVR and ESPVR, respectively.

In Figure 3.7, we report the PV loop obtained from the 0D parametric emulator and the corresponding PV loop from the 3D simulation (i.e. the PV loop obtained with the same parameters set in the emulator). We can observe that the two curves do not coincide: however, the difference between the two PV loops is quite small. Indeed, in this case the ESV computed by the emulator differs only by the 1.3% with respect to one computed in the 3D simulation, while the maximum pressure of the 0D emulator differs by the 4.1%. Therefore, we can use the emulator to estimate R and a_{XB}, and then we can run few simulations to precisely adjust the parameters. In this way, we can greatly reduce the number of simulations needed to calibrate the model.

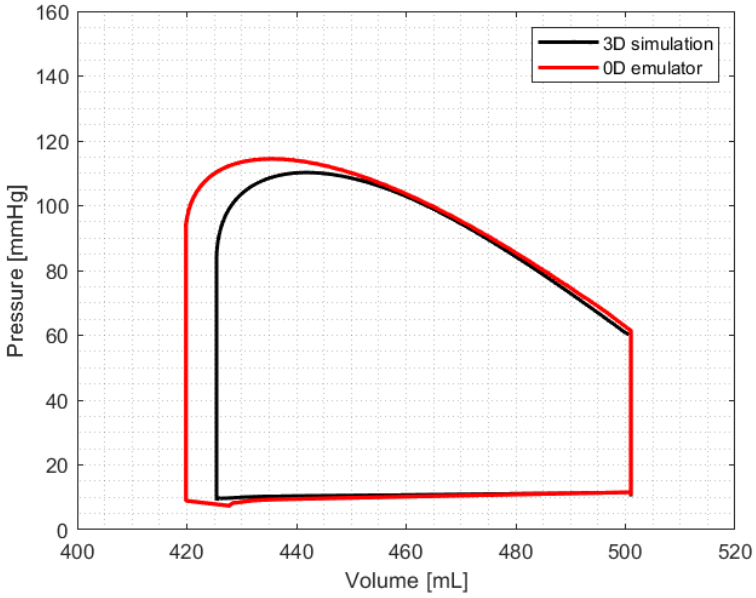

Figure 3.7: Comparison between the PV loop obtained from the 0D emulator and from the 3D simulation.

The time step used to solve the global problem is $\Delta t = 10^{-4}\ s$, while for the active generation model we use $\Delta t = 2.5 \cdot 10^{-5}\ s$ (See Section 3.2.3).

4 | Results of the calibration in the pre-operative scenario

In this chapter we will analyse the numerical results obtained after performing the calibration procedure explained in Section 3.3. The calibration procedure is needed to model the pre-operative condition, fitting the clinical data we have at disposal. In Chapter 5, we will explain how the pre-operative scenario will be used to model cardiac resynchronization therapy (CRT).

We studied four patients, indicated as P2, P3, P8 and P11, whose clinical data were provided by Ospedale S. Maria del Carmine in Rovereto. All the electro-mechanics (EM) simulations were performed by using the high performance finite element library `life`^{x}.

This chapter is structured as follows:

- In Section 4.1, we will report the left ventricle geometry and bullseye plot reconstructed by [68]. Also, we will show the left ventricle meshes used in our EM model. Moreover, we will report the epicardial vein reconstructed by [68], together with the electrical cloud points obtained from the electro-anatomic mapping procedure, explained in Section 2.4;
- In Section 4.2, we will report the results of the calibration procedure, subdivided in the electrical calibration (Section 4.2.1) and the mechanical calibration (Section 4.2.2).

4.1. Geometry

Left ventricle geometry and bullseyeplot

We report the left ventricle geometries reconstructed by [68], used in this thesis (See Section 2.1). Figure 4.1 shows also the bullseye plot reconstructed for each patient by [68]: black areas indicate scarred regions (See section 2.2). As we can notice, only P8 and P11 have fibrotic regions.

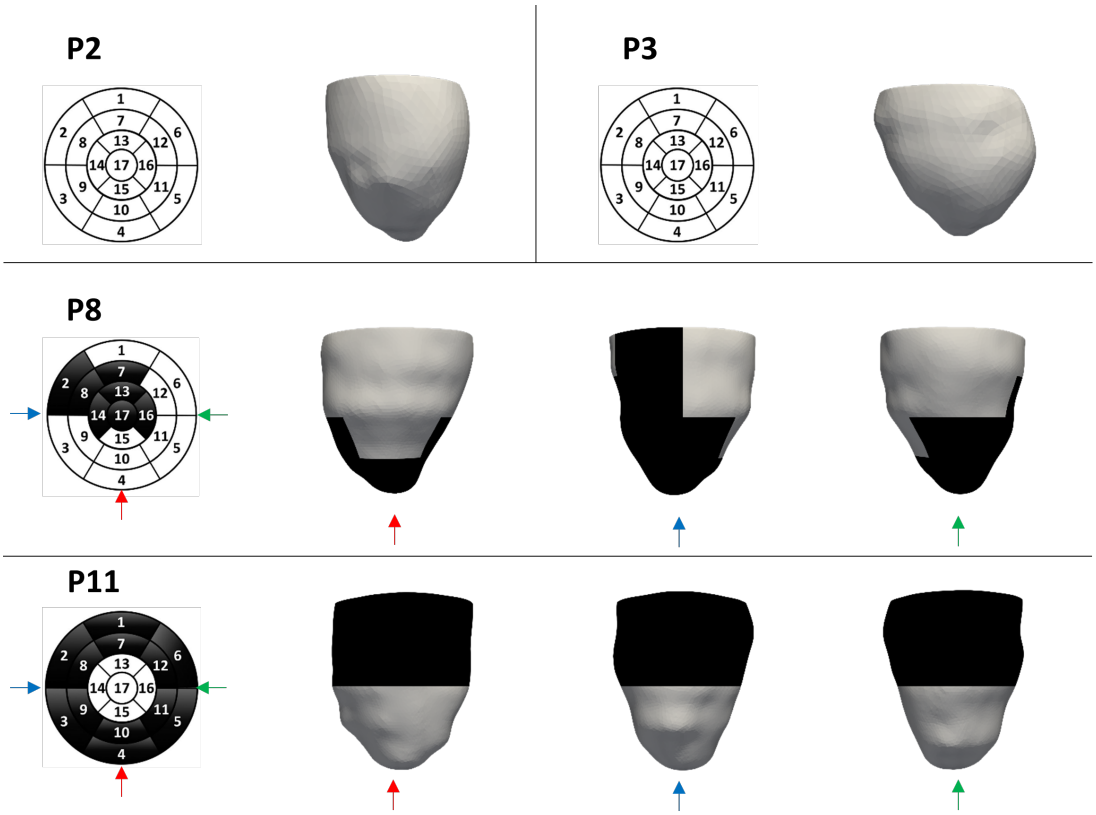

Figure 4.1: Reconstruction of left ventricle geometries and bullseye plot. Modified from [68]. Black regions indicate the scarred tissue, while white regions indicate the healthy tissue.

Left ventricle mesh

To include in our electro-mechanics (EM) model the geometries previously presented, we need to generate their corresponding hexahedral meshes. As explained in [70], the Eikonal model has to be solved on a finer mesh with respect to the active force generation model and to the mechanics model. In this way, we can ensure the convergence of the Eikonal problem. The characteristic mesh size h of the Eikonal problem is indeed $h \simeq 0.8-1\ mm$, while for the mechanical activation problem and for the mechanics problem we have $h \simeq 3-4\ mm$. These characteristic mesh sizes were found to be suitable to model the electrical and mechanical problem in [68, 70].

The finer mesh is generated by uniformly refining the coarser one. Specifically, every hexahedral of the coarser mesh is split in eight subelements, until the desired characteristic mesh size is reached. As we can notice, the characteristic mesh size of the coarser mesh is almost four times greater with respect to the finer one: therefore, the refining process has two be carried out two times. This procedure is performed within `life`^{x}, when solving

the Eikonal problem.

The coarser mesh of every patient studied is generated with the `vmtk` software. In particular, P2 and P8 meshes were generated by [11, 68], while P3 and P11 meshes are generated in this work. We first generate a triangular surface mesh, that is then converted to a tetrahedral mesh. If we have reached the desired characteristic mesh size, we transform the tetrahedral mesh in a hexahedral mesh [24]. In Figure 4.2, we report the fine and coarse meshes of P2, P3, P8 and P11.

Activation times and epicardial vein reconstruction

To integrate in our EM model activation times measured through the electro-anatomic mapping, it is necessary to merge the left ventricle geometries and the electrical measures, since they belong to two different reference system. As mentioned in Section 2.4, in [68] an alignment procedure was performed: we now report the results obtained, showing the electrical cloud of points taken at the coronary epicardial vein and at the septum (See Figure 4.3). We point out that septum data were not available for P8 and P11, therefore three arbitrary points selected at the septum were used as input datum for the Eikonal problem.

In Figure 4.3, we also show the coronary epicardial veins reconstructed by [68]. As described in Section 2.4, in [68] epicardial veins were reconstructed with an interpolation procedure, exploiting the electrical cloud of points obtained with the electro-anatomic mapping.

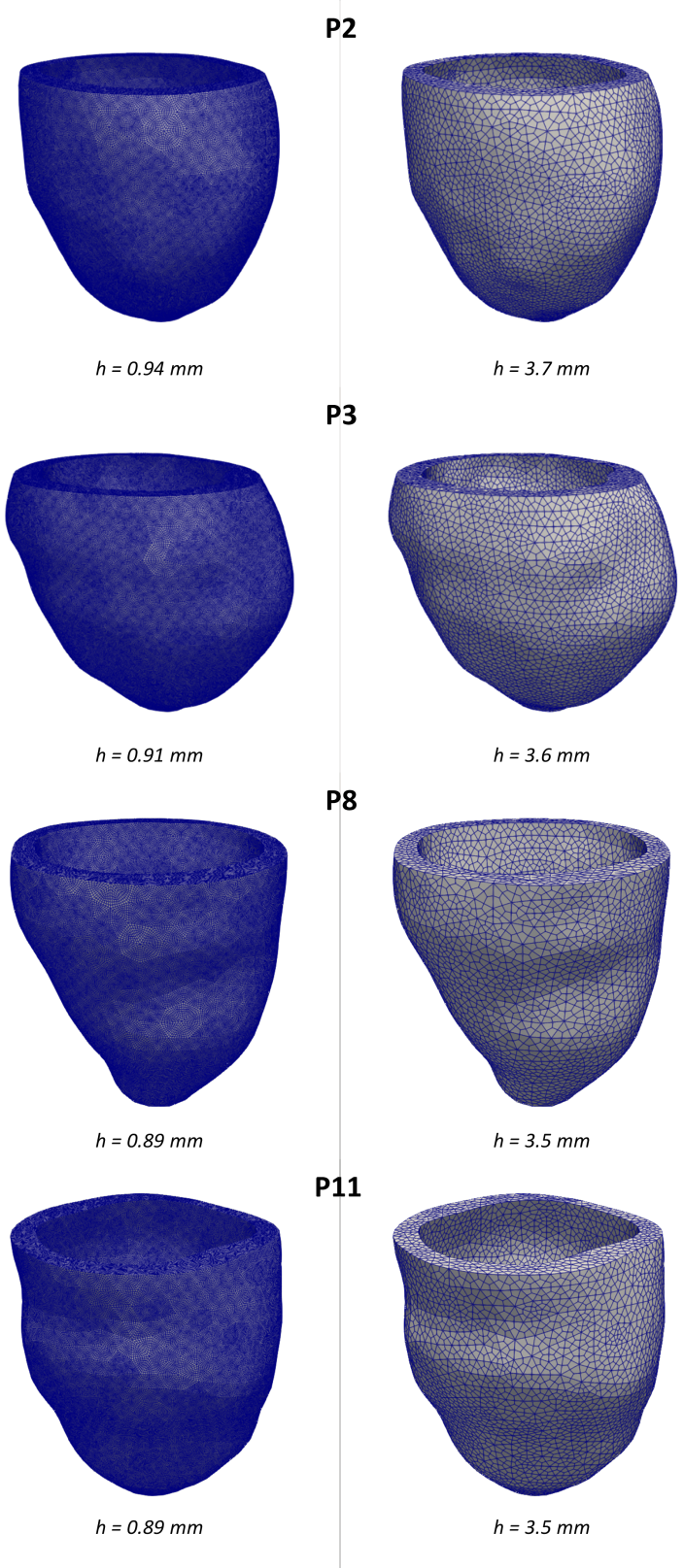

Figure 4.2: Meshes of P2, P3, P8 and P11. On the left the finer mesh, used to solve the Eikonal problem, on the right the coarser one, used to solve the mechanics problem and the active force generation problem.

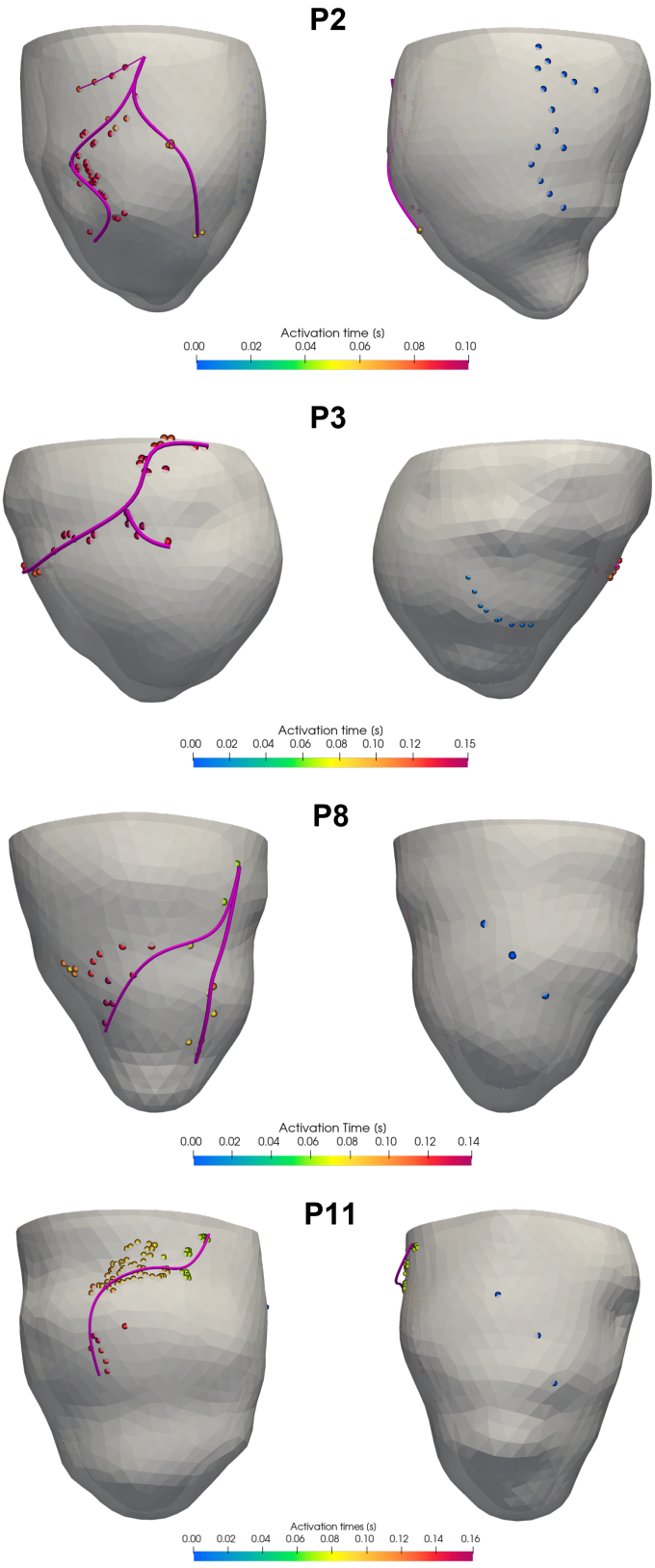

Figure 4.3: Activation times recorded at the coronary epicardial veins (left) and at the septum (right). The reconstructed epicardial veins are highlighted in fuchsia.

4.2. Results of the calibration procedure

In this section, we show the results of the electrical and mechanical calibration, whose procedure is explained in Section 3.3. The calibration is needed to model the pre-operative condition of P2, P3, P8 and P11. As we will deeply explain in Section 5.1, the pre-operative condition has to be modeled in order to simulate CRT.

4.2.1. Results of the electrical calibration

We report in Table 4.1 the Eikonal parameters calibrated for patients P2, P3, P8 and P11. For P2 and P8, we exploited the calibration already performed by [11]. We recall that the electrical calibration consists in estimating five parameters: the velocity of depolarization wave c_0, the dimensionless parameter ϵ and the three conductivities σ_f, σ_s and σ_n (See Section 3.3.1). The parameter z represents the degree of fibrosis: it is used to reduce the conductivity values in the regions where fibrosis is detected. Indeed, $z = 1$ indicates healthy tissue, while $z < 1$ corresponds to scar tissue. As we can notice from Table 4.1, z is set to one in P2 and P3, who do not have fibrotic regions, while z is lower than one in P8 and P11, who were found to have scarred regions (See Section 4.1). The parameter e in Table 4.1 indicates the relative error between computed and measured activation times (See Equation (3.44)).

	c_0 $[s^{-\frac{1}{2}}]$	ϵ [-]	$\hat{\sigma}_f$ $[m^2s^{-1}]$	$\hat{\sigma}_s$ $[m^2s^{-1}]$	$\hat{\sigma}_n$ $[m^2s^{-1}]$	z [-]	e [%]
P2	84.37	11.96	$2.29{\cdot}10^{-4}$	$1.05{\cdot}10^{-4}$	$0.34{\cdot}10^{-4}$	1.0	4.0
P3	73.36	14.95	$1.99{\cdot}10^{-4}$	$0.91{\cdot}10^{-4}$	$0.29{\cdot}10^{-4}$	1.0	6.1
P8	80.70	14.95	$1.91{\cdot}10^{-4}$	$0.87{\cdot}10^{-4}$	$0.28{\cdot}10^{-4}$	0.7	9.9
P11	73.36	14.95	$1.57{\cdot}10^{-4}$	$0.72{\cdot}10^{-4}$	$0.23{\cdot}10^{-4}$	0.9	4.6

Table 4.1: Results of the electrical calibration.

We show in Figure 4.4 the fibers reconstructed with the Bayer-Trayanova algorithm [4], as described in Section 3.3.1. Thanks to this algorithm, we can reconstruct fibers orientation to realistically model the propagation of the electrical signal.

In Figure 4.5, we show the activation times computed with the parameters reported in Table 4.1.

As we can notice from Figure 4.5, there is a good correspondence between computed and measured activation times. Indeed, also calculated errors reported in Table 4.1 are

small, being all the errors lower than 10%. Only in P8 we can notice a little discrepancy between the simulation and activation times measured: indeed, P8 has a relative error of 9.9% (See Table 4.1), the greatest among the four patients studied. A possible explanation could be related to the presence of fibrotic regions: indeed, we simulate scarred regions by uniformly decreasing conduction velocities by the factor z. However, conduction velocities may vary inside the fibrotic regions, being faster or slower in some points.

In Figure 4.5, we highlighted with a black dot the computed latest electrically activated segment (LEAS), identified on the epicardial veins. This point will be used to simulate CRT, as we will see in the next chapter.

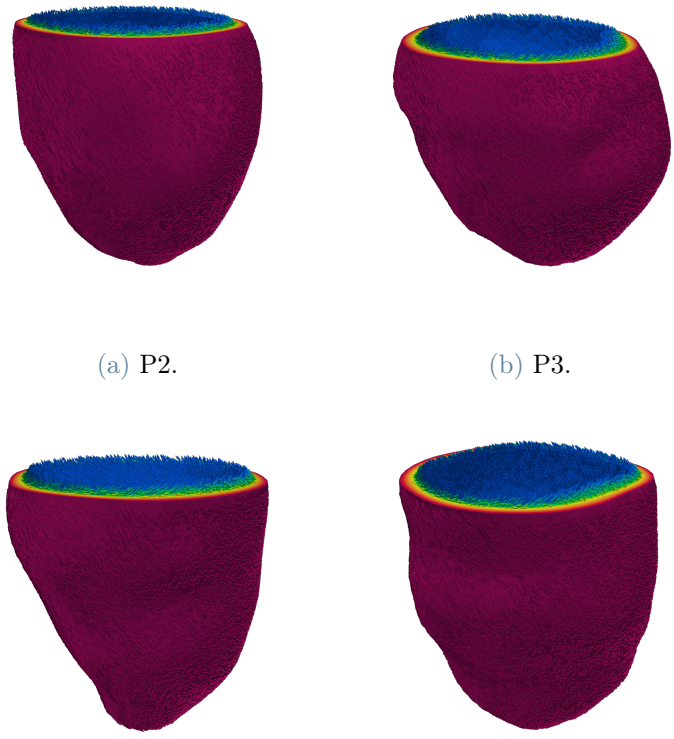

(a) P2. (b) P3.

(c) P8. (d) P11.

Figure 4.4: Reconstructed fibers of P2, P3, P8 and P11.

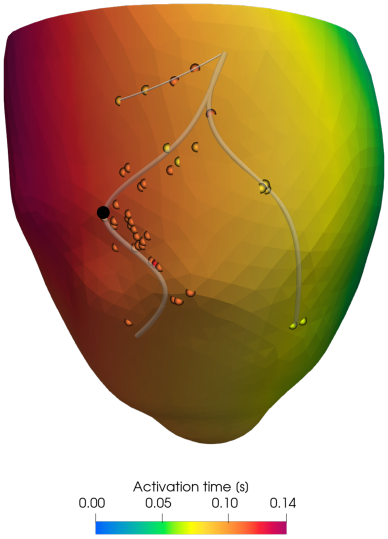

(a) P2.

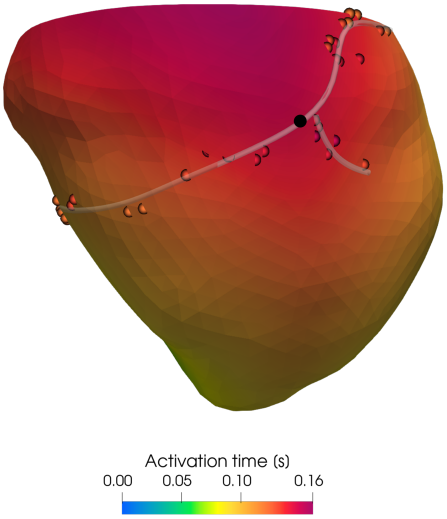

(b) P3.

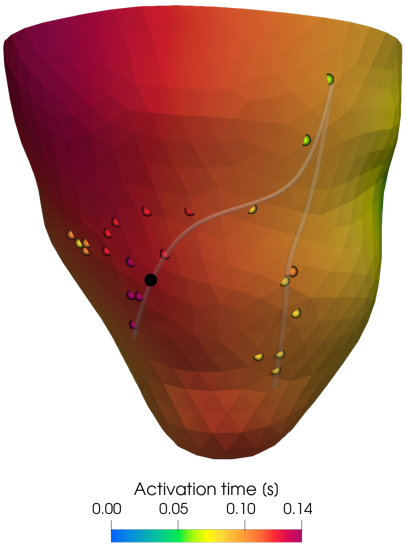

(c) P8.

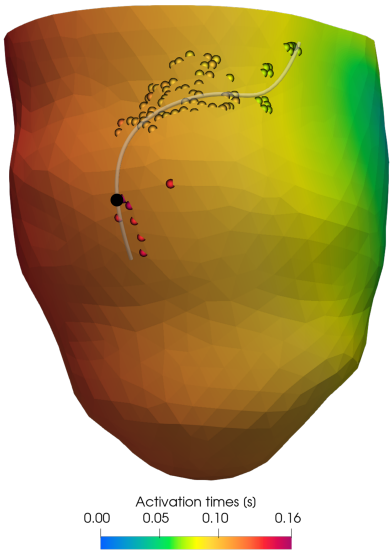

(d) P11.

Figure 4.5: Results of the electrical calibration of P2, P3, P8 and P11. Computed activation times are shown together with measured activation times (colored dots). Reconstructed epicardial veins are colored in grey. Black dots indicate the computed LEAS.

4.2.2. Results of the mechanical calibration

Following the procedure explained in Section 3.3.2, we mechanically calibrate our EM model, in order to fit clinically measured data taken before the CRT implant. We recall that the end diastolic volume (EDV) and the aortic valve opening pressure $\bar{p}^{0D}_{AVO}$ are set

to be equal to their corresponding clinical measure, i.e. EDV_{clin} and $p_{diastolic}$. Therefore, we have only to calibrate the peripheral resistance R and the contractility a_{XB}, to fit the end systolic volume ESV_{clin} and the systolic pressure $p_{systolic}$. In Table 4.2, we report the results of the calibration, while in Table 4.3, we compare the computed and measured data. In Table 4.3 we also show the cardiac frequency of each patient, included in our model exploiting the Tor-ORd ionic model (See Section 3.1.3).

The mitral valve opening pressure $\bar{p}^{0D}_{MVO}$ and the end diastolic pressure $\bar{p}^{0D}_{ED}$ are adjusted for every patient to avoid problems with the convergence of the simulation. In particular, we set $\bar{p}^{0D}_{MVO} = 7\ mmHg$ and $\bar{p}^{0D}_{ED} = 12\ mmHg$ for P3, P8 and P11, while we set $\bar{p}^{0D}_{MVO} = 9\ mmHg$ and $\bar{p}^{0D}_{ED} = 11\ mmHg$ for P2.

	$\boldsymbol{R}$ $[Pa\ s\ m^{-3}]$	$\boldsymbol{a_{XB}}$ $[Pa]$
P2	$3.40{\cdot}10^7$	$2.70{\cdot}10^8$
P3	$3.00{\cdot}10^7$	$3.07{\cdot}10^8$
P8	$5.60{\cdot}10^7$	$1.87{\cdot}10^8$
P11	$3.50{\cdot}10^7$	$2.06{\cdot}10^8$

Table 4.2: Results of the mechanical calibration.

		$\boldsymbol{ESV_{clin}/ESV}$ $[mL]$	$\boldsymbol{EDV_{clin}/EDV}$ $[mL]$	**EF** [%]	$\boldsymbol{P_{diastolic}/\bar{P}_{AVO}}$ $[mmHg]$	$\boldsymbol{P_{systolic}/\bar{P}_{max}}$ $[mmHg]$	**Frequency** [bpm]
P2	*Clinical*	419	501	15.2	60	110	85
	Simulated	419	501	15.1	60	110	85
P3	*Clinical*	238	350	32.0	75	140	75
	Simulated	238	350	31.9	75	140	75
P8	*Clinical*	143	214	33.3	70	130	68
	Simulated	143	214	33.2	70	130	68
P11	*Clinical*	173	231	24.8	80	110	110
	Simulated	173	231	25.0	80	110	110

Table 4.3: Comparison between simulated and clinically measured data. EF: ejection fraction. ESV and EDV are rounded to the nearest integer.

As we can notice from Table 4.3, we are able to simulate the pre-operative condition with a high degree of accuracy. In Figure 4.6, we report the pressure-volume (PV) tracings simulated for each patient in the pre-operative case.

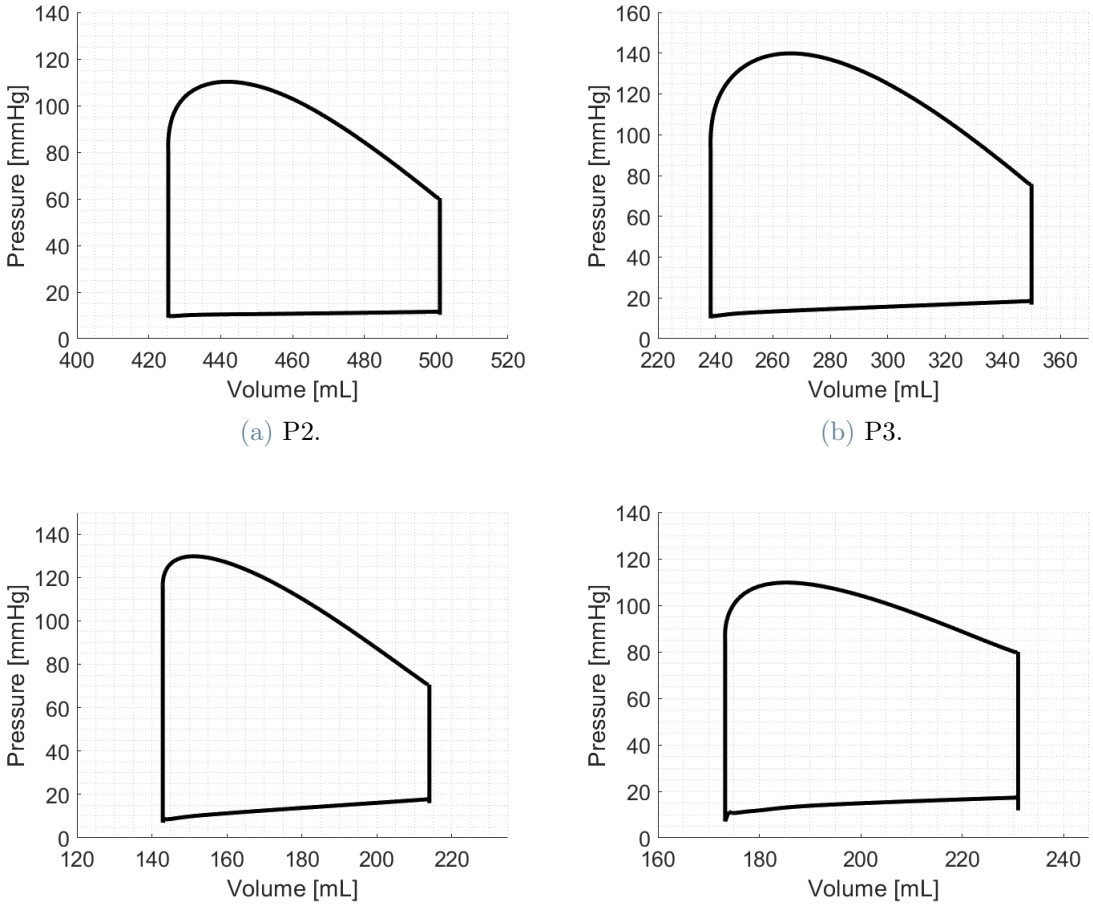

(a) P2.

(b) P3.

(c) P8.

(d) P11.

Figure 4.6: Computed PV loop of P2, P3, P8 and P11, in the pre-operative scenario.

5 | Virtual simulations of cardiac resynchronization therapy

In this chapter, we exploit the pre-operative scenario modeled in Chapter 4 to simulate virtual cardiac resynchronization therapy (CRT) on the patients analysed (called P2, P3, P8 and P11). These patients underwent CRT in Ospedale S. Maria del Carmine in Rovereto.

This chapter is structured as follows:

- In Section 5.1, we will explain the general procedure used to simulate CRT;
- In Section 5.2, we will analyse how different left electrode positions affect CRT virtual simulations;
- In Section 5.3, we will simulate different ventriculoventricular (VV) delays, to understand how they influence CRT outcomes;
- In Section 5.4, we will simulate different right electrode positions, keeping the left electrode fixed at the latest electrically activated segment (LEAS). As far as we know, this is the first study that investigates the effects of the right electrode positioning on CRT;
- Lastly, in Section 5.5, we will summarize all the results obtained simulating virtual CRT.

All the simulations of CRT are performed on `life`$^{\texttt{x}}$, a high performance C++ finite element library, mainly focused on cardiac applications, developed in the MOX department in Politecnico di Milano (`https://lifex.gitlab.io`).

5.1. Simulations of cardiac resynchronization therapy: generalities

In this section we explain the general procedure to simulate virtual CRT.

Simulations of acute post-CRT scenario

Firstly, we have to point out that in our work we only simulate acute post-CRT scenarios, thus excluding the long term effects of the therapy. To simulate the acute phase, we hypothesize that the electrical and mechanical properties of the heart do not change just after the CRT implant. Therefore, the calibration performed for the pre-operative scenario is considered to be still valid for the simulation of CRT. Indeed, CRT induces significant effects on the cardiac muscle only some months after the implant [34], in a process called reverse remodeling. Acutely, a possible change with respect to the pre-operative condition regards the peripheral resistance: in [51], it is suggested that CRT could instantly reduce the arterial load. To better visualize this reduction, we created the illustration in Figure 5.1: as we can see, the slope of the ejection curve in the pressure-volume (PV) tracings decreases with respect to the pre-operative condition. In our simulations, we assume that resistances do not change after CRT implant: this is a valid assumption, since CRT PV loops shown in Figure 5.1 do not differ significantly. This hypothesis was introduced also in other CRT computational studies, such as [11, 33, 68].

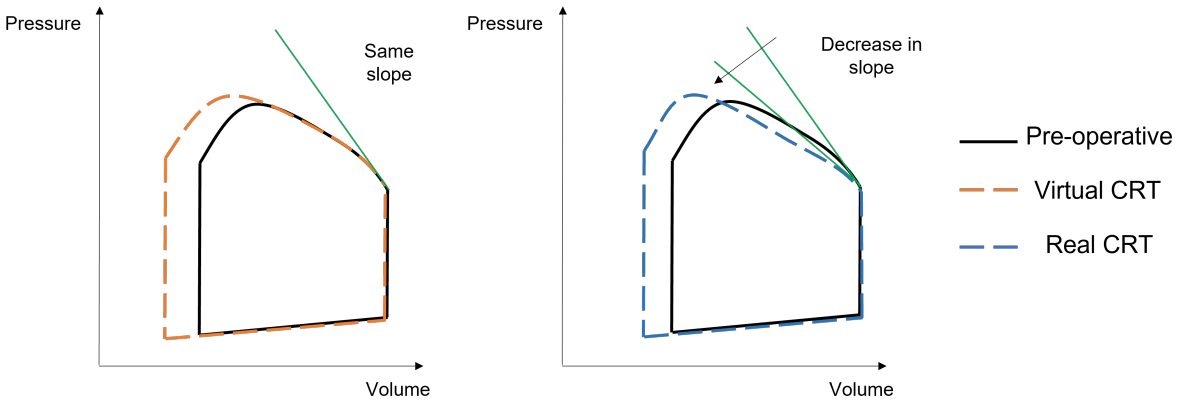

Figure 5.1: Illustration showing a qualitative comparison between simulated and real CRT, just after the implant.

Left and right electrode positions

As pointed out in the previous section, the simulation of CRT is performed with the same calibrated parameters of the pre-operative scenario. The only change we have to introduce regards the stimulations sites: indeed, in CRT the electrical impulse is sent by the right and left electrodes, which are represented in our work by two points selected on the septum and on the epicardium surface, respectively (See Figure 5.2). Specifically, possible left electrode positions are selected to lie on the reconstructed epicardial veins, as done in clinical practice [6, 34, 46]. Figure 4.3 shows the reconstructed veins, along

which possible left electrode positions are chosen. We will also position the left electrode on the computed latest electrically activated segment (LEAS), shown with a black dot in Figure 4.5. The LEAS is indeed the standard left electrode position in clinical practice: in our work, the LEAS position is determined by the simulation, that is able to accurately calculate its location, as proved in [79].

Regarding the right electrode, it should be placed at the apex of the right ventricle, as done in clinics [6, 34]: since we do not include in our model the right ventricle, we place the right electrode on the left ventricle septum, near the apex. To correctly position the right electrode, for P3 and P11 we exploit the right ventricle geometry reconstructed by [68], thanks to which we are able to visualize the right ventricle apex. For P2 and P8, whose right ventricle geometry are not available, we take as reference points the septum data clinically measured (See Figure 4.3, on the right). In this way, we can qualitatively position the right electrode near the apex, as done in clinical practice. Figure 5.3, shows the right electrode location for P2, P3, P8 and P11. These positions will be changed in Section 5.4, to investigate how different right electrode locations can affect CRT outcomes.

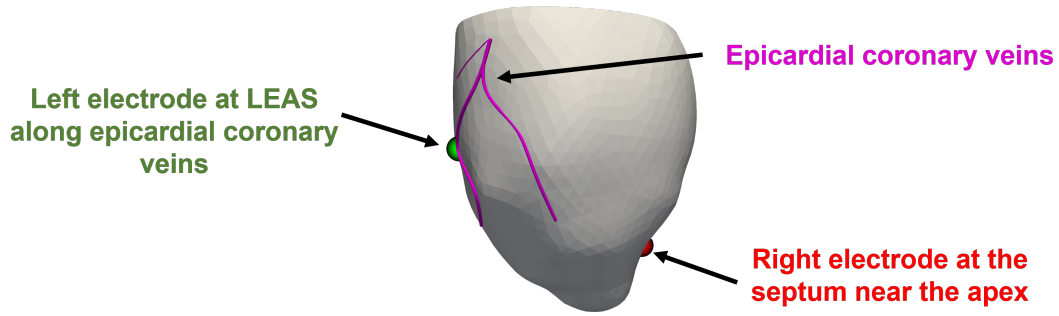

Figure 5.2: Locations of the left (green dot) and right (red dot) electrodes. Epicardial coronary veins are highlighted in fuchsia.

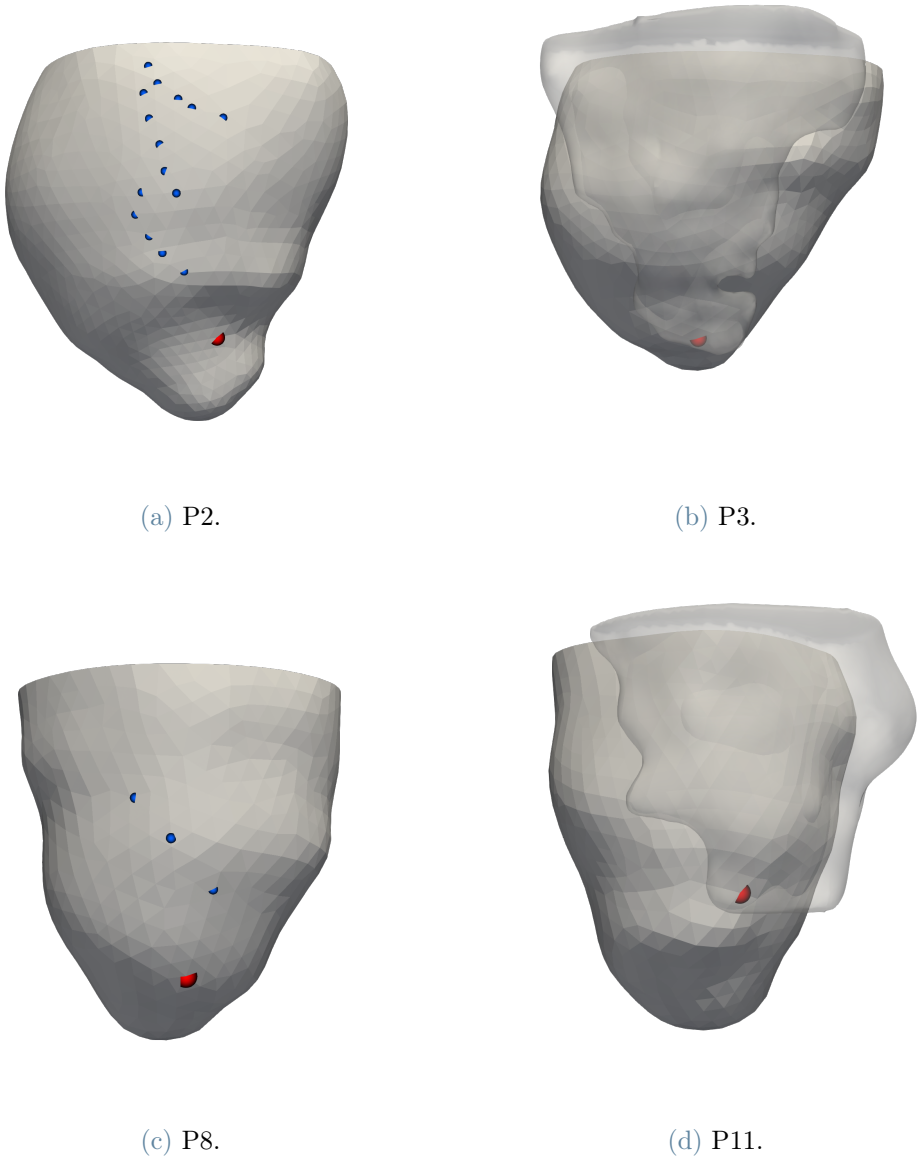

(a) P2. (b) P3.

(c) P8. (d) P11.

Figure 5.3: Standard positions of the right electrode in virtual CRT. The right electrode is highlighted with a red dot. For P2 and P8, the right electrode position is selected with reference to the septum measures (blue dots). For P3 and P11, we exploit the right ventricle reconstruction (reported in transparency) to visualize the position of the right ventricle apex.

Indices to evaluate the therapy outcomes

To evaluate CRT outcomes, we will take in consideration the following indices [34, 51]:

- dP/dt_{max}, the maximum rate of ventricular pressure. As explained in Setion 1.3.2,

it is an index of myocardium contractility, commonly used to asses CRT outcomes;

- The stroke volume SV and the ejection fraction EF, defined as $EF = \frac{SV}{EDV}$ 100, where EDV is the end diastolic volume (See Section 1.1.4);
- The stroke work (SW), defined as the work done by the ventricle to eject the blood. It corresponds to the area within the PV loop tracing (See Figure 5.4).

All the indices previously listed will be calculated for every simulated virtual CRT, to evaluate the therapy outcomes. Moreover, simulated CRTs will be compared with the pre-operative condition, that is taken as reference point. CRT is considered to be effective if it can be noticed an increase with respect to the pre-operative condition in the computed indices values.

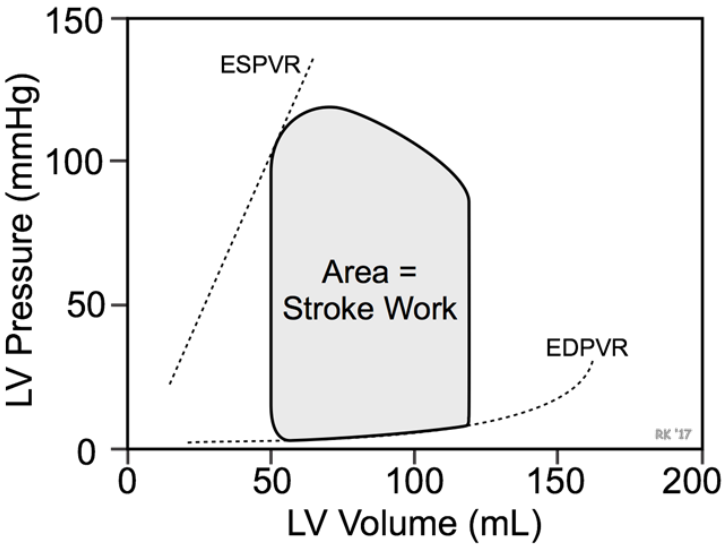

Figure 5.4: Definition of the stroke work. Taken from [12]. LV: left ventricle, ESPVR: end-systolic pressure-volume relationship, EDPVR: end-diastolic pressure-volume relationship.

Left ventricle orientation

In this work, we will show different figures representing the reconstructed epicardial veins together with left electrode stimulation points: we point out that in these cases we are looking at the anterior left ventricle side. This means that the right side of the figure is closer to the left ventricle septal side, while the left one is closer to the left ventricle lateral side (See Figure 5.5).

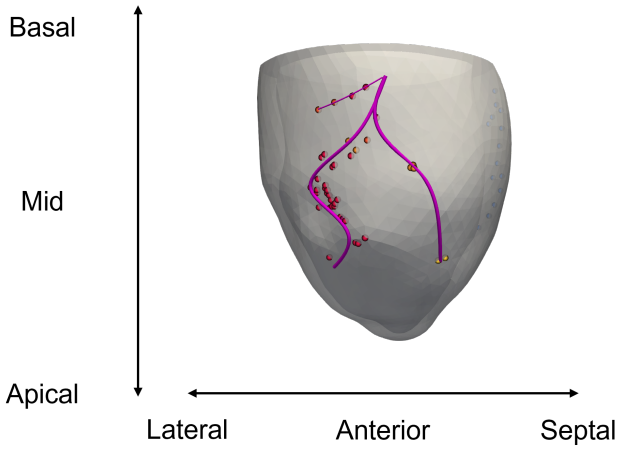

Figure 5.5: Left ventricle orientation.

We will now analyse how the left electrode positioning, the setting of the ventriculoventricular (VV) delay and the right electrode positioning can affect CRT outcomes.

5.2. Study of the left electrode positioning

We want to analyse how different left electrode positions influence CRT. To reach this goal, we place the left electrode on different points along the reconstructed epicardial veins, while we keep the right electrode in its standard position, i.e. at the apex (See Figure 5.3). We also position the left electrode in the latest electrically activated segment (LEAS) along the reconstructed epicardial veins (See Figure 4.5): this is indeed the standard left electrode position in clinical practice. As we have previously mentioned, the LEAS position is determined by the simulation: indeed, in [79], it was established that clinical and computed LEAS positions correspond. In this way, the computed LEAS position can be selected as location of the left electrode.

In these simulations, the VV delay is set to zero: therefore, the right and left stimuli are sent simultaneously. We report in Figure 5.6 the left electrode stimulation points and the corresponding computed PV loop, shown together with the PV loop of the pre-operative scenario. Scarred regions of P8 and P11 are highlighted in black.

In Table 5.1, Table 5.2, Table 5.3 and Table 5.4 we report the computed clinical indices (listed in Section 5.1) for P2, P3, P8 and P11, respectively. All the indices are compared with the pre-operative condition. Maximum and minimum indices values are highlighted in green and red, respectively. Moreover, the left ventricle maximum pressure P_{max} is reported for every simulation performed.

In Table 5.5, we reported for each patient the maximum and minimum relative variation of the calculated indices with respect to the pre-operative scenario.

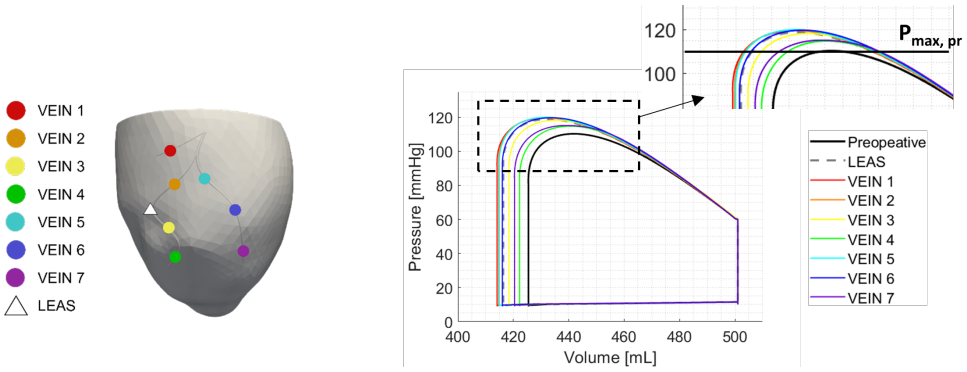

(a) P2.

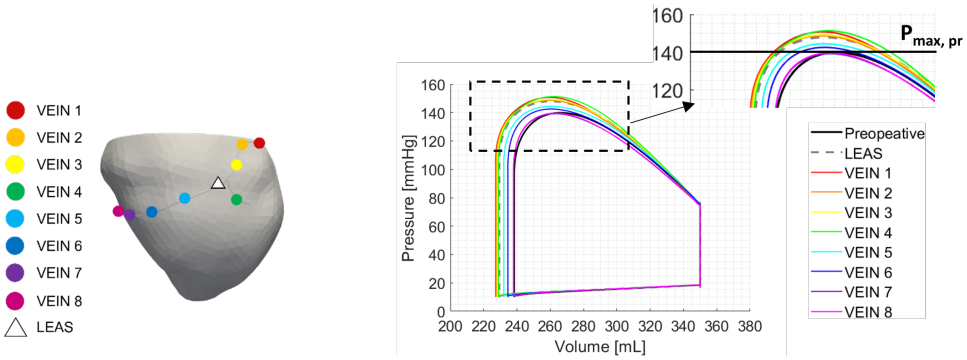

(b) P3.

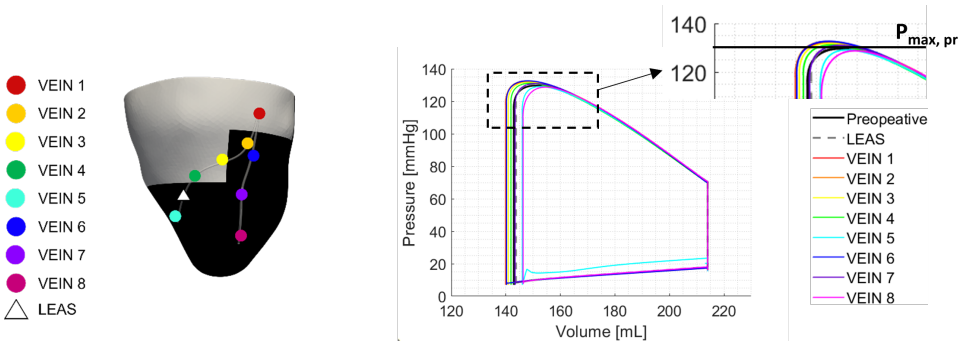

(c) P8.

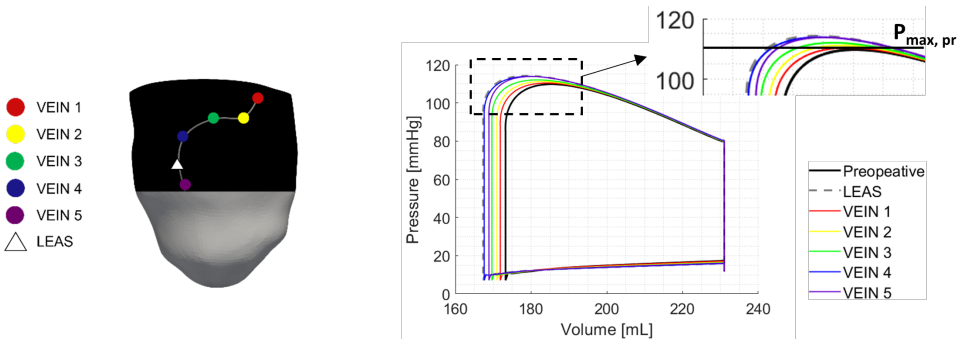

(d) P11.

Figure 5.6: Left electrode stimulation points (left) and corresponding PV loop (right). Scarred regions are highlighted in black. We zoom the upper part of the PV loop to show how the maximum LV pressure increases with respect to the pre-operative scenario ($P_{max,pr}$).

P2									
Scenario	dP/dt_{max} $[mmHg\ s^{-1}]$	$\Delta dP/dt_{max}$ [%]	**SV** $[mL]$	**Δ(SV)** [%]	**EF** [%]	**Δ(EF)** [%]	P_{max} $[mmHg]$	**SW** $[mmHg\ L]$	**Δ(SW)** [%]
Pre-operative	2252	-	76	-	15.1	-	110	6.3	-
LEAS	2418	7.37	85	11.84	16.9	1.8	119	7.5	19.41
VEIN 1	2434	8.08	87	14.47	17.4	2.3	120	7.7	23.46
VEIN 2	2415	7.24	86	13.16	17.2	2.1	120	7.7	22.61
VEIN 3	2464	9.41	83	9.21	16.5	1.4	118	7.3	16.32
VEIN 4	2474	9.86	79	3.95	15.7	0.6	115	6.8	7.71
VEIN 5	2424	7.64	86	13.16	17.2	2.1	120	7.7	22.68
VEIN 6	2523	12.03	85	11.84	17.0	1.9	120	7.6	20.83
VEIN 7	2603	15.59	81	6.58	16.1	1.0	115	7.0	11.36

Table 5.1: Results of CRT simulations for P2. VV Delay is set to zero in every simulation.

P3									
Scenario	dP/dt_{max} $[mmHg\ s^{-1}]$	$\Delta dP/dt_{max}$ [%]	**SV** $[mL]$	**Δ(SV)** [%]	**EF** [%]	**Δ(EF)** [%]	P_{max} $[mmHg]$	**SW** $[mmHg\ L]$	**Δ(SW)** [%]
Pre-operative	3119	-	112	-	31.9	-	140	11.60	-
LEAS	3524	12.98	121	8.04	34.5	2.6	148	13.3	14.84
VEIN 1	3350	7.41	123	9.82	35.1	3.2	151	13.6	17.58
VEIN 2	3422	9.71	123	9.82	35.0	3.1	149	13.5	16.50
VEIN 3	3477	11.48	122	8.93	34.8	2.9	149	13.5	16.63
VEIN 4	3551	13.85	121	8.04	34.6	2.7	151	13.6	17.29
VEIN 5	3422	9.71	118	5.36	33.7	1.8	144	12.7	9.60
VEIN 6	3185	2.12	115	2.68	33.0	1.1	143	12.2	5.49
VEIN 7	2746	-11.96	112	0.00	32.0	0.1	139	11.5	-0.86
VEIN 8	2651	-15.00	112	0.00	32.0	0.1	140	11.5	-0.81

Table 5.2: Results of CRT simulations for P3. VV Delay is set to zero in every simulation.

P8										
Scenario	dP/dt_{max} $[mmHg\ s^{-1}]$	$\Delta dP/dt_{max}$ [%]	**SV** $[mL]$	**Δ(SV)** [%]	**EF** [%]	**Δ(EF)** [%]	P_{max} $[mmHg]$	**SW** $[mmHg\ L]$	**Δ(SW)** [%]	**Fibrosis**
Pre-operative	2731	-	71	-	33.2	-	130	6.7	-	-
LEAS	2527	-7.47	70	-1.41	32.9	-0.3	131	6.6	-1.56	Yes
VEIN 1	2786	2.01	74	4.23	34.6	1.4	132	7.1	6.58	No
VEIN 2	2769	1.39	74	4.23	34.6	1.4	133	7.1	6.26	Yes
VEIN 3	2671	-2.20	73	2.82	34.2	1.0	132	7.0	4.02	No
VEIN 4	2565	-6.08	72	1.41	33.7	0.5	131	6.8	1.77	No
VEIN 5	2510	-8.09	68	-4.23	31.8	-1.4	129	6.0	-10.82	Yes
VEIN 6	2777	1.68	74	4.23	34.5	1.3	133	7.1	5.76	Yes
VEIN 7	2679	-1.90	71	0.00	33.0	-0.2	131	6.7	-0.57	Yes
VEIN 8	2650	-2.97	68	-4.23	31.6	-1.6	129	6.3	-6.36	Yes

Table 5.3: Results of CRT simulations for P8. VV Delay is set to zero in every simulation.

P11										
Scenario	dP/dt_{max} $[mmHg\ s^{-1}]$	$\Delta dP/dt_{max}$ [%]	**SV** $[mL]$	**Δ(SV)** [%]	**EF** [%]	**Δ(EF)** [%]	P_{max} $[mmHg]$	**SW** $[mmHg\ L]$	**Δ(SW)** [%]	**Fibrosis**
Pre-operative	2460	-	58	-	25.0	-	110	4.9	-	-
LEAS	2478	0.73	64	10.34	27.6	2.6	114	5.6	15.63	Yes
VEIN 1	2411	-1.99	59	1.72	25.6	0.6	110	5.1	3.93	Yes
VEIN 2	2419	-1.67	60	3.45	26.0	1.0	111	5.2	6.14	Yes
VEIN 3	2397	-2.56	61	5.17	26.6	1.6	112	5.3	9.45	Yes
VEIN 4	2443	-0.69	63	8.62	27.4	2.4	114	5.6	15.16	Yes
VEIN 5	2496	1.46	62	6.90	26.9	1.9	114	5.5	12.36	Yes

Table 5.4: Results of CRT simulations for P11. VV Delay is set to zero in every simulation.

Patient	**Δ(dP/dt_{max})** [%]	**Δ(SV)** [%]	**Δ(EF)** [%]	**Δ(SW)** [%]
P2	[7.24, 15.59]	[3.95, 14.47]	[0.6, 2.3]	[7.71, 23.46]
P3	[-15.00, 13.85]	[0.00, 9.82]	[0.1, 3.2]	[-0.86, 17.58]
P8	[-8.09, 2.01]	[-4.23, 4.23]	[-1.6, 1.4]	[-10.82, 6.58]
P11	[-2.56, 1.46]	[1.72, 10.34]	[0.6, 2.6]	[3.93, 15.63]

Table 5.5: Maximum and minimum relative variations of dP/dt_{max}, SV, EF and SW with respect to the pre-operative scenario.

General considerations

Firstly, from Table 5.1, Table 5.2, Table 5.3 and Table 5.4 we can observe an increase in the maximum left ventricle pressure P_{max} in all the patients studied. This can be qualitatively noted also in computed PV loop reported in Figure 5.6. This is probably related to a more synchronized contraction of the left ventricle: indeed, the ventricle pumps more blood with respect to the pre-operative condition (computed PV loops are larger), but resistances do not change: therefore, the pressure has to rise-up.

Secondly, as we can notice from Table 5.5, it seems like virtual CRT globally improves all the calculated indices in P2, P3 and P11. P8 does not seem to gain any improvements from virtual CRT: indeed, as we can notice from Figure 5.6c, in some cases (e.g. VEIN 5, VEIN 8) CRT even worsen the pre-operative condition. In P8, fibrotic regions could play a significant role: indeed, in regions detected with fibrosis, conduction velocities are reduced with respect to healthy tissue regions. This results in an asynchronous contraction: healthy tissue contracts earlier with respect to fibrotic one. In this way, CRT could fail to resynchronize the ventricle. Even P11 has fibrotic regions: however, in P11 conductivities are less reduced with respect to P8. Indeed, as we can see from Table 4.1, the degree

of fibrosis z is set to 0.9 in P11 and to 0.7 in P8. This could explain why P11 seems to benefit from CRT.

In Figure 5.7, we report a comparison between cardiac displacements during a heartbeat before and after CRT, in P2, P3, P8 and P11. From Figure 5.7, we can qualitatively notice how CRT affects the ventricle contraction. In the pre-operative scenario, the ventricle contracts in an asynchronous way (see the black arrows): indeed, the ventricle lateral wall moves down, while the septal wall moves up (particularly visible in Figure 5.7a and in Figure 5.7c). With CRT, the ventricle contracts in a more coordinated way, since both the lateral and the septal walls move towards the inside of the ventricle (See Figure 5.7, the second time instant of CRT).

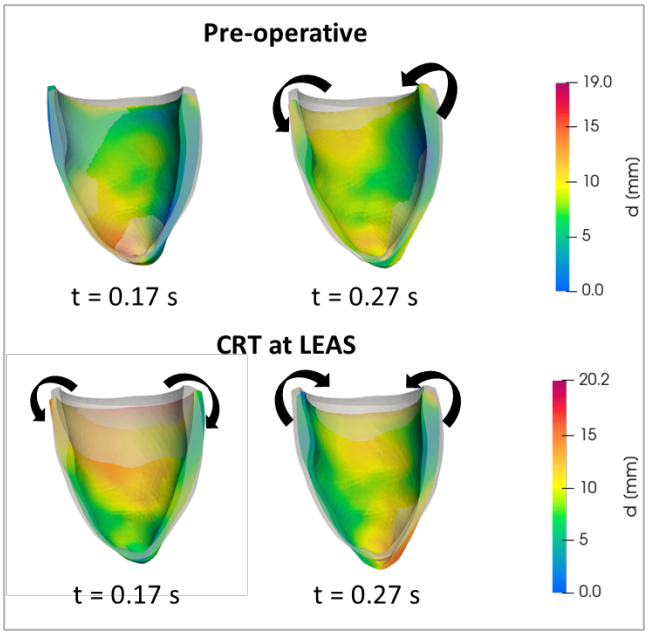

(a) P2.

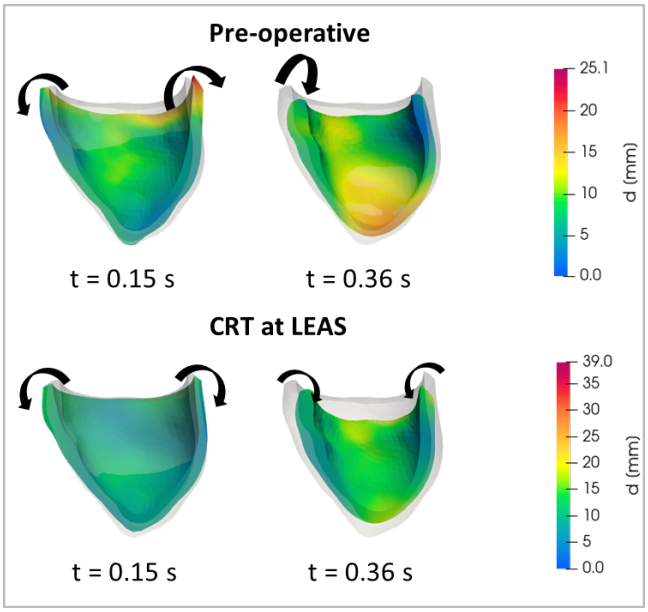

(b) P3.

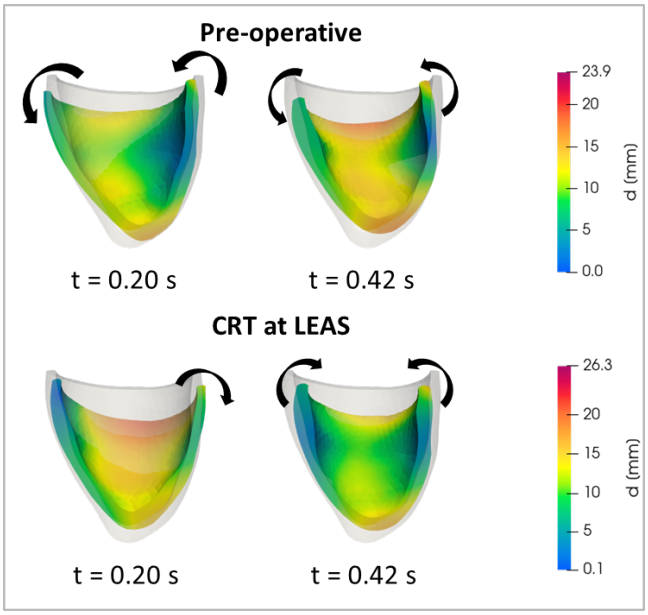

(c) P8.

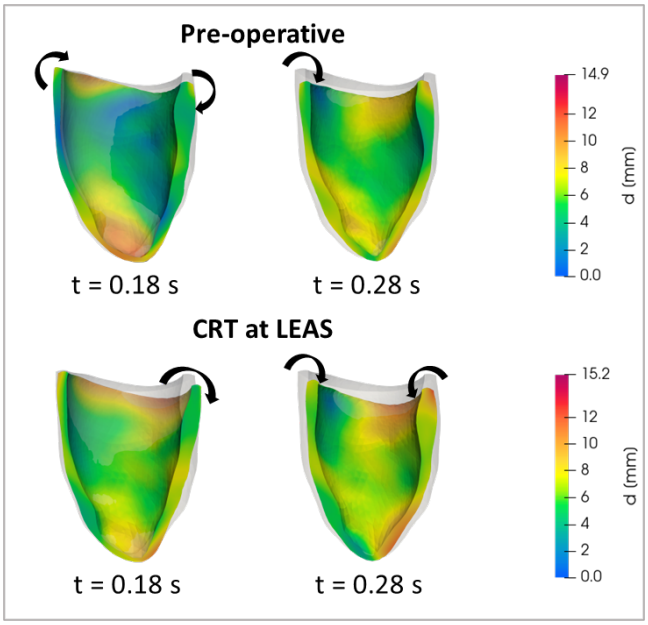

(d) P11.

Figure 5.7: Comparison between displacements d in the pre-operative condition (up) and with CRT at LEAS in P2, P3, P8 and P11 during the cardiac cycle. The left ventricle is shown from the anterior-truncated view. In grey it is highlighted the configuration of the ventricle at the beginning of the cardiac cycle. Black arrows indicate the uncoordinated and coordinated contraction for the pre-operative scenario and for CRT, respectively.

Evaluation of clinical indices

In Table 5.6, we report the left electrode stimulation points corresponding to best and worst values of SV, EF, SW and dP/dt_{max}. For every point we also indicate their position on the ventricle, with reference to Figure 5.5. SV, EF and SW are grouped together: indeed, their highest value is reached in the same point of stimulation (See green values in Table 5.1, Table 5.2, Table 5.3 and Table 5.4). This is reasonable, given their deep correlation: EF is computed from SV, while SW, being the area within the PV loop, is strictly connected to both EF and SV.

	P2	**P3**	**P8**	**P11**
Max	Vein 1	Vein 1	Vein 1	LEAS
SV, EF, SW	(basal lateral)	(basal septal)	(basal septal)	(mid lateral)
Min	Vein 4	Vein 7/Vein 8	Vein 5/Vein 8	Vein 1
SV, EF, SW	(apical lateral)	(mid lateral)	(apical lateral/apical antero-septal)	(basal septal)
Max	Vein 7	Vein 4	Vein 1	Vein 5
$\boldsymbol{dP/dt_{max}}$	(apical septal)	(mid antero-septal)	(basal septal)	(mid lateral)
Min	Vein 2	Vein 7/Vein 8	Vein 5	Vein 3
$\boldsymbol{dP/dt_{max}}$	(mid lateral)	(mid lateral)	(apical lateral)	(basal anterior)

Table 5.6: Points of stimulation that correspond to maximum and minimum values of dP/dt_{max}, SV, EF and SW.

The best values of EF, SV and SW are reached in the basal/mid lateral side of the ventricle in P2 and P11 (See Table 5.6). This result is in accordance with literature: indeed, the best location of the left electrode should be in the lateral or postero-lateral side of the left ventricle [34, 35]. In P8 the best point of stimulation (VEIN 1, see Table 5.6) seems to be near the septal side: this is reasonable, since VEIN 1 does not fall in the ischemic region of P8 (See Figure 5.6c). Indeed, this result confirms that the left electrode should not be placed in ischemic regions, as it is believed in clinical practice [34, 35]. Regarding P3, the best values of EF, SV and SW are reached near the septum: this could seem strange, however, if we look at computed activation times in the pre-operative scenario (See Figure 4.5b), we notice that the left ventricle antero-septal side is the last electrically activated. This could explain why points in this area (like VEIN 1, VEIN 2, VEIN 3 and LEAS, See Figure 4.6b) have comparable and large PV loops.

Regarding dP/dt_{max}, as we can see from Table 5.5, in P8 and P11 there is no significant increase in this index: indeed, in P8 dP/dt_{max} increases of almost 2%, while in P11 it increases of less than 1.5%. Being both P8 and P11 fibrotic, it is possible that the presence of scarred tissue could decrease the rate of ventricular pressure, because of reduced

conduction velocities that lead to an impaired contraction. On the other hand, in P2 and P3 dP/dt_{max} reaches a maximum increase of more than 10% in both patients (See Table 5.5). In particular, in P3 the maximum dP/dt_{max} is reached in the septal side of the ventricle, as for SV, EF and SW (See Table 5.6). There seems to be a correlation between these indices. Moreover, worst values of both dP/dt_{max} and SV, EF and SW are reached in the lateral side of the ventricle. P2 seems to contradict this correlation: indeed, the maximum increase in dP/dt_{max} is reached in the apical septal side, while for SV, EF and SW the maximum corresponds to the basal lateral side. However, differently from P3, in P2 every simulated stimulation point increases the dP/dt_{max} with respect to the pre-operative scenario: indeed, as we can see from Table 5.5, the minimum variation for P2 is +7.24% with respect to the pre-operative scenario, while in P3 dP/dt_{max} is worsen up to 15%. This is true also for SV, EF and SW: in P2 these indices are all improved with respect to the pre-operative scenario. Knowing that all the points improves the clinical indices, and given the fact that it is not possible to select a point that maximizes them all, we would place the left electrode in the LEAS, which induces a good improvement in all the indices (dP/dt_{max} = +7.37% , SV = +11.84%, EF = +1.8%, SW = +19.41%). In this case, we are not able to predict *a priori* a good location for the left electrode, since computed clinical indices indicate different regions to consider.

Latest electrically activated segment

As we can qualitatively notice from Figure 5.6, virtual CRT performed at LEAS improves the pre-operative scenario: indeed, in P2, P3 and P11 all the PV loops are larger. Only in P8 there is no improvement: this is probably related to the position of the LEAS, that is within the ischemic region of P8. As mentioned in the previous sections, the left electrode should not be placed in scarred regions. For P11 we are forced to place the left electrode in the ischemic region (See Figure 5.6d): however, as explained in previous sections, in P11 the degree of fibrosis is less high with respect to P8. Therefore, it is possible that virtual CRT results to be more effective in P11.

In P2 and P3 the LEAS increases also the dP/dt_{max}, with a +7.37% and with a +12.98%, respectively. As mentioned before, in P8 and P11 there is no significant improvement for this index, not even for the LEAS.

In conclusion, stimulating at the LEAS would seem to be a good choice to best optimize CRT. Even though other points of stimulation achieve the maximum indices values, we are not able to give general indications to correctly position the left electrode. Moreover, in clinical practice the left electrode cannot be placed precisely in a certain point: therefore, aiming at the LEAS seems to us the best way to improve the therapy outcomes. The only

exception regards the case in which the LEAS is within a scarred region: in this context, the left electrode should be placed in a healthy region, if accessible.

5.3. Study of the ventriculoventricular delay

We now study the effect of the ventriculoventricular (VV) delay on CRT. We recall that the VV delay is defined as the time interval between the electrical stimuli sent to the right and left electrodes. We perform virtual CRT simulations at LEAS in P2, P3 and P11. For P8, we choose a different point of stimulation (VEIN 1, See Figure 5.6c), since in the previous section we proved that LEAS is not a suitable point for CRT, being within the fibrotic region.

In our work, we define the VV delay as follows:

- Delay $= 0$: the left and right stimuli are simultaneous;
- Delay > 0: the left stimulus is sent after the right one;
- Delay < 0: the left stimulus anticipates the right one.

We simulate delays within the range $[-30, +30]$ ms: these are common values used in clinical practice.

We report in Figure 5.8 the computed PV loops for patient P2, P3, P8 and P11, comparing the different simulated delays. In Table 5.7, Table 5.8, Table 5.9 and Table 5.10 we report the results of the virtual CRT of P2, P3, P8 and P11, respectively.

Discussion of the results

As we can qualitatively notice from Figure 5.8, computed PV loops with a positive or negative delay do not improve CRT outcomes with respect to the case in which right and left stimuli are sent simultaneously. Indeed, also SV, EF and SW do not change significantly with respect to the case in which the VV delay is set to zero (See Table Table 5.7, Table 5.8, Table 5.9 and Table 5.10). In P2 and P11 (See Figure 5.8a and Figure 5.8d), we can even notice a slight decrease in the PV loop width in CRT performed with a positive or negative delay. In P3 and P8 (See Figure 5.8b and Figure 5.8c) PV loops are almost superimposed. This behaviour is probably connected to the fact that imposing a delay between the right and left stimuli can make the ventricle contraction more asynchronous: in this way, the quantity of blood ejected may decrease.

Looking at Table 5.7, Table 5.8 and Table 5.9, we can notice that in P2, P3 and P8 dP/dt_{max} increases if the delay becomes positive. This is more evident in Figure 5.9,

where we plot the relative variation of dP/dt_{max} (with respect to the pre-operative scenario) against the corresponding delay. Among the four patients, P3 displays the greatest increment, with a maximum increase of almost +25%. P11 is the only one with a different trend: indeed, dP/dt_{max} does not gain any improvements from positive or negative delays. We point out that P11 is stimulated from the LEAS, which is within the scarred region (See Figure 5.6d). This could explain why dP/dt_{max} in P11 does not benefit from the delays. In P8 we can notice a small improvement, even if the maximum increase in dP/dt_{max} is less than 5%: also in this case fibrosis probably limits the ventricle contractility.

From Figure 5.9, we can notice that maximum values of dP/dt_{max} correspond to positive delays. This means that the electrical stimulus is first sent to the right electrode and then to the left electrode. This result seems to suggest that activating first the ventricle septal side increases the contractility. Instead, activating first the anterior side results in a decreased dP/dt_{max}.

In conclusion, introducing a delay seems to influence mostly the dP/dt_{max}, while SV, EF and SW do not change significantly. In fibrotic patients (P8 and P11) the delay does not induce an improvement in dP/dt_{max}, while in P2 and P3 a positive delay greatly increases the values of this index. Setting the delay to +15 ms seems to be a good compromise to improve all the calculated indices: indeed, in P2, P3 and P8 dP/dt_{max} is increased, without affecting SV, EF and SW. Only in P11 it would be better to set the delay to 0 ms, probably because the LEAS is within the fibrotic region, as previously explained.

Further investigations should be performed to understand the correlation between the dP/dt_{max} and the delay: a possible way to study this trend could be simulating a wider range of delays, e.g. [-60, +60] ms. In this way, it could be possible to understand how dP/dt_{max} evolves: there may be even a limit in the increase of dP/dt_{max} with respect to the delay.

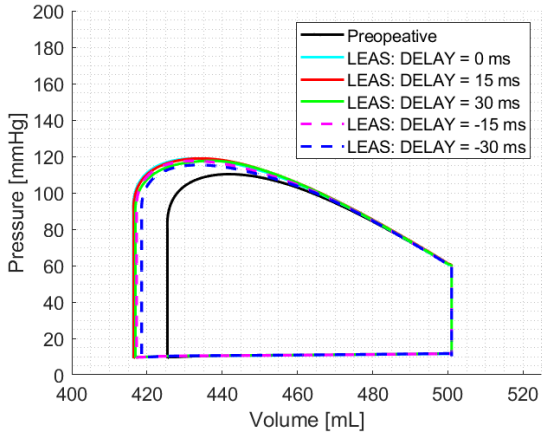

(a) P2.

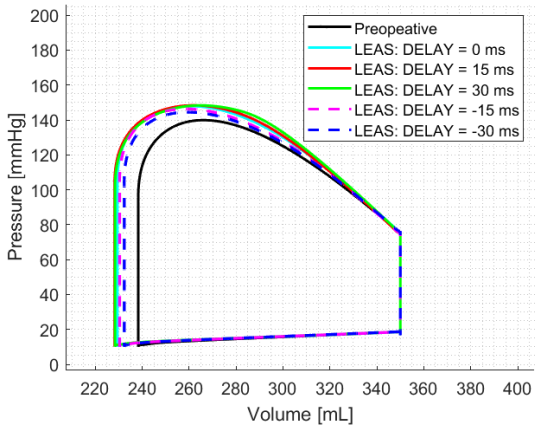

(b) P3.

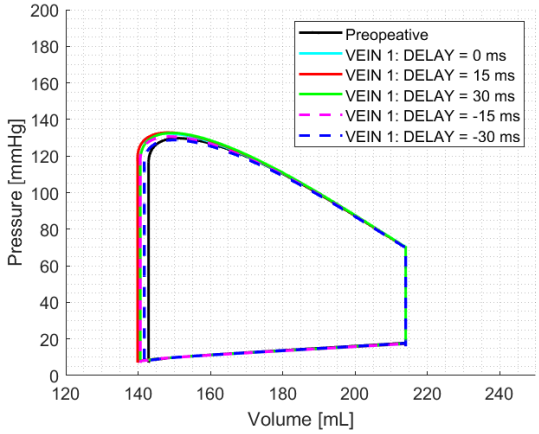

(c) P8.

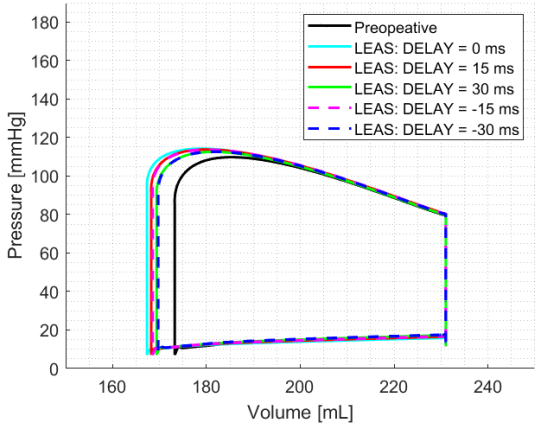

(d) P11.

Figure 5.8: Computed PV loop at different VV delays. Virtual CRT is performed at LEAS in P2, P3 and P11, while it is performed in VEIN 1 in P8.

P2: Virtual CRT at LEAS									
Delay	$\boldsymbol{dP/dt_{max}}$	$\boldsymbol{\Delta dP/dt_{max}}$	**SV**	**Δ(SV)**	**EF**	**Δ(EF)**	$\boldsymbol{P_{max}}$	**SW**	**Δ(SW)**
$[ms]$	$[mmHg\ s^{-1}]$	[%]	$[mL]$	[%]	[%]	[%]	$[mmHg]$	$[mmHg\ L]$	[%]
-30	2350	4.35	82	7.89	16.5	1.4	115	7.1	13
-15	2370	5.24	84	10.53	16.7	1.6	118	7.3	17
0	2418	7.37	85	11.84	16.9	1.8	119	7.5	19
15	2462	9.33	85	11.84	16.9	1.8	119	7.5	20
30	2506	11.28	84	10.53	16.8	1.7	118	7.4	18

Table 5.7: Results of P2 CRT simulations performed at LEAS with different VV delays. We report relative variations of the indices with respect to the pre-operative scenario.

P3: Virtual CRT at LEAS									
Delay	$\boldsymbol{dP/dt_{max}}$	$\boldsymbol{\Delta dP/dt_{max}}$	**SV**	**Δ(SV)**	**EF**	**Δ(EF)**	$\boldsymbol{P_{max}}$	**SW**	**Δ(SW)**
$[ms]$	$[mmHg\ s^{-1}]$	[%]	$[mL]$	[%]	[%]	[%]	$[mmHg]$	$[mmHg\ L]$	[%]
-30	3211	2.95	118	5.36	33.6	1.7	144	12.6	9.00
-15	3337	6.99	120	7.14	34.2	2.3	146	13.0	12.16
0	3524	12.98	121	8.04	34.5	2.6	148	13.3	14.84
15	3671	17.70	122	8.93	34.8	2.9	148	13.5	16.19
30	3896	24.91	122	8.93	34.7	2.8	148	13.5	16.60

Table 5.8: Results of P3 CRT simulations performed at LEAS with different VV delays. We report relative variations of the indices with respect to the pre-operative scenario.

P8: Virtual CRT at VEIN 1									
Delay	$\boldsymbol{dP/dt_{max}}$	$\boldsymbol{\Delta dP/dt_{max}}$	**SV**	**Δ(SV)**	**EF**	**Δ(EF)**	$\boldsymbol{P_{max}}$	**SW**	**Δ(SW)**
$[ms]$	$[mmHg\ s^{-1}]$	[%]	$[mL]$	[%]	[%]	[%]	$[mmHg]$	$[mmHg\ L]$	[%]
-30	2647	-3.08	72	1.41	33.8	0.6	129	6.8	1.34
-15	2706	-0.92	73	2.82	34.3	1.1	131	7.2	6.87
0	2786	2.01	74	4.23	34.6	1.4	132	7.1	6.58
15	2813	3.00	74	4.23	34.7	1.5	133	7.2	6.87
30	2817	3.15	73	2.82	34.3	1.1	133	7.1	5.44

Table 5.9: Results of P8 CRT simulations performed at VEIN 1 with different VV delays. We report relative variations of the indices with respect to the pre-operative scenario.

P11: Virtual CRT at LEAS									
Delay	$\boldsymbol{dP/dt_{max}}$	$\boldsymbol{\Delta dP/dt_{max}}$	**SV**	**Δ(SV)**	**EF**	**Δ(EF)**	$\boldsymbol{P_{max}}$	**SW**	**Δ(SW)**
$[ms]$	$[mmHg\ s^{-1}]$	[%]	$[mL]$	[%]	[%]	[%]	$[mmHg]$	$[mmHg\ L]$	[%]
-30	2458	-0.08	61	5.17	26.5	1.5	113	5.3	8.60
-15	2471	0.45	62	6.90	27.1	2.1	114	5.5	12.41
0	2478	0.73	64	10.34	27.6	2.6	114	5.6	15.63
15	2437	-0.93	63	8.62	27.2	2.2	114	5.5	13.17
30	2417	-1.75	62	6.90	26.7	1.7	113	5.3	9.05

Table 5.10: Results of P11 CRT simulations performed at LEAS with different VV delays. We report relative variations of the indices with respect to the pre-operative scenario.

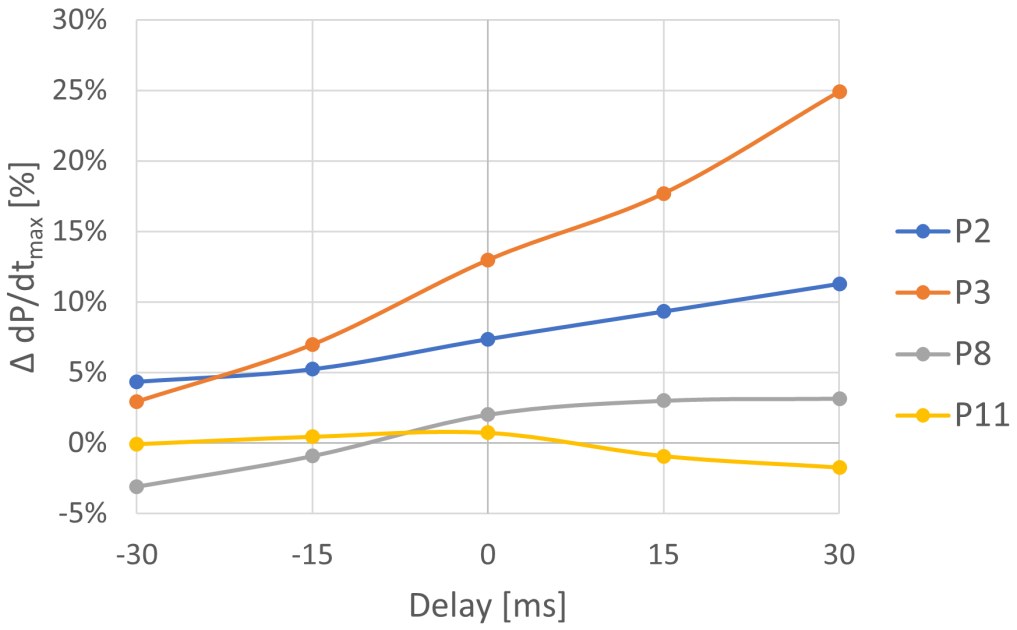

Figure 5.9: Relative variation of dP/dt_{max} with respect to the pre-operative condition at different VV delays, for P2, P3, P8 and P11.

5.4. Study of the right electrode positioning

We now analyse how the right electrode position can affect CRT outcomes. In this work, the right electrode is placed in different points along the ventricle septum (See Figure 5.10), while the left one is placed at the LEAS in every patient. In this way, we can compare virtual CRT performed at different right electrode configurations with the standard CRT (i.e. left electrode at the LEAS, right electrode at the apex). The VV delay is set to zero in every simulation.

As far as we know, this is the first work that investigates the effect of the right electrode position on CRT: indeed, CRT studies are mostly focused on the left electrode location, neglecting the effect of the right electrode position. Therefore, there is a great interest in understanding how it can affect CRT outcomes: actually, this possibility has never been explored neither in clinics nor in a computational study. We recall that the right electrode could be moved from its standard position (i.e. the right ventricle apex): indeed, as explained in [83], the right electrode can be placed along the septum.

We report in Figure 5.11 computed PV loops for each right electrode position simulated. PV loops are compared with the pre-operative scenario (red dotted line) and with the standard CRT scenario (black line), i.e. the case in which virtual CRT is performed with

the right electrode in the apex. We report in Table 5.11, Table 5.12, Table 5.13 and Table 5.14 the indices computed for each simulated scenario for P2, P3, P8 and P11, respectively. All the indices are compared with respect to the pre-operative scenario.

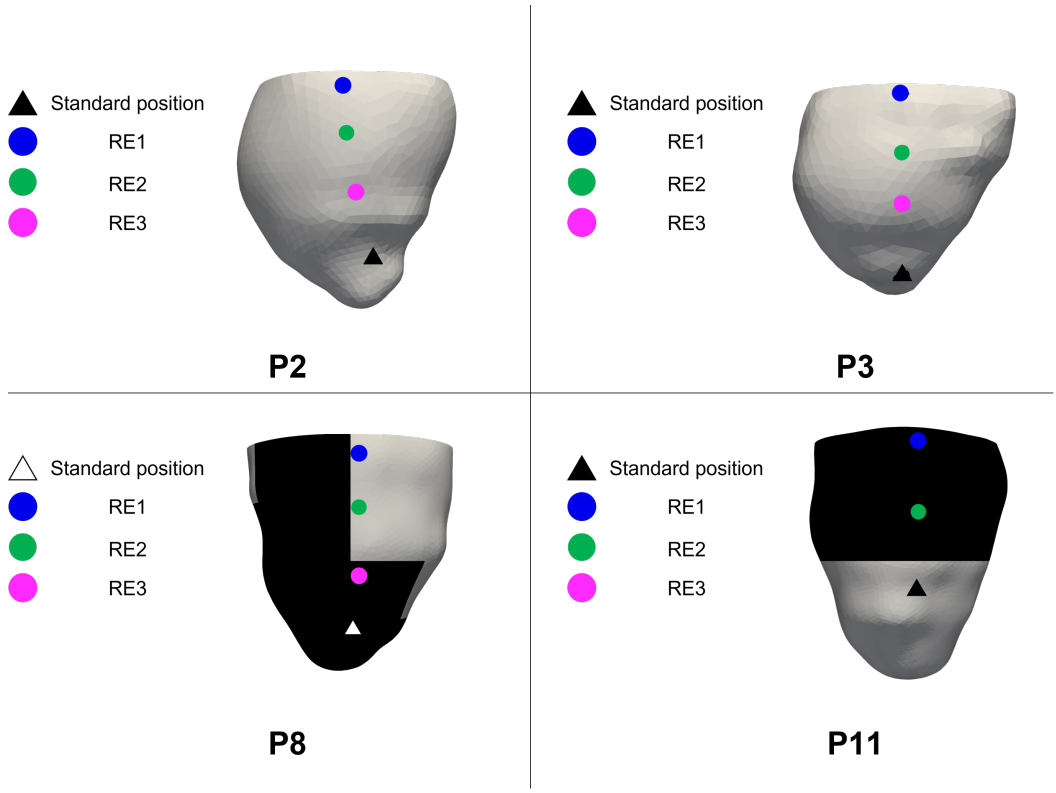

Figure 5.10: Right electrode stimulation points of P2, P3, P8 and P11. The standard position of the right electrode is represented with a triangle. Scarred regions in P8 and P11 are colored in black.

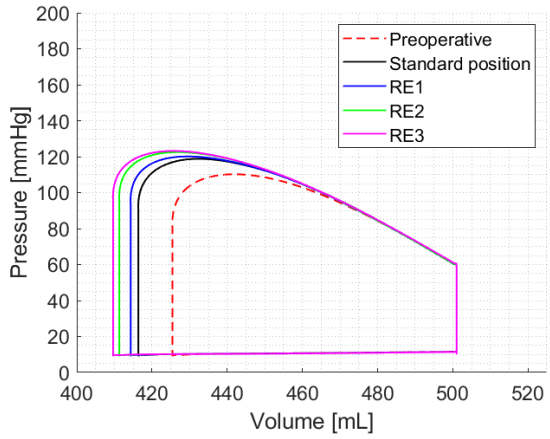

(a) P2.

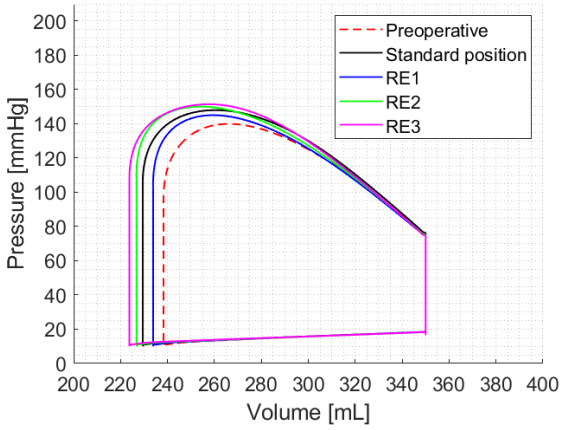

(b) P3.

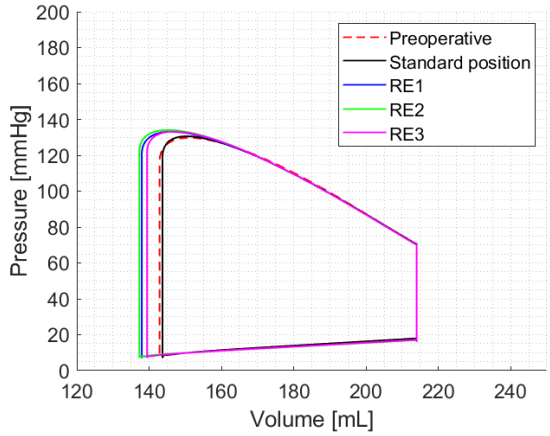

(c) P8.

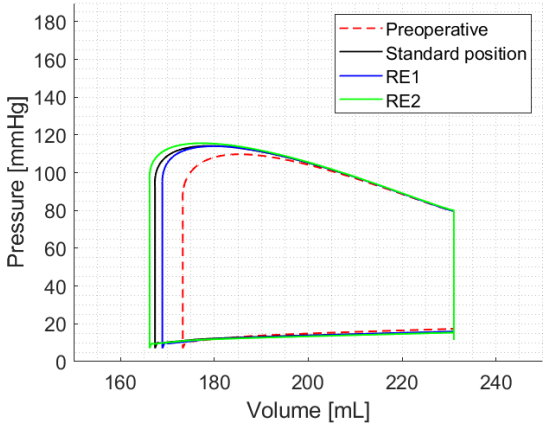

(d) P11.

Figure 5.11: Computed PV loop at different right electrode positions. The left electrode is set at the LEAS in all the patients. The standard CRT configuration (i.e. the right electrode positioned at the apex) is colored in black, while the pre-operative condition is colored with a red dotted line.

P2									
Scenario	$\boldsymbol{dP/dt_{max}}$ $[mmHg\ s^{-1}]$	$\boldsymbol{\Delta dP/dt_{max}}$ [%]	**SV** $[mL]$	**Δ(SV)** [%]	**EF** [%]	**Δ(EF)** [%]	$\boldsymbol{P_{max}}$ $[mmHg]$	**SW** $[mmHg\ L]$	**Δ(SW)** [%]
Pre-operative	2252	-	76	-	15.1	-	110	6.3	-
Standard	2418	7.37%	85	11.84%	16.9	1.8	119	7.5	19.41%
RE 1	2233	-0.84%	87	14.47%	17.3	2.2	120	7.7	23.49%
RE 2	2242	-0.44%	90	18.42%	17.9	2.8	123	8.2	30.06%
RE 3	2330	3.46%	91	19.74%	18.2	3.1	123	8.4	33.44%

Table 5.11: Results of P2 CRT simulations with different right electrode location. VV Delay is set to zero in every simulation. All the results are compared with the pre-operative condition. The standard scenario corresponds to the case in which the right electrode is placed at the apex.

P3									
Scenario	$\boldsymbol{dP/dt_{max}}$ $[mmHg\ s^{-1}]$	$\boldsymbol{\Delta dP/dt_{max}}$ [%]	**SV** $[mL]$	**Δ(SV)** [%]	**EF** [%]	**Δ(EF)** [%]	$\boldsymbol{P_{max}}$ $[mmHg]$	**SW** $[mmHg\ L]$	**Δ(SW)** [%]
Pre-operative	3119	-	112	-	31.9	-	140	11.6	-
Standard	3524	12.98%	121	8.04%	34.5	2.6	148	13.3	14.84%
RE 1	3103	-0.51%	116	3.57%	33.2	1.3	145	12.4	6.96%
RE 2	3461	10.97%	123	9.82%	35.2	3.3	150	13.7	17.85%
RE 3	3570	14.46%	126	12.50%	36.1	4.2	151	14.2	22.30%

Table 5.12: Results of P3 CRT simulations with different right electrode location. VV Delay is set to zero in every simulation. All the results are compared with the pre-operative condition. The standard scenario corresponds to the case in which the right electrode is placed at the apex.

P8										
Scenario	$\boldsymbol{dP/dt_{max}}$ $[mmHg\ s^{-1}]$	$\boldsymbol{\Delta dP/dt_{max}}$ [%]	**SV** $[mL]$	**Δ(SV)** [%]	**EF** [%]	**Δ(EF)** [%]	$\boldsymbol{P_{max}}$ $[mmHg]$	**SW** $[mmHg\ L]$	**Δ(SW)** [%]	**Fibrosis**
Pre-operative	2731	-	71	-	33.2	-	130	6.7	-	-
Standard	2527	-7.47%	70	-1.41%	32.9	-0.3	131	6.6	-1.56%	Yes
RE 1	2575	-5.71%	76	7.04%	35.5	2.3	133	7.4	9.74%	No
RE 2	2592	-5.09%	77	8.45%	35.8	2.6	134	7.5	11.34%	No
RE 3	2547	-6.74%	75	5.63%	34.8	1.6	133	7.2	7.19%	Yes

Table 5.13: Results of P8 CRT simulations with different right electrode location. VV Delay is set to zero in every simulation. All the results are compared with the pre-operative condition. The standard scenario corresponds to the case in which the right electrode is placed at the apex.

P11										
Scenario	dP/dt_{max} $[mmHg\ s^{-1}]$	$\Delta dP/dt_{max}$ [%]	**SV** $[mL]$	**Δ(SV)** [%]	**EF** [%]	**Δ(EF)** [%]	P_{max} $[mmHg]$	**SW** $[mmHg\ L]$	**Δ(SW)** [%]	**Fibrosis**
Pre-operative	2460	-	58	-	25	-	110	4.9	-	-
Standard	2478	0.73%	64	10.34%	27.6	2.6	114	5.6	15.6%	No
RE 1	2534	3.01%	62	6.90%	26.9	1.9	114	5.5	12.6%	Yes
RE 2	2523	2.56%	65	12.07%	28.1	3.1	116	5.8	19.6%	Yes

Table 5.14: Results of P11 CRT simulations with different right electrode location. VV Delay is set to zero in every simulation. All the results are compared with the pre-operative condition. The standard scenario corresponds to the case in which the right electrode is placed at the apex.

Discussion of the results

From Figure 5.11, we can qualitatively observe that changing the right electrode location seems to increase PV loops width in all the patients. Indeed, as we can see in Table 5.15, SV, EF and SW are greatly increased with respect to the pre-operative scenario. If we look at SV, EF and SW, the best points of stimulation seem to be (See Table 5.11, Table 5.12, Table 5.13 and Table 5.14):

- RE 3 in P2;
- RE 3 in P3;
- RE 2 in P8;
- RE 2 in P11.

Moreover, these points show the highest SV, EF and SW values ever reached in this work: indeed, maximum values in Table 5.15 are always greater than the ones shown in Table 5.5. The location of the right electrode seems to be the most impacting factor on SV, EF and SW. To investigate this result, we report in Figure 5.12 computed activation times in the standard scenario (i.e. with the right electrode in the apex) and in the best scenario (obtained by locating the right electrode in positions listed before). We show the positions of the LEAS and of the right electrode with a pink dot. As we can notice from Figure 5.12, it seems that best electrode positions lead to a more symmetric electrical activation. This can be observed for all the patients. This behaviour can be explained by looking at the relative positions of the right and left electrode: indeed, in the best scenarios the LEAS and the right electrode are more horizontally aligned with respect to the standard case. Probably, having the two electrodes aligned allows to have a symmetric electrical activation, that results in a more synchronized contraction. In this

way, the ventricle is able to pump more blood.

The dP/dt_{max} index does not seem to benefit from a different right electrode location with respect to the standard case. Indeed, in P8 and P11 this index does not increase, being in the case of P8 even worse with respect to the pre-operative scenario (See Table 5.13 and Table 5.14)). In P2, only positions RE 1 and RE 2 worsen the dP/dt_{max} (See Table 5.11): these points are located in the basal/mid septal side of the ventricle (See Figure 5.10). In P3, the only point that worsen the dP/dt_{max} is RE 1 (See Table 5.12), that is located in the basal septal side of the ventricle (See Figure 5.10). P2 and P3 results seem to suggest that mid/basal locations of the right electrode could decrease the dP/dt_{max}, and therefore the contractility.

In conclusion, varying the right electrode seems to greatly impact SV, EF and SW, because of a more synchronized contraction. On the other hand, the dP/dt_{max} does not benefit from a different right electrode location: in this context, we hypothesize that it would be better to give more importance to the SV, EF and SW, since an increase in their values is correlated to a more synchronized contraction.

Patient	**$\Delta(dP/dt_{max})$** [%]	**Δ(SV)** [%]	**Δ(EF)** [%]	**Δ(SW)** [%]
P2	[-0.84, 7.37]	[11.84, 19.74]	[1.8, 3.1]	[19.41, 33.44]
P3	[-0.51, 14.46]	[3.57, 12.50]	[1.3, 4.2]	[6.96, 22.30]
P8	[-7.47, -5.09]	[-1.41, 8.45]	[-0.3, 2.6]	[-1.56, 11.34]
P11	[0.73, 3.01]	[6.90, 12.07]	[1.9, 3.1]	[12.6, 19.6]

Table 5.15: Maximum and minimum relative variations of dP/dt_{max}, SV, EF and SW with respect to the pre-operative scenario varying the right electrode position.

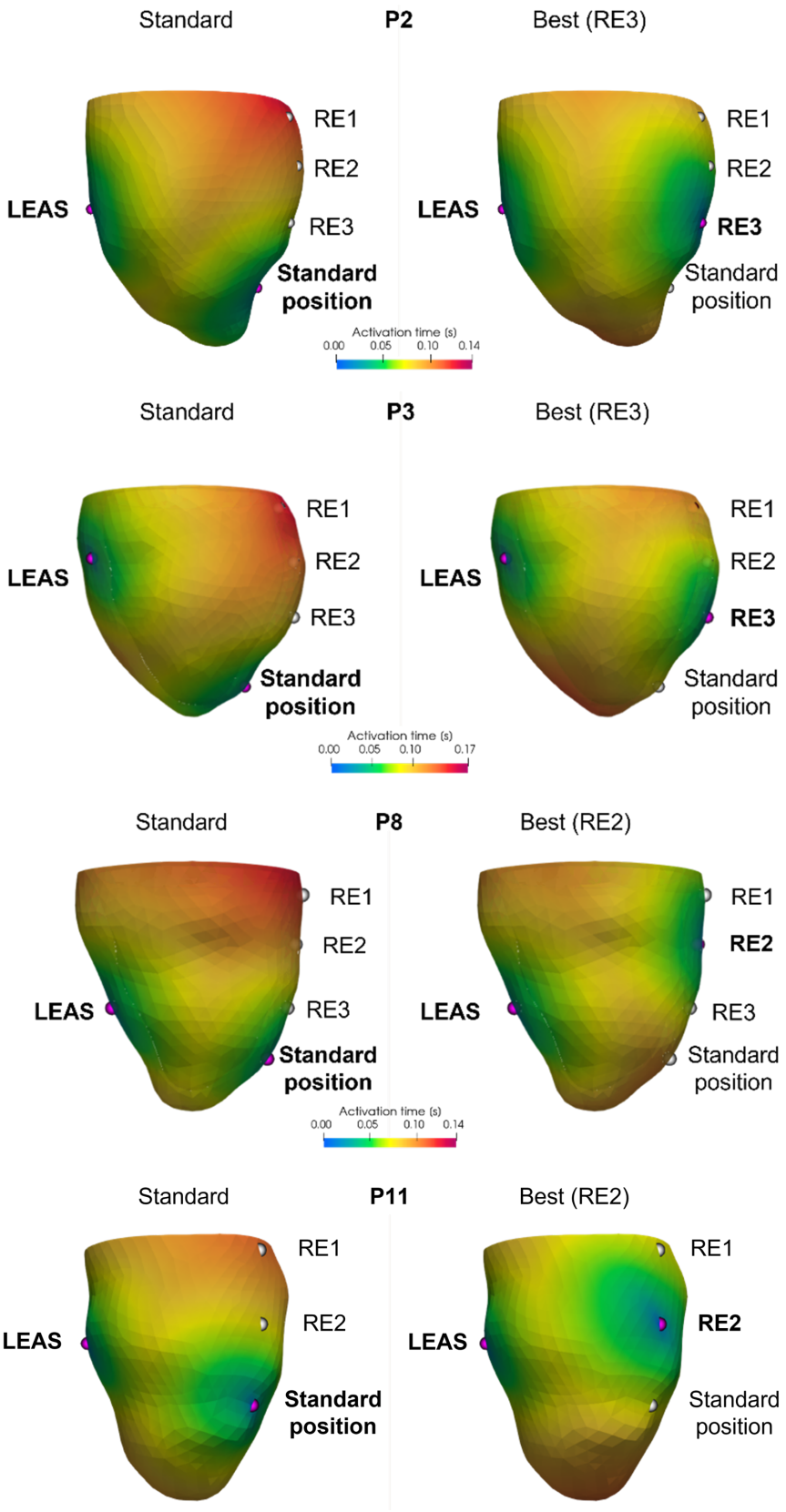

Figure 5.12: Activation times computed with the standard (left) and best (right) right electrode position. Stimulation points are colored in fuchsia. Grey points represent the other simulated right electrode positions.

5.5. Summary of the results

We now summarize all the results discussed in Section 5.2, Section 5.3 and in Section 5.4.

In Section 5.2, we firstly note that virtual CRTs induce an increase in the maximum left ventricle pressure. This result is obtained in every simulation performed. This increase in pressure is probably connected with the ejected amount of blood: indeed, CRT induces a more synchronized contraction, that results in a greater SV. Since resistances do not change with respect to the pre-operative scenario, ventricular pressure has to rise, so that a greater quantity of blood can be pushed out.

We perform different virtual CRT simulations, taking into account the effects related to different positions of left and right electrode and to different VV delays. In all the three configurations studied, we notice that all the patients analysed seem to show a positive response to simulated CRT. The only exception is P8: no significant improvements are obtained by varying the left electrode position or by setting a VV delay. For P8, the only way to improve CRT outcomes is changing the position of the right electrode: indeed, as we can see in Table 5.15, we have a maximum increase in SV of +8.45% and in SW of +11.34%.

Regarding the left electrode positions, in P2 and P11 we obtain the best values of SV, EF and SW in the lateral side of the ventricle (See Section 5.2). On the other hand, in P3 best values are reached near the septum: however, in this case this region corresponds to the latest electrically activated area, thus explaining why best SV, EF and SW values are achieved in this zone. In P8, the best point point of stimulation is near the septal side and outside the scarred region, even if we have to point out that no significant improvements are recorded. These considerations hold true only for SV, EF and SW: indeed, the index dP/dt_{max} shows different results. In P2 there seems to be no correlation between dP/dt_{max} and SV, EF and SW: indeed their maximum values are reached at the apical septal side and at the basal lateral side, respectively, two very distant regions. In P8 and P11, no significant increase in dP/dt_{max} is computed. P3 is the only patient that shows a correlation between the two groups of indices: indeed, their best values are achieved in the basal septal side.

We also study the LEAS effect on CRT: apart from P8, all the patients show good indices values at this stimulation point. Even though the LEAS does not maximize the computed indices, we still consider this point as the one we should choose to optimize CRT. Indeed, we are not able to give precise indications regarding the position of the left electrode: therefore, the LEAS results to be the point to target for the left electrode.

The second configuration studied regards the setting of the VV delay. We simulate different delays, considering the delay positive if the left stimulus is sent after the right one, while we consider it negative if the left stimulus anticipates the right one. Regarding the SV, EF and SW, no improvements are recorded: in some cases their values are even worsen. dP/dt_{max} seems to be highly dependent on the delay: indeed, higher delays correspond to higher dP/dt_{max}. In this work, we propose to set the delay to +15 ms: this seems to us the best compromise to obtain improved values of both dP/dt_{max} and of SV, EF and SW. Only in P11 the delay should be set to zero: however, we recall that in this case the LEAS is within the scarred regions, that probably reduces the rate of ventricular pressure dP/dt_{max}. In this work, we were able to identify a possible VV delay setting to optimize CRT: we want to recall that VV delay optimization is rarely performed in clinics. To correctly set the VV delay, an alternative to computational study is represented by device-based algorithm, able to automatically set the VV delay. However, these algorithms still need to be validated, since, as explained in [62], they are not able to correctly optimize the device.

Lastly, we study the impact of the right electrode positioning on simulated CRT. The most significant result regards the improvement of SV, EF and SW: indeed, it seems that positioning the right electrode at the same height of the left electrode results in a significant increase in SV, EF and SW. This is probably related to a more symmetric electrical activation, that leads to a more synchronized contraction.

To summarize, in this work we propose to place the left electrode at the LEAS, since our simulations proved that virtual CRTs performed in this point improve the therapy outcomes. If LEAS is within a scarred region, another point in the healthy tissue should be taken in consideration. Secondly, if the left electrode does not fall within a scarred region, we suggest to set the VV delay to +15 ms, since in this way all the considered indices are improved. Lastly, we propose to take in consideration to move the right electrode along the septum: in particular, it seems that placing the right and left electrode at the same height results in a more synchronized contraction. This alignment between the two electrodes can be realistically performed in clinical practice by exploiting the electroanatomic mapping procedure (See Section 2.4), that allows to accurately visualize the electrodes position.

The evaluation of clinical indices is crucial to understand if CRT is effective: however, as we have previously explained, indices considered in this work lead to contrasting results. In particular, we notice that:

- dP/dt_{max} seems highly sensitive to the presence of fibrotic regions. Indeed, in P8

and P11 this index has never significantly improved. Moreover, dP/dt_{max} is highly influenced by the VV delay, reaching higher values with more positive delays;

- SV, EF and SW are mostly influenced by the position of the right electrode.

It is still not clear which indices should be taken in consideration to evaluate CRT; moreover, we are only simulating the CRT post-implant scenario, thus excluding all the long terms effect of the therapy. Further investigations should be performed to understand how short and long term effects are correlated.

6 | Conclusions and future developments

Cardiac resynchronization therapy (CRT) is an effective treatment for heart failure, mostly indicated in patients suffering from left bundle branch block (LBBB). Even though beneficial effects of CRT are widely recognized, 30% of patients selected for CRT do not show any improvements from the therapy. In this context, in this thesis we wanted to investigate how different CRT configurations could improve the therapy outcomes, exploiting a calibrated electro-mechanics (EM) model of the left ventricle. We analysed four patients who underwent CRT in Ospedale S. Maria del Carmine in Rovereto; in two of them fibrotic regions were detected.

To perform virtual CRT simulations, we first needed to model the pre-operative scenario. Indeed, for each patient we calibrated our electrical and mechanical model in order to reproduce clinical data we had at our disposal, including also patient cardiac frequency. Regarding the mechanical calibration procedure, to speed-up the process we exploited a cardiac 0D emulator, a surrogate cardiac model built from pressure-volume tracings of the EM simulations. The emulator allowed to significantly simplify the calibration procedure, reducing the computational cost needed.

Once modeled the pre-operative scenario, we simulated virtual CRT in every patient, while considering still valid the calibration performed for the pre-operative scenario, under the assumption that the myocardial contractility and vascular properties are not affected in the acute phase. We studied different CRT configurations, in particular:

- We changed the left electrode locations, selecting positions along the epicardial veins;
- We introduced a delay between the right and left stimuli;
- We modified the standard position of right electrode, considering locations on the septal side of the ventricle.

We analysed all the configurations with four clinical indices: the stroke volume (SV),

the ejection fraction (EF), the stroke work (SW) and the maximum rate of ventricular pressure dP/dt_{max}. These indices are crucial to evaluate CRT outcomes: however, our analysis showed that they may lead to contrasting results. Indeed, dP/dt_{max} was highly influenced by the the delay between the right and left stimuli: maximum increase in this index were achieved when the stimulus is sent first to the right electrode. For SV, EF and SW the most impacting factor seemed to be the right electrode position: if the right electrode is at the same height of the left one, the contraction is more synchronized, increasing the volume of blood ejected. Regarding the left electrode position, we noticed that placing the electrode in a scarred regions resulted in a worsening of all the indices. Moreover, the latest electrically activated segment (LEAS) seemed to be a good location for the left electrode: indeed all the indices were improved in all patients except one.

Our work has obviously some limitations:

- We analysed a small number of patients (four), thus we cannot extend our results to a more general clinical scenario;
- To model virtual CRT, we used calibrated parameters of the pre-operative scenario. This poses a limitation on our work: indeed, just after CRT is implanted parameters such peripheral resistances change. To overcome this limit, we would need to integrate in our model clinical data measured just after CRT is activated;
- We did not include in our model the right ventricle, that should be implemented in order to realistically simulate the position of the right electrode;
- Our EM model did not include the Purkinje fibers: these should be considered to proper model cardiac electrical activation;
- Further investigations are needed to understand which clinical indices should be taken in consideration to evaluate the post-acute scenario. Moreover, we would need to understand which is the correlation between short and long term effect induced by the therapy.

Possible future developments in the context of CRT computational models regard the introduction of the bundle of His in the EM model: indeed, some studies have suggested that pacing in the bundle of His could restore the intrinsic electrical activation path of the heart [35, 46].

Bibliography

[1] K. N. Aronis, R. L. Ali, A. Prakosa, H. Ashikaga, R. D. Berger, J. B. Hakim, J. Liang, H. Tandri, F. Teng, J. Chrispin, and N. A. Trayanova. Accurate conduction velocity maps and their association with scar distribution on magnetic resonance imaging in patients with postinfarction ventricular tachycardias. *Circulation: Arrhythmia and Electrophysiology*, 13(4):e007792, 2020. doi: 10.1161/CIRCEP.119.007792. URL https://www.ahajournals.org/doi/abs/10.1161/CIRCEP.119.007792.

[2] A. Auricchio, H. Klein, B. Tockman, S. Sack, C. Stellbrink, J. Neuzner, A. Kramer, J. Ding, T. Pochet, A. Maarse, and J. Spinelli. Transvenous biventricular pacing for heart failure: can the obstacles be overcome? *The American Journal of Cardiology*, 83(5, Supplement 2):136–142, 1999. ISSN 0002-9149. doi: https://doi.org/10.1016/S0002-9149(98)01015-7. URL https://www.sciencedirect.com/science/article/pii/S0002914998010157.

[3] M. B. Bastos, D. Burkhoff, J. Maly, J. Daemen, C. A. den Uil, K. Ameloot, M. Lenzen, F. Mahfoud, F. Zijlstra, J. J. Schreuder, and N. M. Van Mieghem. Invasive left ventricle pressure–volume analysis: overview and practical clinical implications. *European Heart Journal*, 41(12):1286–1297, 08 2019. ISSN 0195-668X. doi: 10.1093/eurheartj/ehz552. URL https://doi.org/10.1093/eurheartj/ehz552.

[4] J. D. Bayer, R. C. Blake, G. Plank, and N. A. Trayanova. A novel rule-based algorithm for assigning myocardial fiber orientation to computational heart models. *Annals of biomedical engineering*, 40(10):2243–2254, 2012.

[5] M. Benzi, G. H. Golub, and J. Liesen. Numerical solution of saddle point problems. *Acta Numerica*, 14:1–137, 2005. doi: 10.1017/S0962492904000212.

[6] Boston Scientific. How crts work. URL https://www.bostonscientific.com/en-US/patients/about-your-device/crt-devices/how-crts-work.html. Accessed: 2022-10-10.

[7] Boston Scientific. *CRT-P Patient Manual*, 4 2014.

[8] J. R. Bragard, O. Camara, B. Echebarria, L. Gerardo Giorda, E. Pueyo, J. Saiz,

R. Sebastián, E. Soudah, and M. Vázquez. Cardiac computational modelling. *Revista Española de Cardiología (English Edition)*, 74(1):65–71, 2021. ISSN 1885-5857. doi: https://doi.org/10.1016/j.rec.2020.05.024. URL https://www.sciencedirect.com/science/article/pii/S188558572030270X.

[9] Q. Cai and M. Ahmad. Left ventricular dyssynchrony by three-dimensional echocardiography: Current understanding and potential future clinical applications. *Echocardiography*, 32(8):1299–1306, 2015. doi: https://doi.org/10.1111/echo.12965. URL https://onlinelibrary.wiley.com/doi/abs/10.1111/echo.12965.

[10] C. D. Cantwell, C. H. Roney, F. S. Ng, J. H. Siggers, S. J. Sherwin, and N. S. Peters. Techniques for automated local activation time annotation and conduction velocity estimation in cardiac mapping. *Computers in biology and medicine*, 65:229–242, 2015.

[11] E. Capuano. Calibration of a cardiac electromechanics model in view of cardiac resynchronization therapy. Master's thesis, Politecnico di Milano, 2022.

[12] Cardiovascular Physiology Concepts. Stroke work and cardiac work, 2017. URL https://cvphysiology.com/Cardiac%20Function/CF019. Accessed: 2022-11-20.

[13] Cardiovascular Physiology Concepts. Ventricular pressure-volume relationship, 2017. URL https://www.cvphysiology.com/Cardiac%20Function/CF024. Accessed: 2022-10-05.

[14] M. D. Cerqueira, N. J. Weissman, V. Dilsizian, A. K. Jacobs, S. Kaul, W. K. Laskey, D. J. Pennell, J. A. Rumberger, T. Ryan, and M. S. Verani. Standardized myocardial segmentation and nomenclature for tomographic imaging of the heart. *Circulation*, 105(4):539–542, 2002. doi: 10.1161/hc0402.102975. URL https://www.ahajournals.org/doi/abs/10.1161/hc0402.102975.

[15] Cleveland Clinic. Heart conduction system (cardiac conduction), 2021. URL https://my.clevelandclinic.org/health/body/21648-heart-conduction-system. Accessed: 2022-10-04.

[16] Cleveland Clinic. Left bundle branch block, 2022. URL https://my.clevelandclinic.org/health/diseases/23287-left-bundle-branch-block. Accessed: 2022-10-08.

[17] C. M. Costa, A. Neic, E. Kerfoot, B. Porter, B. Sieniewicz, J. Gould, B. Sidhu, Z. Chen, G. Plank, C. A. Rinaldi, et al. Pacing in proximity to scar during cardiac resynchronization therapy increases local dispersion of repolarization and susceptibility to ventricular arrhythmogenesis. *Heart rhythm*, 16(10):1475–1483, 2019.

[18] C. M. Costa, A. Neic, K. Gillette, B. Porter, J. Gould, B. Sidhu, Z. Chen, M. Elliott, V. Mehta, G. Plank, et al. Left ventricular endocardial pacing is less arrhythmogenic than conventional epicardial pacing when pacing in proximity to scar. *Heart Rhythm*, 17(8):1262–1270, 2020.

[19] M. Courtemanche, R. J. Ramirez, and S. Nattel. Ionic mechanisms underlying human atrial action potential properties: insights from a mathematical model. *American Journal of Physiology-Heart and Circulatory Physiology*, 275(1):H301–H321, 1998. doi: 10.1152/ajpheart.1998.275.1.H301. URL `https://doi.org/10.1152/ajpheart.1998.275.1.H301`. PMID: 9688927.

[20] A. Crozier, B. Blazevic, P. Lamata, G. Plank, M. Ginks, S. Duckett, M. Sohal, A. Shetty, C. A. Rinaldi, R. Razavi, et al. Analysis of lead placement optimization metrics in cardiac resynchronization therapy with computational modelling. *EP Europace*, 18(suppl_4):iv113–iv120, 2016.

[21] M. Del Greco, M. Marini, and R. Bonmassari. Implantation of a biventricular implantable cardioverter-defibrillator guided by an electroanatomic mapping system. *Europace*, 14(1):107–111, 2012.

[22] M. Del Greco, A. Zorzi, I. Di Matteo, A. Cima, M. Maines, C. Angheben, and D. Catanzariti. Coronary sinus activation patterns in patients with and without left bundle branch block undergoing electroanatomic mapping system–guided cardiac resynchronization therapy device implantation. *Heart Rhythm*, 14(2):225–233, 2017. ISSN 1547-5271. doi: https://doi.org/10.1016/j.hrthm.2016.10.025. URL `https://www.sciencedirect.com/science/article/pii/S1547527116309961`.

[23] A. E. Epstein, J. P. DiMarco, K. A. Ellenbogen, N. M. Estes, R. A. Freedman, L. S. Gettes, A. M. Gillinov, G. Gregoratos, S. C. Hammill, D. L. Hayes, M. A. Hlatky, L. K. Newby, R. L. Page, M. H. Schoenfeld, M. J. Silka, L. W. Stevenson, M. O. Sweeney, C. M. Tracy, A. E. Epstein, D. Darbar, J. P. DiMarco, S. B. Dunbar, N. M. Estes, T. B. Ferguson, S. C. Hammill, P. E. Karasik, M. S. Link, J. E. Marine, M. H. Schoenfeld, A. J. Shanker, M. J. Silka, L. W. Stevenson, W. G. Stevenson, P. D. Varosy, J. L. Anderson, A. K. Jacobs, J. L. Halperin, N. M. Albert, M. A. Creager, D. DeMets, S. M. Ettinger, R. A. Guyton, J. S. Hochman, F. G. Kushner, E. M. Ohman, W. Stevenson, and C. W. Yancy. 2012 accf/aha/hrs focused update incorporated into the accf/aha/hrs 2008 guidelines for device-based therapy of cardiac rhythm abnormalities. *Circulation*, 127(3):e283–e352, 2013. doi: 10.1161/CIR.0b013e318276ce9b. URL `https://www.ahajournals.org/doi/abs/10.1161/CIR.0b013e318276ce9b`.

[24] M. Fedele and A. Quarteroni. Polygonal surface processing and mesh generation tools for the numerical simulation of the cardiac function. *International Journal for Numerical Methods in Biomedical Engineering*, 37(4):e3435, 2021.

[25] N. G. Frangogiannis. Cardiac fibrosis. *Cardiovascular Research*, 117(6):1450–1488, 11 2020. ISSN 0008-6363. doi: 10.1093/cvr/cvaa324. URL https://doi.org/10.1093/cvr/cvaa324.

[26] M. Glikson, J. C. Nielsen, M. B. Kronborg, Y. Michowitz, A. Auricchio, I. M. Barbash, J. A. Barrabés, G. Boriani, F. Braunschweig, M. Brignole, H. Burri, A. J. S. Coats, J.-C. Deharo, V. Delgado, G.-P. Diller, C. W. Israel, A. Keren, R. E. Knops, D. Kotecha, C. Leclercq, B. Merkely, C. Starck, I. Thylén, J. M. Tolosana, and E. S. D. Group. 2021 ESC Guidelines on cardiac pacing and cardiac resynchronization therapy: Developed by the Task Force on cardiac pacing and cardiac resynchronization therapy of the European Society of Cardiology (ESC) With the special contribution of the European Heart Rhythm Association (EHRA). *European Heart Journal*, 42(35):3427–3520, 08 2021. ISSN 0195-668X. doi: 10.1093/eurheartj/ehab364. URL https://doi.org/10.1093/eurheartj/ehab364.

[27] J. M. Guccione, A. D. McCulloch, and L. K. Waldman. Passive Material Properties of Intact Ventricular Myocardium Determined From a Cylindrical Model. *Journal of Biomechanical Engineering*, 113(1):42–55, 02 1991. ISSN 0148-0731. doi: 10.1115/1.2894084. URL https://doi.org/10.1115/1.2894084.

[28] V. Gurev, P. Pathmanathan, J.-L. Fattebert, H.-F. Wen, J. Magerlein, R. A. Gray, D. F. Richards, and J. J. Rice. A high-resolution computational model of the deforming human heart. *Biomechanics and modeling in mechanobiology*, 14(4):829–849, 2015.

[29] A. Hadjis, R. Proietti, and V. Essebag. Implantation of cardiac resynchronization therapy devices using three leads by cephalic vein dissection approach. *EP Europace*, 19(9):1514–1520, 03 2017. ISSN 1099-5129. doi: 10.1093/europace/euw276. URL https://doi.org/10.1093/europace/euw276.

[30] S. Hinderer and K. Schenke-Layland. Cardiac fibrosis – a short review of causes and therapeutic strategies. *Advanced Drug Delivery Reviews*, 146:77–82, 2019. ISSN 0169-409X. doi: https://doi.org/10.1016/j.addr.2019.05.011. URL https://www.sciencedirect.com/science/article/pii/S0169409X19300614. Wound healing and fibrosis – State of play.

[31] P. R. Huntjens, J. Walmsley, S. Ploux, P. Bordachar, F. W. Prinzen, T. Delhaas,

and J. Lumens. Influence of left ventricular lead position relative to scar location on response to cardiac resynchronization therapy: a model study. *Europace*, 16 (suppl_4):iv62–iv68, 2014.

[32] E. R. Hyde, J. M. Behar, S. Claridge, T. Jackson, A. W. Lee, E. W. Remme, M. Sohal, G. Plank, R. Razavi, C. A. Rinaldi, et al. Beneficial effect on cardiac resynchronization from left ventricular endocardial pacing is mediated by early access to high conduction velocity tissue: electrophysiological simulation study. *Circulation: Arrhythmia and Electrophysiology*, 8(5):1164–1172, 2015.

[33] A. Isotani, K. Yoneda, T. Iwamura, M. Watanabe, J.-i. Okada, T. Washio, S. Sugiura, T. Hisada, and K. Ando. Patient-specific heart simulation can identify non-responders to cardiac resynchronization therapy. *Heart and vessels*, 35(8):1135–1147, 2020.

[34] L. M. Jaffe and D. P. Morin. Cardiac resynchronization therapy: history, present status, and future directions. *Ochsner Journal*, 14(4):596–607, 2014.

[35] A. Katbeh, G. Van Camp, E. Barbato, M. Galderisi, B. Trimarco, J. Bartunek, M. Vanderheyden, and M. Penicka. Cardiac resynchronization therapy optimization: a comprehensive approach. *Cardiology*, 142(2):116–128, 2019.

[36] N. Kawel-Boehm, A. Maceira, E. R. Valsangiacomo-Buechel, J. Vogel-Claussen, E. B. Turkbey, R. Williams, S. Plein, M. Tee, J. Eng, and D. A. Bluemke. Normal values for cardiovascular magnetic resonance in adults and children. *Journal of Cardiovascular Magnetic Resonance*, 17(1):1–33, 2015.

[37] A. W. Lee, A. Crozier, E. R. Hyde, P. Lamata, M. Truong, M. Sohal, T. Jackson, J. M. Behar, S. Claridge, A. Shetty, et al. Biophysical modeling to determine the optimization of left ventricular pacing site and av/vv delays in the acute and chronic phase of cardiac resynchronization therapy. *Journal of cardiovascular electrophysiology*, 28(2):208–215, 2017.

[38] A. W. Lee, C. M. Costa, M. Strocchi, C. A. Rinaldi, and S. A. Niederer. Computational modeling for cardiac resynchronization therapy. *Journal of cardiovascular translational research*, 11(2):92–108, 2018.

[39] A. W. Lee, U. C. Nguyen, O. Razeghi, J. Gould, B. S. Sidhu, B. Sieniewicz, J. Behar, M. Mafi-Rad, G. Plank, F. W. Prinzen, et al. A rule-based method for predicting the electrical activation of the heart with cardiac resynchronization therapy from non-invasive clinical data. *Medical Image Analysis*, 57:197–213, 2019.

[40] A. W. Lee, D. P. O'Regan, J. Gould, B. Sidhu, B. Sieniewicz, G. Plank, D. R. Warriner, P. Lamata, C. A. Rinaldi, and S. A. Niederer. Sex-dependent qrs guidelines for cardiac resynchronization therapy using computer model predictions. *Biophysical Journal*, 117(12):2375–2381, 2019.

[41] Magnet Academy. Mri: A guided tour, 2020. URL `https://nationalmaglab.org/education/magnet-academy/learn-the-basics/stories/mri-a-guided-tour`. Accessed: 2022-10-25.

[42] J. Malmivuo and R. Plonsey. *Bioelectromagnetism. 6. The Heart*, pages 119–130. Oxford University Press, 01 1995. ISBN 978-0195058239.

[43] M. P. Nash and A. V. Panfilov. Electromechanical model of excitable tissue to study reentrant cardiac arrhythmias. *Progress in biophysics and molecular biology*, 85(2-3): 501–522, 2004.

[44] U. C. Nguyên, N. J. Verzaal, F. A. van Nieuwenhoven, K. Vernooy, and F. W. Prinzen. Pathobiology of cardiac dyssynchrony and resynchronization therapy. *EP Europace*, 20(12):1898–1909, 05 2018. ISSN 1099-5129. doi: 10.1093/europace/euy035. URL `https://doi.org/10.1093/europace/euy035`.

[45] S. A. Niederer, G. Plank, P. Chinchapatnam, M. Ginks, P. Lamata, K. S. Rhode, C. A. Rinaldi, R. Razavi, and N. P. Smith. Length-dependent tension in the failing heart and the efficacy of cardiac resynchronization therapy. *Cardiovascular research*, 89(2):336–343, 2011.

[46] T. O'Brien, M.-S. Park, J.-C. Youn, and E. Chung. The past, present and future of cardiac resynchronization therapy. *Korean Circulation Journal*, 49, 05 2019. doi: 10.4070/kcj.2019.0114.

[47] R. W. Ogden. *Non-Linear Elastic Deformations*. Dover Publications, 1997.

[48] T. O'Hara, L. Virág, A. Varró, and Y. Rudy. Simulation of the undiseased human cardiac ventricular action potential: model formulation and experimental validation. *PLoS computational biology*, 7(5):e1002061, 2011.

[49] Pathway Medicine. Cardiac action potential - cellular basis. URL `http://pathwaymedicine.org/Cardiac-Action-Potential-Cellular-Basis`. Accessed: 2022-10-01.

[50] L. Pavarino, S. Scacchi, and S. Zampini. Newton–krylov-bddc solvers for nonlinear cardiac mechanics. *Computer Methods in Applied Mechanics and Engineering*, 295: 562–580, 2015.

[51] P. Pieragnoli, G. B. Perego, G. Ricciardi, S. Sacchi, M. Padeletti, A. Michelucci, S. Valsecchi, and L. Padeletti. Cardiac resynchronization therapy acutely improves ventricular-arterial coupling by reducing the arterial load: Assessment by pressure–volume loops. *Pacing and Clinical Electrophysiology*, 38(4):431–437, 2015. doi: https://doi.org/10.1111/pace.12585. URL `https://onlinelibrary.wiley.com/doi/abs/10.1111/pace.12585`.

[52] A. R. Pérez-Riera, R. Barbosa-Barros, M. P. C. de Rezende Barbosa, R. Daminello-Raimundo, L. C. de Abreu, and K. Nikus. Left bundle branch block: Epidemiology, etiology, anatomic features, electrovectorcardiography, and classification proposal. *Annals of Noninvasive Electrocardiology*, 24(2):e12572, 2019. doi: https://doi.org/10.1111/anec.12572. URL `https://onlinelibrary.wiley.com/doi/abs/10.1111/anec.12572`.

[53] A. Quarteroni, A. Manzoni, and C. Vergara. The cardiovascular system: Mathematical modelling, numerical algorithms and clinical applications. *Acta Numerica*, 26: 365–590, 2017. doi: 10.1017/S0962492917000046.

[54] A. Quarteroni, L. Dede', A. Manzoni, and C. Vergara. *Modelling the heart*, page 102–152. Cambridge Monographs on Applied and Computational Mathematics. Cambridge University Press, 2019. doi: 10.1017/9781108616096.007.

[55] H. Rabah, M. Youness, and A. Rabah. Sensor enabled catheter ablation study (secas). *Cureus*, 13(11), 2021.

[56] F. Regazzoni and A. Quarteroni. Accelerating the convergence to a limit cycle in 3d cardiac electromechanical simulations through a data-driven 0d emulator. *Computers in Biology and Medicine*, 135:104641, 2021. ISSN 0010-4825. doi: https://doi.org/10.1016/j.compbiomed.2021.104641. URL `https://www.sciencedirect.com/science/article/pii/S0010482521004352`.

[57] F. Regazzoni, L. Dedè, and A. Quarteroni. Biophysically detailed mathematical models of multiscale cardiac active mechanics. *PLOS Computational Biology*, 16 (10):1–42, 10 2020. doi: 10.1371/journal.pcbi.1008294. URL `https://doi.org/10.1371/journal.pcbi.1008294`.

[58] F. Regazzoni, L. Dedè, and A. Quarteroni. Machine learning of multiscale active force generation models for the efficient simulation of cardiac electromechanics. *Computer Methods in Applied Mechanics and Engineering*, 370:113268, 2020. ISSN 0045-7825. doi: https://doi.org/10.1016/j.cma.2020.113268. URL `https://www.sciencedirect.com/science/article/pii/S0045782520304539`.

[59] F. Regazzoni, L. Dedè, and A. Quarteroni. Active force generation in cardiac muscle cells: mathematical modeling and numerical simulation of the actin-myosin interaction. *Vietnam Journal of Mathematics*, 49(1):87–118, 2021.

[60] M. Reumann, B. Osswald, and O. Doessel. Noninvasive, automatic optimization strategy in cardiac resynchronization therapy. *Anatolian Journal of Cardiology/Anadolu Kardiyoloji Dergisi*, 7, 2007.

[61] V. Russo, L. Lovato, and G. Ligabue. Cardiac mri: technical basis. *La radiologia medica*, 125(11):1040–1055, 2020.

[62] K. Sedláček, R. Polášek, H. Jansová, D. Grieco, P. Kučera, J. Kautzner, D. P. Francis, and D. Wichterle. Inadvertent qrs prolongation by an optimization device-based algorithm in patients with cardiac resynchronization therapy. *PloS one*, 17(9):e0275276, 2022.

[63] S. D. Serai, M.-L. Ho, M. Artunduaga, S. S. Chan, and G. B. Chavhan. Components of a magnetic resonance imaging system and their relationship to safety and image quality. *Pediatric radiology*, 51(5):716–723, 2021.

[64] J. B. Shea and M. O. Sweeney. Cardiac resynchronization therapy a patient’s guide. *Circulation*, 108(9):e64–e66, 2003. doi: 10.1161/01.CIR.0000085657.09097.38. URL `https://www.ahajournals.org/doi/abs/10.1161/01.CIR.0000085657.09097.38`.

[65] Simple Med. The cardiac cycle, 2022. URL `https://simplemed.co.uk/subjects/cardiovascular/cardiac-cycle#:~:text=There%20are%20seven%20stages%20of,changes%20seen%20in%20an%20ECG.` Accessed: 2022-10-05.

[66] M. Spartalis, E. Tzatzaki, E. Spartalis, C. Damaskos, A. Athanasiou, E. Livanis, and V. Voudris. Pathophysiology and current evidence for detection of dyssynchrony. *Cardiology Research*, 8(5):179, 2017.

[67] N. Sperelakis, Y. Kurachi, A. Terzic, and M. V. Cohen. *Heart physiology and pathophysiology*. Elsevier, 2000.

[68] S. Stella. *Data-driven mathematical and numerical models for the ventricular electromechanics with application to cardiac resynchronization therapy*. PhD thesis, Politecnico di Milano, 2021.

[69] S. Stella, C. Vergara, M. Maines, D. Catanzariti, P. C. Africa, C. Dematteè, M. Centonze, F. Nobile, M. Del Greco, and A. Quarteroni. Integration of activation maps of epicardial veins in computational cardiac electrophysiology. *Com-*

puters in Biology and Medicine, 127:104047, 2020. ISSN 0010-4825. doi: https://doi.org/10.1016/j.compbiomed.2020.104047. URL https://www.sciencedirect.com/science/article/pii/S0010482520303784.

[70] S. Stella, F. Regazzoni, C. Vergara, L. Dedé, and A. Quarteroni. A fast cardiac electromechanics model coupling the eikonal and the nonlinear mechanics equations. *Mathematical Models and Methods in Applied Sciences*, 32(08):1531–1556, 2022. doi: 10.1142/S021820252250035X. URL https://doi.org/10.1142/S021820252250035X.

[71] P. Stewart, O. V. Aslanidi, D. Noble, P. J. Noble, M. R. Boyett, and H. Zhang. Mathematical models of the electrical action potential of purkinje fibre cells. *Philosophical Transactions of the Royal Society A: Mathematical, Physical and Engineering Sciences*, 367(1896):2225–2255, 2009. doi: 10.1098/rsta.2008.0283. URL https://royalsocietypublishing.org/doi/abs/10.1098/rsta.2008.0283.

[72] M. Strocchi, C. M. Augustin, M. A. F. Gsell, E. Karabelas, A. Neic, K. Gillette, O. Razeghi, A. J. Prassl, E. J. Vigmond, J. M. Behar, J. Gould, B. Sidhu, C. A. Rinaldi, M. J. Bishop, G. Plank, and S. A. Niederer. A publicly available virtual cohort of four-chamber heart meshes for cardiac electro-mechanics simulations. *PLOS ONE*, 15(6):1–26, 06 2020. doi: 10.1371/journal.pone.0235145. URL https://doi.org/10.1371/journal.pone.0235145.

[73] J. Sundnes, S. Wall, H. Osnes, T. Thorvaldsen, and A. D. McCulloch. Improved discretisation and linearisation of active tension in strongly coupled cardiac electromechanics simulations. *Computer methods in biomechanics and biomedical engineering*, 17(6):604–615, 2014.

[74] E. Surkova, L. P. Badano, R. Bellu, P. Aruta, F. Sambugaro, G. Romeo, F. Migliore, and D. Muraru. Left bundle branch block: from cardiac mechanics to clinical and diagnostic challenges. *EP Europace*, 19(8):1251–1271, 04 2017. ISSN 1099-5129. doi: 10.1093/europace/eux061. URL https://doi.org/10.1093/europace/eux061.

[75] N. Y. Tan, C. M. Witt, J. K. Oh, and Y.-M. Cha. Left bundle branch block. *Circulation: Arrhythmia and Electrophysiology*, 13(4):e008239, 2020. doi: 10.1161/CIRCEP.119.008239. URL https://www.ahajournals.org/doi/abs/10.1161/CIRCEP.119.008239.

[76] K. H. W. J. ten Tusscher, D. Noble, P. J. Noble, and A. V. Panfilov. A model for human ventricular tissue. *American Journal of Physiology-Heart and Circulatory*

Physiology, 286(4):H1573–H1589, 2004. doi: 10.1152/ajpheart.00794.2003. URL https://doi.org/10.1152/ajpheart.00794.2003. PMID: 14656705.

[77] J. Tomek, A. Bueno-Orovio, E. Passini, X. Zhou, A. Minchole, O. Britton, C. Bartolucci, S. Severi, A. Shrier, L. Virag, A. Varro, and B. Rodriguez. Development, calibration, and validation of a novel human ventricular myocyte model in health, disease, and drug block. *eLife*, 8:e48890, dec 2019. ISSN 2050-084X. doi: 10.7554/eLife.48890. URL https://doi.org/10.7554/eLife.48890.

[78] N. Trayanova. Whole-heart modeling applications to cardiac electrophysiology and electromechanics. *Circulation research*, 108:113–28, 01 2011. doi: 10.1161/CIRCRESAHA.110.223610.

[79] C. Vergara, S. Stella, M. Maines, P. C. Africa, D. Catanzariti, C. Demattè, M. Centonze, F. Nobile, A. Quarteroni, and M. Del Greco. Computational electrophysiology of the coronary sinus branches based on electro-anatomical mapping for the prediction of the latest activated region. *Medical & Biological Engineering & Computing*, 60(8):2307–2319, 2022.

[80] C. Werner, F. Sachse, and O. Dössel. Electrical excitation propagation in the human heart. *International Journal of Bioelectromagnetism*, 2(2), 2000.

[81] N. Westerhof, J.-W. Lankhaar, and B. E. Westerhof. The arterial windkessel. *Medical & biological engineering & computing*, 47(2):131–141, 2009.

[82] Wikimedia Commons. A diagram of the human heart, as seen by a coronal section., 2006. URL https://commons.wikimedia.org/wiki/File:Diagram_of_the_human_heart_%28cropped%29.svg. Accessed: 2022-09-30.

[83] S. A. Worsnick, P. S. Sharma, and P. Vijayaraman. Right ventricular septal pacing: a paradigm shift. *The Journal of Innovations in Cardiac Rhythm Management*, 9(5): 3137, 2018.

[84] L. Zocchi, G. D'Arcangelo, T. Florio, M. Gussoni, U. Laforenza, C. Maioli, C. Molinari, D. Mutolo, P. Pagliaro, and V. Tancredi. *Principi di Fisiologia*. EDISES, 2012.

[85] Zygote Media Group Inc. The zygote solid 3d heart model., 2013.

List of Figures

List of Tables